

ABSTRACT

TAYLOR, MICHAEL PHILLIP. Novel Split-Tip Probe for Molecular Orientation and Nonlinear Optical Studies. (Under the direction of Dr. Hans Hallen.)

Nanoscale materials are now fabricated by a variety of means, but the dominant methods rely on self-assembly or advanced lithography. These and other fabrication schemes, especially self-assembly, can create structures in which the molecular orientation perpendicular to the surface is controlled by the chemistry. This is important for functionality. We present the first step of a method to take this control of orientation one step further - a split-tip nanoprobe, used to generate a high electric field in a local region near the probe tip. It is this field that will produce nonlinear optical effects in conjugated polymer molecules as well as orient molecules in the plane of the surface, while the small spot provides lateral resolution. The method allows variation of the orientation on a < 100 *nm* length scale, so that nanoscale functionality that is based on the relative orientation of molecules can be obtained. This is needed since a uniform layer is not a device. This is a powerful concept for high performance molecular devices, since the properties of molecules are highly anisotropic. It also allows the fabrication of many independent structures close together on a surface, as has been the successful paradigm in microelectronics. The 'nanopoling' scheme that we propose should be much more effective at orienting molecules than current poling methods due to the larger electric field that can be generated locally. This advantage is in addition to the obvious resolution improvement.

NOVEL SPLIT-TIP PROBE FOR MOLECULAR ORIENTATION AND NONLINEAR
OPTICAL STUDIES

by

MICHAEL PHILLIP TAYLOR

A dissertation submitted to the Graduate Faculty of
North Carolina State University
in partial fulfillment of the
requirements for the Degree of
Doctor of Philosophy

PHYSICS

Raleigh, North Carolina

2007

APPROVED BY:

Dr. Laura I. Clarke

Dr. Hien T. Tran

Dr. Hans Hallen
Chair of Advisory Committee

Dr. David E. Aspnes

Dedication

*To my parents, Archie and Geneva Taylor,
for teaching me tolerance and perseverance.*

Biography

Michael Phillip Taylor was born on February 7, 1970 in Chicago, IL. He is the youngest son of Archie V. Geneva H. Taylor. He graduated from Saint Rita High School in 1987, earning an athletic scholarship to attend Morehouse College in Atlanta, GA. While at Morehouse, he involved himself with several organizations and activities, both on and off campus, always focussed on community uplift. In 1992, he earned his Bachelors of Science degree in Physics. Mr. Taylor began his graduate work in Physics at Clark Atlanta University (CAU). While in the masters program there, he met his best friend, Shree Yvonne Whitaker. He left CAU in 1996 to pursue a Ph.D. in Physics at North Carolina State University (NCSU) in Raleigh.

At NCSU, Mr. Taylor earned both Graduate Assistance in areas of National Need (GAANN) and Preparing the Professoriate fellowships. He engaged himself with a host of outreach initiatives geared toward academic social enrichment, both on and off campus. Most noted was the creation of *Feet for the Fight*. This event was the debut 5K in the nation for raising prostate cancer awareness in the surrounding community and generating research funds. In November of 2003, he married Shree Whitaker Taylor, Ph.D. and they now have two beautiful daughters - Trinity Vaughn Whitaker Taylor and Zayin Genevieve Whitaker Taylor. In November of 2006, he successfully defended his Ph.D. dissertation in Physics, with a concentration in Near-Field Optics.

Mr. Taylor has begun his career in Physics with the Remote Sensing Laboratory at Andrews Air Force Base and he looks forward to making positive contributions in science and his community.

Contents

List of Figures	v
List of Tables	vii
1 Introduction	1
2 Near-Field Scanning Optical Microscopy	5
2.1 Limits on Conventional Microscopy	5
2.2 NSOM - Beyond the Diffraction Limit	8
3 The Split-Tip Probe	18
3.1 Design Requirements	19
3.2 Probe Fabrication	21
4 Modeling The Tip	33
4.1 Mathematical Modeling	33
4.2 Modeling the Split-Tip	34
4.3 Cartesian Coordinates	35
4.4 Cylindrical Coordinates	38
4.5 Finite Element Approach	41
5 Applications: Molecular Orientation	44
5.1 Molecular Polarization	44
5.2 Nano-lithography	45
6 Conclusion	49
Bibliography	50

Appendices	55
Appendix A	56
Appendix B	75
Appendix C	94

List of Figures

2.1	Abbe's Theory of Image Formation	6
2.2	Comparison of Conventional and Near-Field Microscopy Approaches	8
2.3	x -polarized light near a sub-wavelength aperture	10
2.4	x -polarized light at various distances from a sub-wavelength aperture	11
2.5	Boundary Conditions for E_x , E_y , and E_z near the tip of an NSOM probe	12
2.6	x -polarized component E_x^2 , showing change with distance from the aperture	13
2.7	y -polarized light near a sub-wavelength aperture	14
2.8	y -polarized light at various distances from a sub-wavelength aperture	14
2.9	y -polarized component E_y^2 , showing change with distance from the aperture	15
2.10	z -polarized light near a sub-wavelength aperture	16
2.11	z -polarized light at various distances from a sub-wavelength aperture	16
2.12	z -polarized component E_z^2 , showing change with distance from the aperture	17
3.1	The Split-Tip Probe.	19
3.2	A schematic of the probe illustrates the major features.	20
3.3	SEM image of a larger-aperture tapered fiber fabricated by the heat-and-pull method.	21
3.4	The Etching Process	22
3.5	A split-tip probe, showing the entire tapered region.	28
3.6	The tip of a split-tip probe	29
3.7	The tip of a split-tip probe	30
3.8	A close look at the aperture of a typical split-tip probe	31
3.9	A detailed look at the split of the probe.	32
4.1	The Electric Field of a Split-Tip Probe	43
5.1	Sample orientation schemes due to alignment of polymer molecules	47
A.1	The split-tip probe	58
A.2	A schematic of the probe illustrates the major features.	59
A.3	SEM image of a larger-aperture tapered fiber fabricated by the heat-and-pull method.	60
A.4	A tip holding fixture used for the coating of split-tip fibers.	62

A.5	A split-tip probe fabricated by the same method that reliably produces good NSOM probes.	63
A.6	A close look at the aperture of a typical spit-tip probe	67
A.7	A detailed look at the split of the probe.	68
A.8	A photograph of the tip holder.	69
A.9	Exposed film of a water soluble PPV precursor Poly (p-xylene tetrahydrothiophenium chloride), 2.5% in water.	71
B.1	The split-tip probe	77
B.2	A schematic of the probe illustrates the major features.	78
B.3	Sample orientation schemes due to alignment of polymer molecules	81
B.4	Layer Solidification Using Various Light Sources	84
B.5	The Electric Field of a Split-Tip Probe	86
B.6	Exposed film of a water soluble PPV precursor.	89
C.1	Representative images of YBCO in a 5 μm square region.	102
C.2	Optical images of YBCO in a 5 μm square region.	103
C.3	Optical images of YBCO in a 10 μm square region.	104

List of Tables

B.1	Normalized transmission data extracted from images similar to B.6	90
-----	---	----

Chapter 1

Introduction

There are a multitude of microscopic techniques in existence. Among them, optical microscopy is the most often utilized research tool employed today. This is due to several key benefits:

- It is reliable.
- It is non-invasive and can be used on a variety of samples.
- It is fast.
- It is inexpensive.
- It is fairly simple to use.
- It employs several contrast mechanisms [4]:
 - Optical density
 - Index of refraction
 - Fluorescence
 - Birefringence/Polarization
 - Reflectivity
 - Absorption spectroscopy
 - Raman spectroscopy

There is, however, a significant disadvantage to conventional optical microscopy, that being the resolution limits associated with its use. In the far-field, this limitation is wavelength dependent. In fact, according to the Abbe diffraction limit [1], the best resolution obtainable by an optical microscope is $\lambda/2$. This diffraction limit has been overcome with the advent of near-field optical microscopy (NSOM) [32]. NSOM was first proposed by Synge [41], employing a localized probe, such as a subwavelength aperture in an opaque screen. Rastering this probe in the region above a sample ($z \ll \lambda$) will generate an image on the order of the size of the probe. Hence, the fabrication of quality probes is crucial to maintaining high resolution, signal strength, and reliability for NSOM.

NSOM probes have been fabricated from a number of materials, to include atomic force microscope (AFM) cantilever tips, glass pipettes, and cleaved crystals. Probably the most common probe material used today is the tapered optical fiber (single mode). Due to the loss of total internal reflection (caused by the taper), optical fiber probes are typically coated with a film of highly reflective material, usually Al, to prevent light loss.

Essential to probe fabrication is the reliable production of a quality taper. Quality is determined by the geometry, the guiding parameters, scattering, and the loss of photons due to absorption in the metallized taper region. The task of producing an NSOM tapered fiber tip is the most commonly accomplished by:

The Pulling Method. This technique utilizes the controlled heating and pulling of a single mode fiber in a commercial micropipette puller. The optical fiber is stripped locally of its polymer jacket and the exposed glass is heated. Then it is pulled at opposite ends until it breaks (at the point of heating). With optimized parameters, this process produces two finely tapered probes with 50 - 100 *nm* apertures.

Meniscus Etching (Turner Method). This technique utilizes an etchant such as buffered hydrofluoric acid to form the taper. A stripped optical fiber is inserted into the etchant and a meniscus is formed around the fiber. Etching takes place at the point where the meniscus is formed. This produces a shorter taper with a larger cone angle. This yields at least an order of magnitude more optical efficiency than pulled probes.

Tube Etching. This technique is the same as the meniscus etching technique, with the exception of stripping the fiber jacket. Since the jacket is resistant to the etching process, the taper formation process itself takes place inside the tube formed by the

jacket. Among the advantages of tube etching over the Turner method are high reproducibility, an extremely smooth surface at the taper, and more control over cone angle. This is likely due to the fact that the "tube" provides protection from vibrations, air movement, etc.

NSOM continues to develop and is becoming a common technique for optical imaging and spectroscopy. It is also becoming a suitable instrument for the fabrication of nano-structures (scanning near-field lithography). Conjugated polymers are increasingly becoming the material of choice for their promising optoelectric properties and applications, including such devices as light emitting diodes, photodiodes, and polymer lasers. Nonpatterned polymer films can be sufficient for large area, low-cost applications. However, lateral patterning, on a range of lengthscales, is required for multicolor displays, integrated electronics, and the fabrication of smart materials. Nano-structures have been fabricated from conjugated polymer thin films with well defined features [36].

In addition to patterning, many complex materials and polymer or other molecular-based electronic devices depend upon the orientation of the components for their properties. The interface properties are crucial to performance, and are determined by the orientation of any non symmetric molecules involved. orientation also matters within the film. For example, problems of orientation in conducting polymers lead to poor electrical performance, and nonlinear polymers must usually be poled to yield some degree of orientation in order to function well. The key benefit of using complex materials is that the material properties can be adjusted, such that materials with novel properties can be grown and optimized for a particular application. A problem with current deposition techniques is that it is difficult to control the orientation of the molecules deposited onto an arbitrary surface, especially orientation in the plane of the film when one wants to vary the orientation on the nanometer scale.

We present in this work the fabrication of a novel tool, the split-tip probe, to be employed within an NSOM unit for the purpose of controlling the orientation in the plane of an arbitrary surface, onto which molecules are to be deposited. This will provide new capabilities for complex material fabrication, and will be a powerful method to create interfaces and higher performance material for conducting polymer devices. In order to accomplish this, we must understand the fundamental tenants of NSOM and the manner in which it can be used as a fabrication tool. A repeatable technique for fabricating the

split-tip probe must be established and its fabrication constraints understood. Utilization of the split-tip must be preceded by a fundamental understanding of both the optical and DC fields that can be produced at its apex. Once these milestones have been met, we can finally consider the applications of its use. Thus is the organization of the following body of work.

Chapter 2

Near-Field Scanning Optical Microscopy

2.1 Limits on Conventional Microscopy

Conventional optical microscopy has been one of the most powerful tools used by researchers for hundreds of years. Limits on diffraction kept the pioneers of this technology from realizing the idea of optical imaging on a sub-wavelength scale.

Light diffracted from the slits of a periodic diffraction grating diverge and interfere both constructively and destructively. Light that passes through the slits undiffracted are termed zeroth order light. Higher order diffracted light is described by

$$d \sin \theta = m\lambda \quad (m = \pm 1, \pm 2, \pm 3, \dots) \quad (2.1)$$

This gives the values of θ for which the diffraction pattern yields zero intensity (destructive interference). If the light from the periodic grating is passed through a convex lens, one will observe Fraunhofer diffraction. One bright spot will appear on the focal plane of the lens along the axis at $\theta = 0$. Alternating dark and bright spots will be observed on either side of the central bright spot.

Placement of the periodic grating onto a microscope stage provides an opportunity to examine the limits on image formation as observed by Ernest Abbe. Here, a grating is considered, but there can be any object exhibiting any contrast mechanism to be observed with light: height, refractive index, color, fluorescence, optical density, reflectivity, etc.

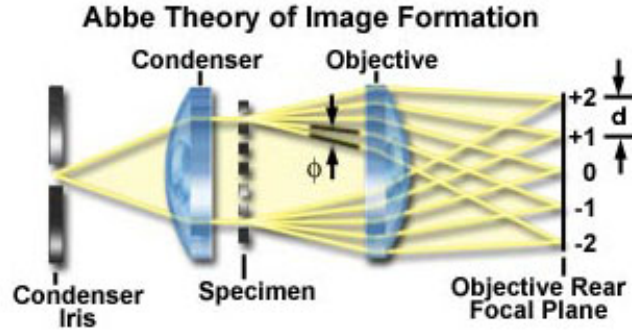


Figure 2.1: Abbe's Theory of Image Formation

When the grating (or other object) is illuminated with a collimated beam of light, the objective lens collects the zeroth and higher order diffracted light. Light that passes through the grating undiffracted, will be imaged on the rear focal plane of the objective, in the center of its optical axis. First and higher order diffracted light will be collected by the objective at an angle θ and imaged at the rear focal plane of the objective on both sides of the undiffracted beam. The diffracted light emerges from the objective rear aperture to interfere and form an intermediate, magnified image of the grating that is further magnified by the eyepiece.

Abbe determined that in order to form a recognizable image, the objective must capture the zeroth order light rays and at least one of the higher order diffracted waves or two adjacent orders. The diffraction angle is dependent upon the grid spacing and the wavelength is determined by the refractive index n of the medium between the grating and the objective front lens; i.e.,

$$\lambda_n = \frac{\lambda_0}{n} \quad (2.2)$$

where λ_n is the wavelength in the medium and λ_0 is the vacuum wavelength. The diffraction equation, given by equation 2.1 above, can now be rewritten as:

$$d = \frac{\lambda_0}{n \sin \theta} \quad (2.3)$$

Abbe originally defined the numerical aperture NA of the objective as:

$$NA = n \sin \theta \quad (2.4)$$

So the equation 2.3 reduces to:

$$d = \frac{\lambda_0}{NA} \quad (2.5)$$

Equation 2.5, known as Abbe's diffraction limit, is one of the most fundamental to optical microscopy and demonstrates that an objective's ability to resolve fine details in a specimen, such as a periodic grating, is dependent upon both the wavelength of illuminating light rays and the numerical aperture. Abbe further determined that

$$d = 0.61 \frac{\lambda_0}{NA} \quad (2.6)$$

The accepted practice is to invoke the Rayleigh criterion which states that two objects are resolvable if they are separated by a distance at least equal to the distance given in equation 2.6. Thus, the lower the wavelength or the higher the numerical aperture, the greater the resolving power of the objective. Note that there is an upper limit to this sort of improvement. The highest NA obtainable with the best oil-immersion lenses is around 1.3 – 1.4. Therefore, equation 2.6 is usually reduced to

$$d = \frac{\lambda}{2} \quad (2.7)$$

This gives us a means by which to calculate the smallest features visible for a given wavelength. The maximal resolution is then approximately equal to half the wavelength of the radiation used, which for visible light applications results in a spatial resolution of 250 – 300 nm . The arbitrary nature of the definition, however, only provides guidance for determining the optical resolution, and in actual practice, the experimental situation is often quite different. For instance, with excellent signal-to-noise and/or an accurate description of the instrumental response function, smaller distances can, in theory, be determined. More often, however, the experimental conditions and aberrations in the optical components conspire to lower the resolution and prevent attainment of the theoretical limit. In common practice, therefore, the practical limitation on spatial resolution is often worse than the so-called diffraction-limit.

It is advantageous to use shorter wavelength light in order to improve the diffraction-limited resolution. Electron microscopes have realized very high diffraction-limited resolution because they utilize the short wavelength of the de Broglie wave of an electron. However, a disadvantage of the electron microscope is that the observable samples are limited to conductors installed in a vacuum, and this does not allow one to observe insulators and living biological samples.

2.2 NSOM - Beyond the Diffraction Limit

Near-field scanning optical microscopy (NSOM) circumvents the diffraction limits of conventional optical microscopy. It does so by combining the extremely high topographic resolution of techniques such as AFM with the significant temporal resolution, polarization characteristics, spectroscopic capabilities, sensitivity, and flexibility inherent in many forms of optical microscopy. This technique is based upon the detection of non-propagating evanescent waves in the near-field region. The near-field region is defined as the region away from the sample that is less than the wavelength of the incident light. With NSOM this distance is typically on the order of a few nanometers. In order to achieve an optical resolution better than the diffraction limit, a probe has to be brought within the near-field region. The NSOM probe can either detect in the near-field directly, by means of a sub-wavelength size aperture (collection mode), or by using the probe as a wave guide with a sub-wavelength scattering source and detecting the evanescent waves as they propagate into the far-field (transmission mode). Probes are typically fabricated from optical fibers, which have been either mechanically drawn or chemically etched. Light in the near-field carries more high-

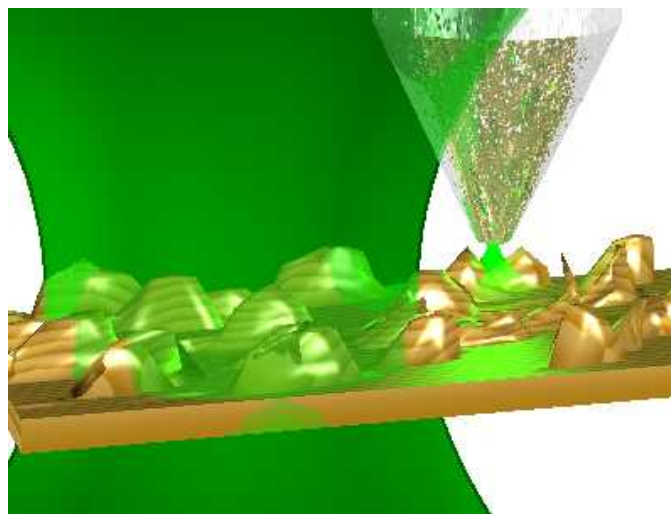


Figure 2.2: Comparison of Conventional and Near-Field Microscopy Approaches

frequency (greater detail) information and has its greatest amplitude in the region within the first few tens of nanometers of the specimen surface. Because the near-field light decays exponentially within a distance less than the wavelength of the light, it usually goes un-

detected. In effect, as the light propagates away from the surface into the far-field region, the highest-frequency spatial information is filtered out, and the Abbe limit on resolution is imposed. By detecting and utilizing the near-field light before it undergoes diffraction, the NSOM makes available the full gamut of far-field optical contrast-enhancing mechanisms at much higher spatial resolution. In addition to non-diffraction-limited high-resolution optical imaging, near-field optical techniques can be applied to chemical and structural characterization through spectroscopic analysis at resolutions beneath 100 nanometers.

There are two fundamental differences between near-field and far-field (conventional) optical microscopy: the size of the specimen area that is illuminated, and the separation distance between the source of radiation and the specimen. In conventional far-field optical microscopy, the distance between the light source and the specimen is typically much greater than the wavelength of the incident light, whereas in NSOM, a necessary condition of the technique is that the illumination source is closer to the specimen than the wavelength of the illuminating radiation.

In an aperture-scanning NSOM instrument, the probe can be used in collection or transmission mode. Therefore, it is useful to know the behavior of the electric (optical) field near the tip of such a probe. Measuring these fields is not trivial. The simplest form of the theory dates back to Hans Bethe, with a slight correction by Bouwkamp, who calculated the fields near a thin, perfectly conducting, flat sheet with an aperture in it. This is not exactly what we have experimentally. We have an aperture at the end of a pointed structure that has been coated with a metal (usually *Al*); but the metal is often thicker than the aperture size. Bouwkamp's work in this area uses oblate-spheroidal coordinates u, ν , and ϕ defined by

$$\begin{aligned} x &= a\sqrt{(1-u^2)(1+\nu^2)}\cos\phi \\ y &= a\sqrt{(1-u^2)(1+\nu^2)}\sin\phi \\ z &= au\nu \end{aligned} \tag{2.8}$$

where a is the radius of the aperture, z denotes the distance from the center of the aperture. The aperture is sub-wavelength in diameter, so $a < \lambda$. The designation far-field will refer to $z > a$, and near-field will refer to the region $0 < z < \lambda/10$. For incident light through the aperture, polarized in the x -direction, the electric field components due to diffraction

are given by:

$$E_x = -kz - \frac{2}{\pi}kau \left[1 + \nu \arctan(\nu) + \frac{1}{3} \frac{1}{u^2 + \nu^2} + \frac{x^2 - y^2}{3a^2(u^2 + \nu^2)(1 + \nu^2)^2} \right] \quad (2.9)$$

$$E_y = \frac{4kxyu}{3\pi a(u^2 + \nu^2)(1 + \nu^2)^2} \quad (2.10)$$

$$E_z = \frac{4kx\nu}{3\pi(u^2 + \nu^2)(1 + \nu^2)^2} \quad (2.11)$$

The norm values of these electric field components are plotted with $a = 1/5\lambda$, at a distance of $z = 1/10 a$ from the aperture. for typical distances above the sample. Figure 2.4

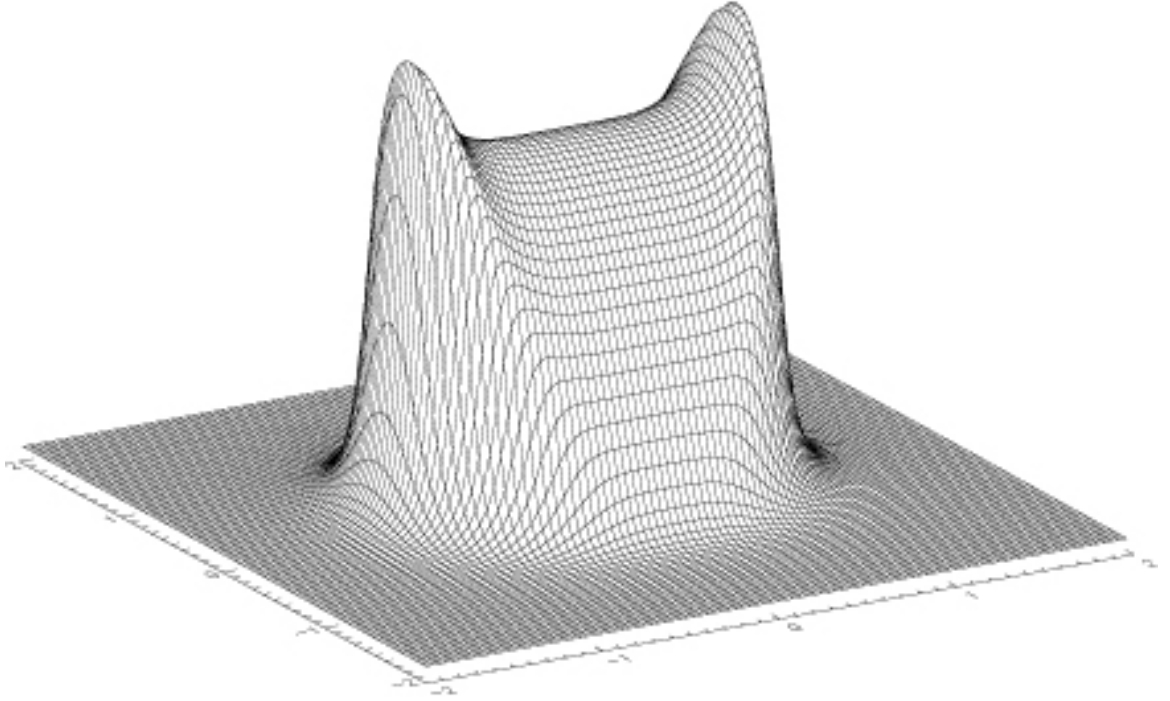


Figure 2.3: x -polarized light near a sub-wavelength aperture

displays a profile of E_x^2 at various distances above the aperture, showing a region $3a$ on a side. Figure 2.4(a) is $(1/100)a$ above the aperture. Figures 2.4(a) and (b) are $(1/10)a$ and a above the aperture, respectively. One can clearly see the outline of the aperture. This is because E_x lies within the aperture. This behavior is clear when one considers the boundary conditions for electric field near a metal surface:

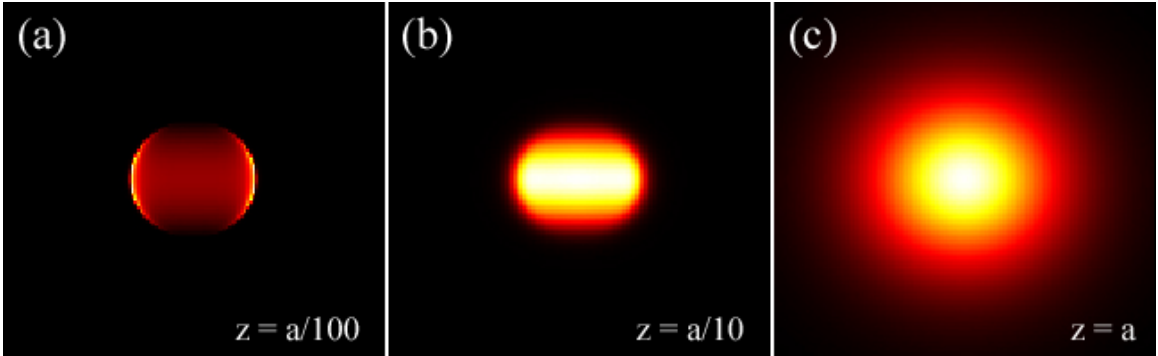


Figure 2.4: x -polarized light at various distances from a sub-wavelength aperture

1. There can be no electric field in the plane of the surface (no E_x or E_y over the metal here).
2. The electric field is allowed normal to the surface (E_z is allowed over metal here).
3. The situation within the aperture is different: now the metal is on the edges only, so E_x and E_y but not E_z can be near the edges.

Anything can be in the middle according to the selection rules, but only E_x has the source (input light). This behavior is illustrated for an NSOM probe in 2.5.

Figure 2.8 displays a profile of E_y^2 at various distances above the aperture, showing a region $3a$ on a side. Here, the data have been scaled. E_y is actually much smaller than the other two. A comparison of figures 2.6, 2.9, and 2.12 reveals a more realistic, relative scaling. As expected from the boundary conditions, E_y exists inside the aperture at the metal interface. As with E_x^2 , a significant drop in resolution occurs as we move into the far-field; i.e., at distances $\geq a$ above the aperture.

Figure 2.11 displays a profile of E_z^2 at various distances above the aperture, showing a region $3a$ on a side. Also from the boundary conditions, E_z lies on the outside of the aperture, under the metal. The electric field is allowed normal to the metal surface and E_z is parallel to the surface, as light propagates toward/through the aperture. Therefore, E_z will be observed right outside of the aperture, perpendicular to the sheet (or the thickness of the metal coating). Figure 2.11(b) shows (as does figures 2.4(b) and 2.8(b)) the aperture is just resolved at a distance $(1/10)a$ over the aperture. of course, in the far-field (a distance

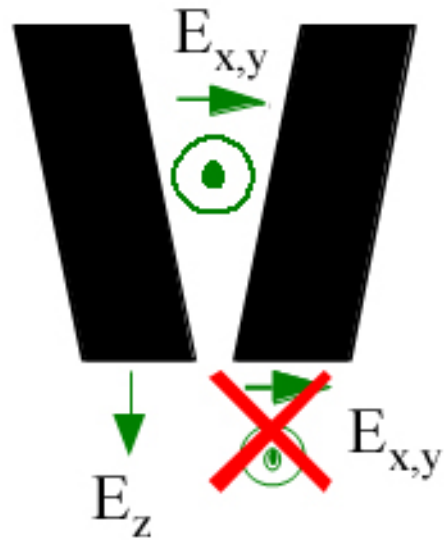


Figure 2.5: Boundary Conditions for E_x , E_y , and E_z near the tip of an NSOM probe

$\geq a$ over the aperture), there is a great reduction in resolution and the Abbe diffraction limit is invoked.

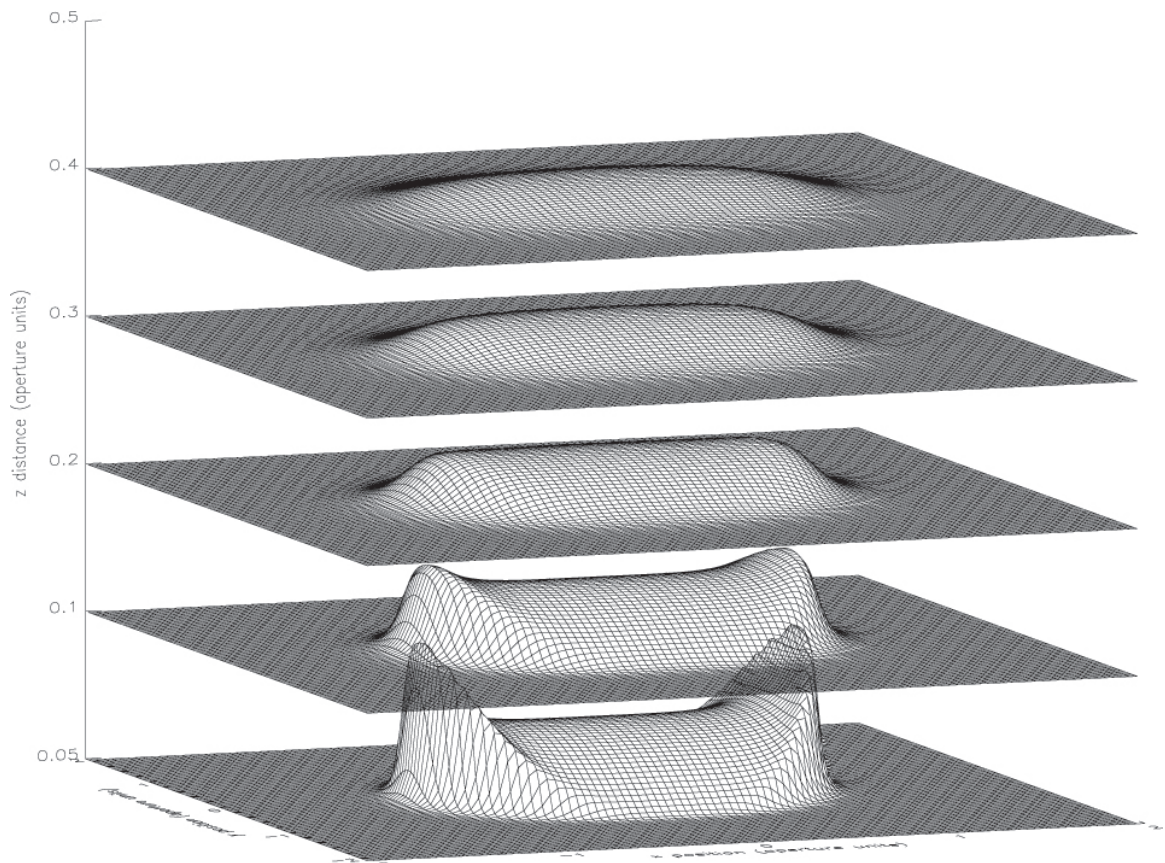


Figure 2.6: x -polarized component E_x^2 , showing change with distance from the aperture

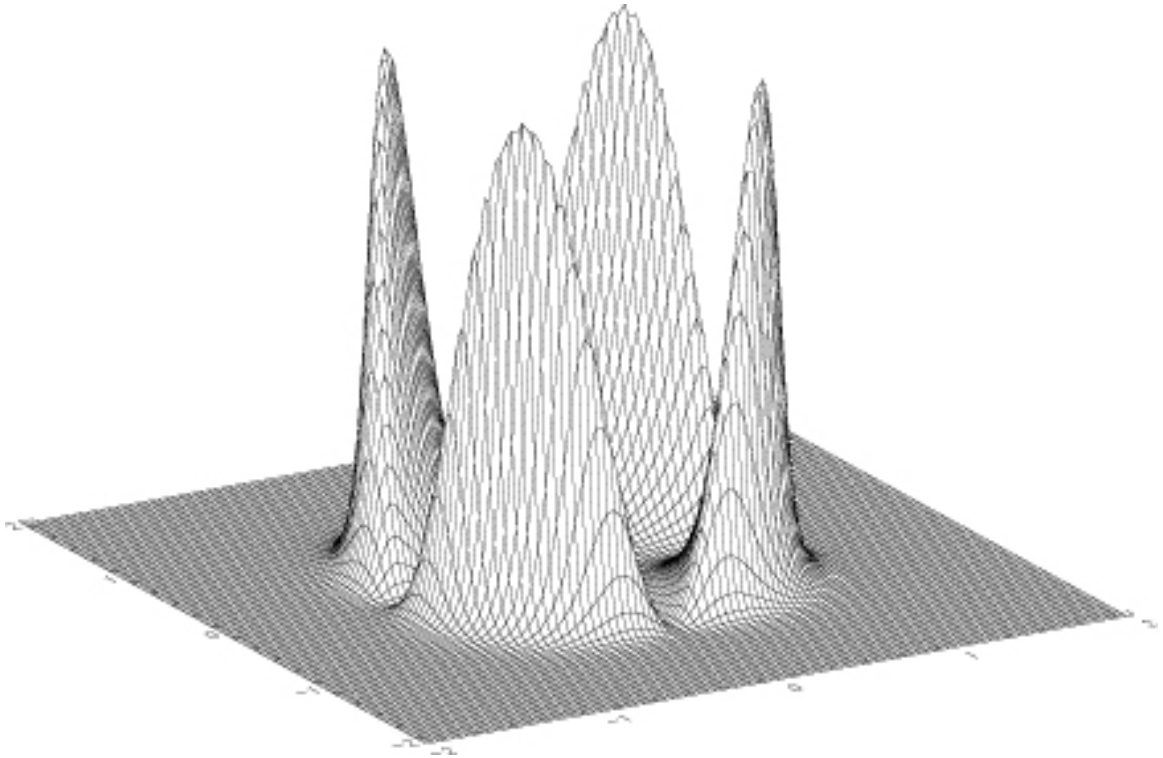


Figure 2.7: y -polarized light near a sub-wavelength aperture

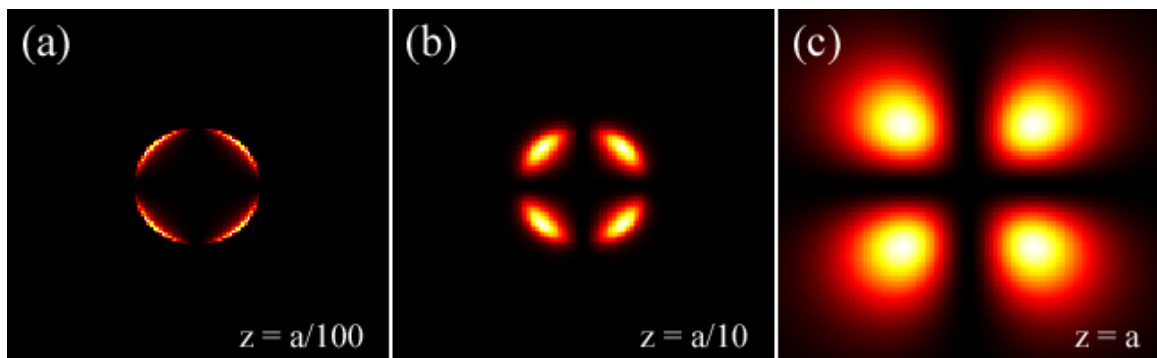


Figure 2.8: y -polarized light at various distances from a sub-wavelength aperture

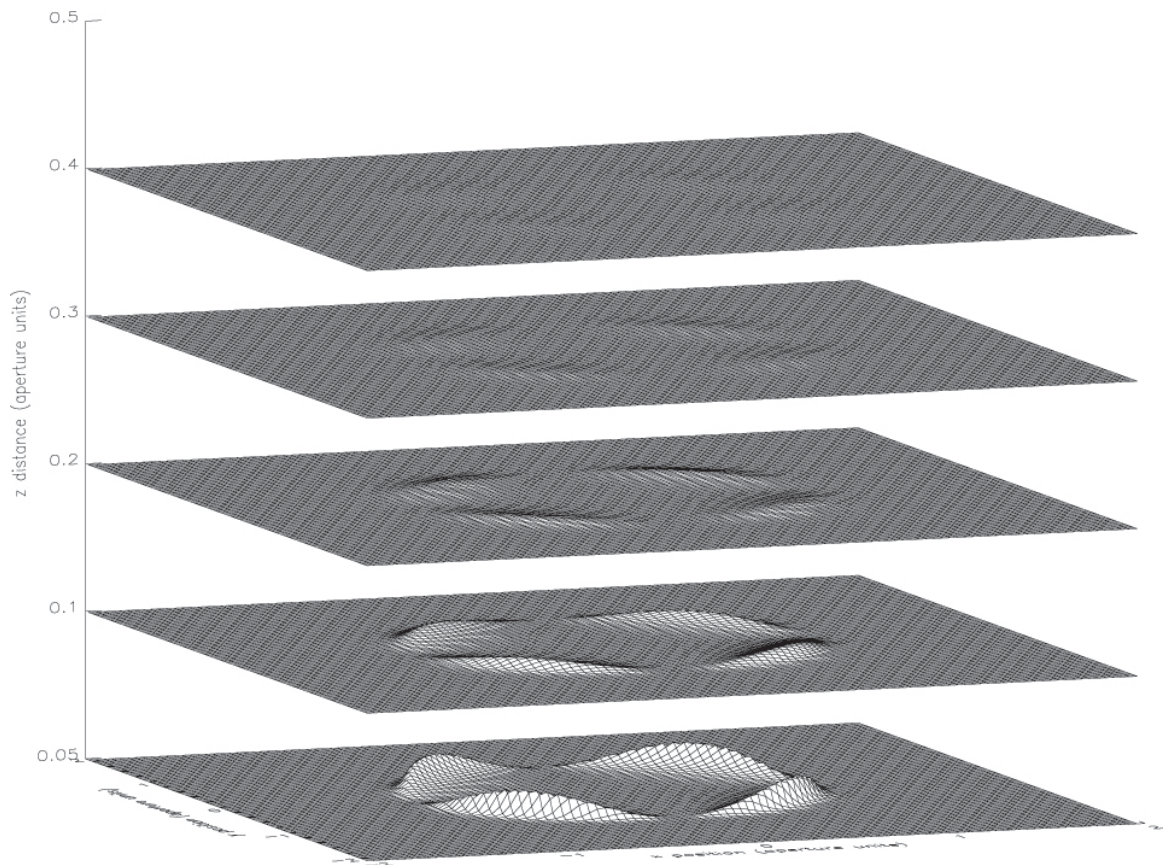


Figure 2.9: y -polarized component E_y^2 , showing change with distance from the aperture

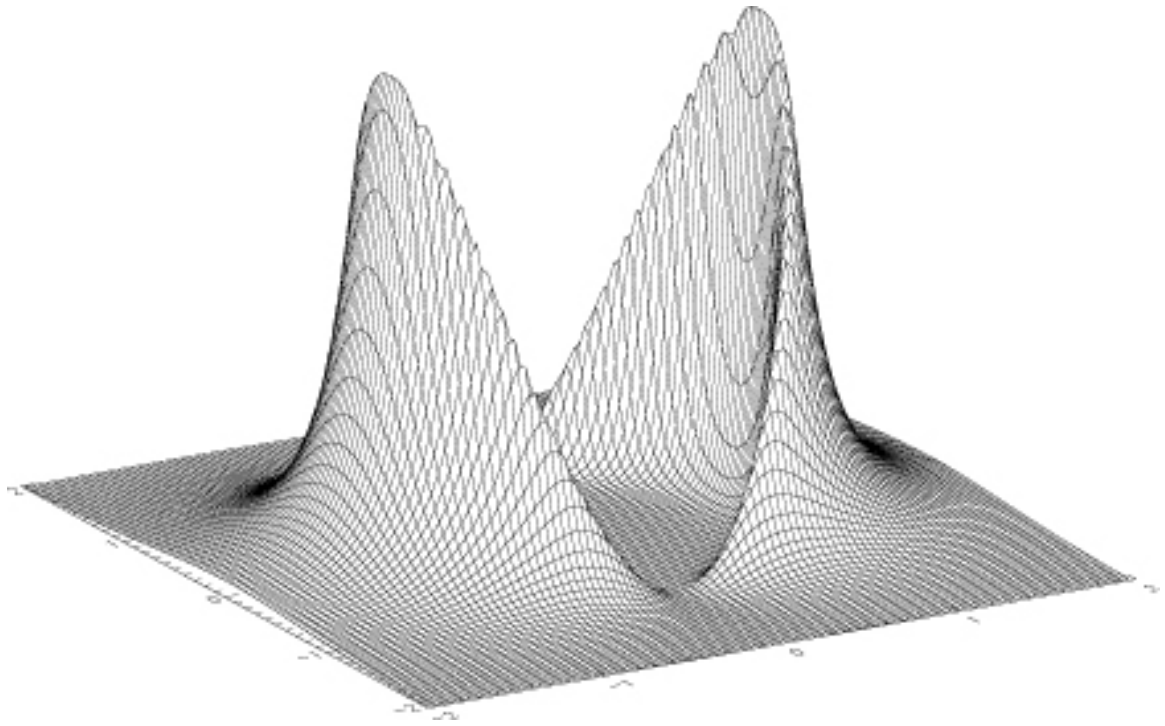


Figure 2.10: z -polarized light near a sub-wavelength aperture

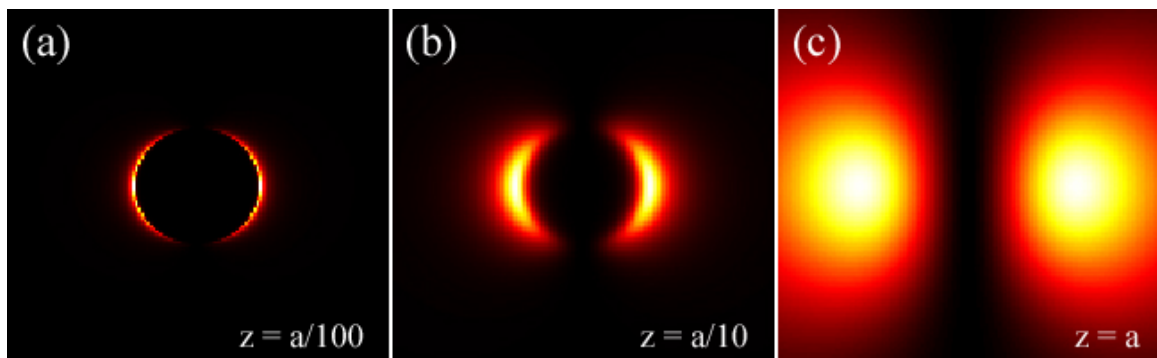


Figure 2.11: z -polarized light at various distances from a sub-wavelength aperture

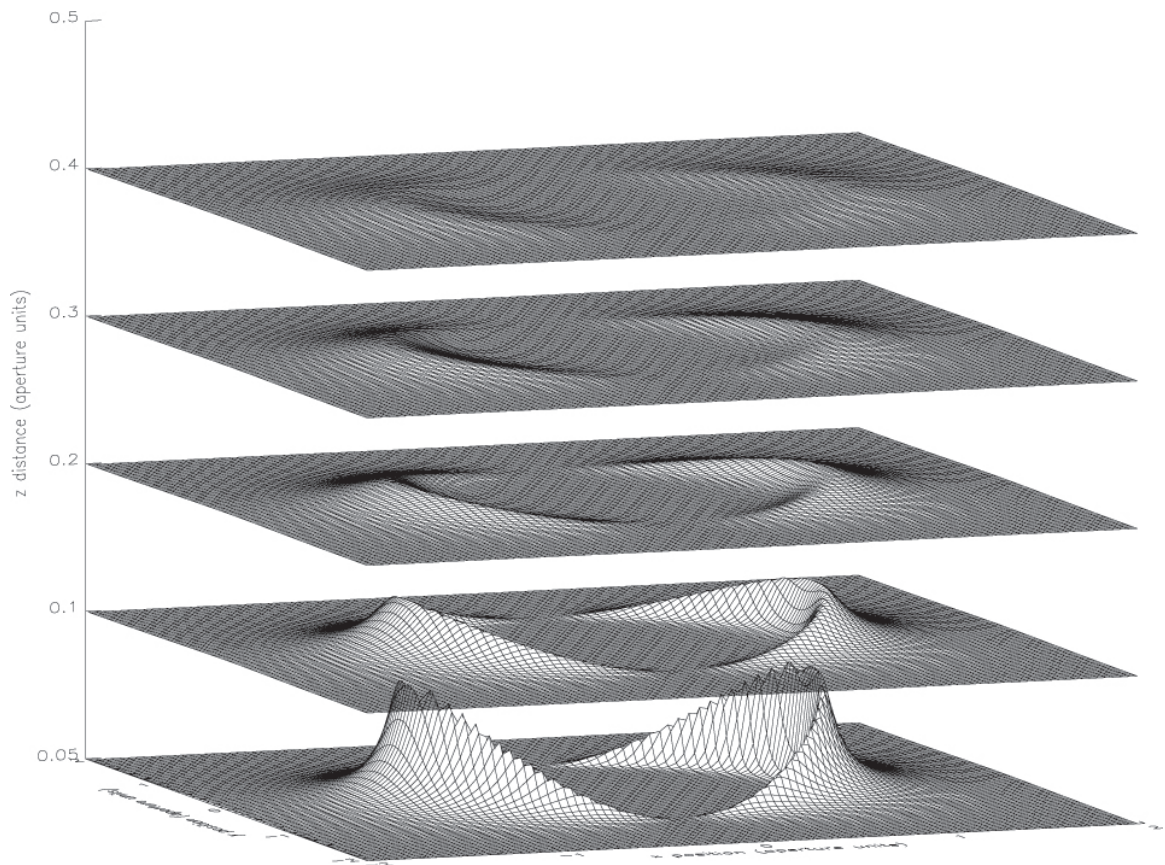


Figure 2.12: z -polarized component E_z^2 , showing change with distance from the aperture

Chapter 3

The Split-Tip Probe

Proximal probe lithography has been used for several years. Early work included using an scanning tunneling microscope (STM) as an electron source with e-beam resists [4] or for electron-assisted chemical vapor deposition, [5] single atom manipulation at low temperature [6] or room temperature [7, 8], the creation of gold bumps on a surface with an STM current pulse, [9] and the growth of single layer high gold terraces on the bottom surface of a gold film with hot electrons injected from an STM tip, and their observation with ballistic electron emission microscopy (BEEM). [10-13] More recent examples of high lateral resolution patterning with proximal probes includes optical modification of materials with a near-field scanning optical microscope (NSOM), [14, 15] and 'dip-pen' nanolithography with an atomic force microscope (AFM). [16] Although the resolution of many of these probe methods is very high, the interactions with the samples are symmetric, so lateral (in the plane of the sample) orientation cannot be controlled. This issue can be addressed by employing the use of a nonsymmetric 'split-probe' to control orientation through a proximal probe interaction while maintaining nanometer-scale resolution. This added dimension of control represents a significant advance.

The split-tip probe, which is mounted onto a standard scanning proximal probe microscope, consists of two electrically isolated and independently contacted metal electrodes deposited on opposite sides of a tapered optical fiber, similar to those used for near-field scanning optical microscopy (NSOM). An electron microscope image of one of these split-tip probes is shown in figure 3.1. We use Al or Au for these tips. The NSOM system has the required optical hardware for coupling laser light into the region between the split-tip electrodes, which is exactly where it is needed for initiating the deposition to

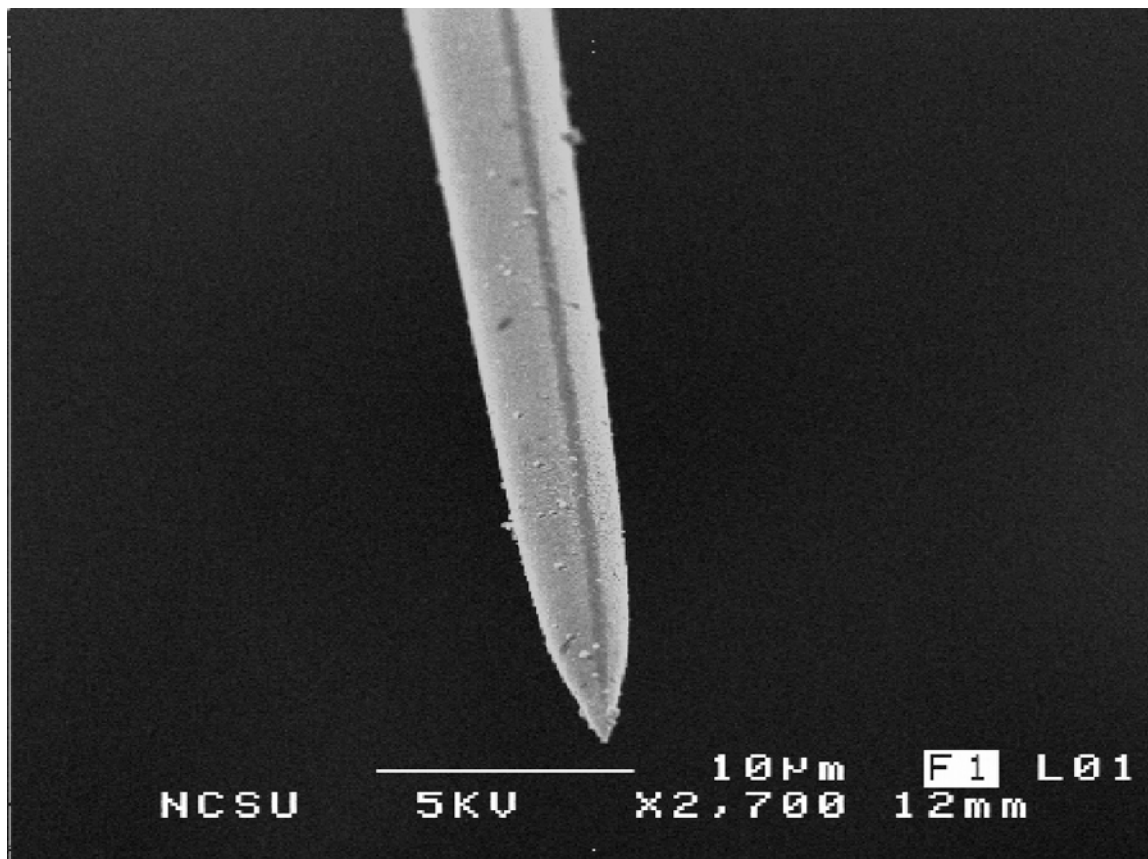


Figure 3.1: The electrodes are on the left and right sides, and the aperture is visible at the bottom.

the surface. The probe not only guides the deposition, but can characterize the quality of the resulting material by:

1. measurement of topography by the NSOM-like scanning probe, or
2. measuring orientation with polarization-dependent NSOM imaging with the probe that is also used for deposition.

3.1 Design Requirements

Before we describe the fabrication of the probe, we briefly describe the deposition scheme that it will be used for and some of the other criteria that impact the design of the probe. A schematic of the probe tip near the sample as molecules are being deposited with

a fixed orientation to the sample surface is shown in figure B.2. In this cut-away view, the

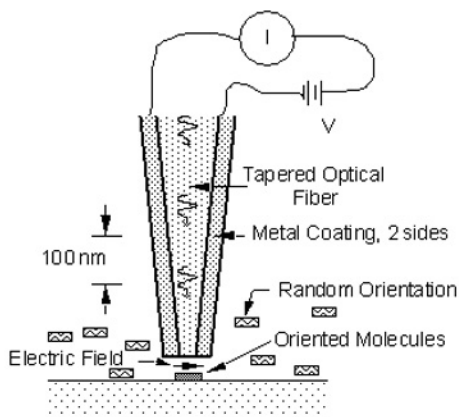


Figure 3.2: A schematic of the probe illustrates the major features.

electrodes are on the left and right sides of the tip. The electric field is localized in the region of the split, and is highest where the split is narrow - near the tip apex. Molecules that are in solution will be oriented where the field is high, but not elsewhere. When the tip moves to a new location, it aligns the molecules, then initiates the deposition to the sample with a pulse of ultraviolet light. The tip then moves to a new location, orients the molecules as they should be in the new location, and links them to the surface. It is important that molecules not under the probe tip do not attach to the surface, since they are not oriented. The schemes for insuring this are below. The molecules are shown in solution. This is not necessary. They could also be deposited 'dry' onto the surface, those in the regions of interest be rotated by the field and linked to the surface, then the remainder washed off. Another alternative is to load the tip with molecules as in the 'dip-pen' lithography scheme, [16] oriented and attached as in liquid, then another molecule chosen for a different position.

The requirements for the tip are therefore that two electrodes must be electrically isolated from each other, that ultraviolet light must be able to propagate through the probe to the region between the electrodes, that deposition must not occur on the probe itself, that the probe must be compatible with a microscope system, that the probe must not be 'shorted' by the solution or the molecules that are in the solution, that the probe be usable

in a probe-surface distance regulation scheme and that the probe have a reasonable lifetime.

3.2 Probe Fabrication

Our 'split-tip' probe resembles an NSOM probe, and it is fabricated using a process similar to that used for our NSOM tips, but with a few significant differences that make the process work. We use either a Sutter Instruments puller, modified to work better with

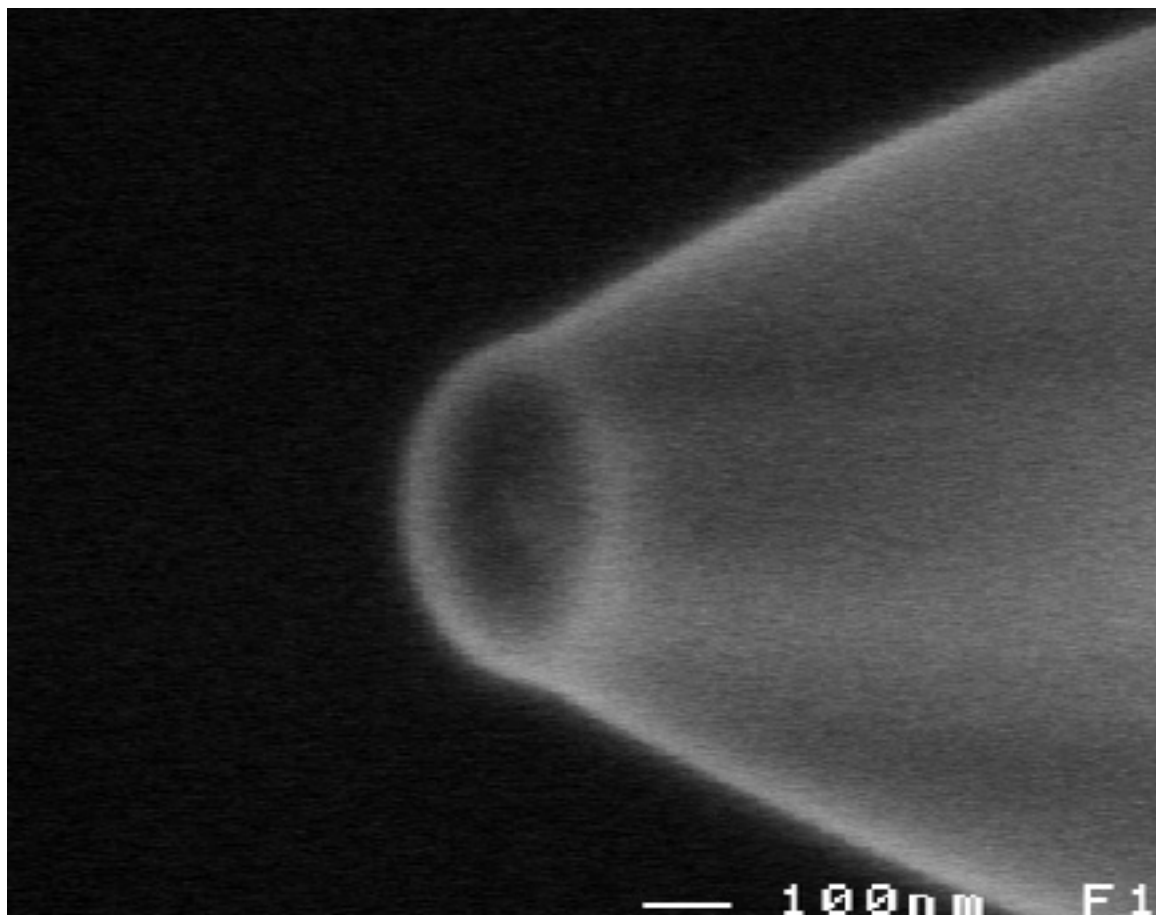


Figure 3.3: SEM image of a larger-aperture tapered fiber fabricated by the heat-and-pull method. Note the flat cleaved end that is formed when this fabrication scheme is used, as opposed to the sharp point of etched fibers.

fibers, [29-32] or chemical etching [33] to taper the end of an optical fiber. We need to pull the fibers when we want a large separation of the electrodes, since the fiber gets a flat face as it cleaves in the fiber pulling apparatus, as can be seen in figure A.3. This shape

contrasts with the sharp point at the tip of properly-etched fibers. Thus, if the electrodes are to be brought in close proximity to the surface, they need to be close together with etched fibers, but may be further apart when pulled fibers are used. Etched fibers are more reproducible to fabricate in large quantities, and have a higher optical throughput. We

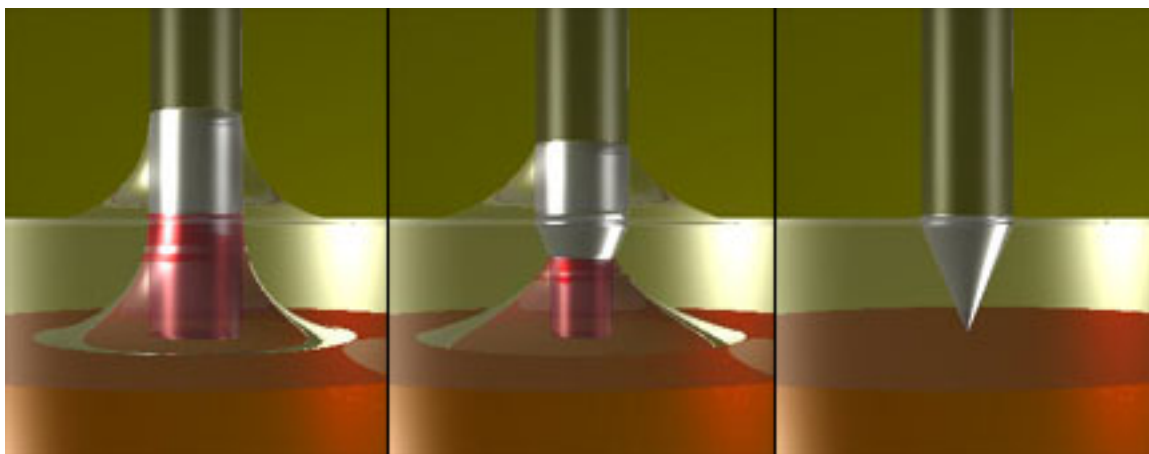


Figure 3.4: The Etching Process

initially used only pulled fiber probes for the fabrication of split-tip probes, since we were concerned that the electrodes might short near the tip, but we now use both types without shorting problems.

Once the fibers are shaped, metal is coated on one side, then the fiber rotated 180, and the other electrode is deposited. This forms a split metal structure with the two metal sides electrically isolated. The metal coating must be thin so that the two sides do not short together. Our probe-holding fixture, shown in figure ???, in the deposition chamber allows an accurate flipping of the probes in vacuum. The probes are mounted on holders that keep the probes straight and separated by a sufficient distance that they do not shadow each other during evaporation. Between 8 and 10 probes are held in each unit. Two units can be used at once in the evaporator system, facing each other. The probe holder is mounted on a large gear, and the fiber tails run through a series of holders, also mounted on the gear, in the direction so that they do not unravel during the rotation of the gear. The gear is turned by a smaller gear attached to a small electric motor. We have found that the motors work reliably in vacuum when they are driven by a voltage lower than their maximum rating, which also has the advantage that they spin more slowly. Although it is commonly taught

that the back-voltage generated by the motor limits the current and that lower voltages result in motor over-current failure, we have found that the current is limited primarily by the resistance of the wires, when the motors are under load. We have found that motor failure is usually the result of shorting from metal deposition or an increase in friction in the mechanism, often due to effects of metal deposition. The two gears provide a reduction of the motor rotation by a factor of. Copper braiding attaches the axle of the larger gear shaft to a liquid nitrogen cold trap mounted directly over the rotation units. In this way, the fibers can be cooled by radiation (with approximately π steradian of solid angle towards the cold trap) or by conduction through the Cu braids, shaft, gear, holder, and fiber shanks. The evaporation chamber allows three different source materials can be used during one pump-down. We use Al or Au. Following the initial deposition, a thicker coating of gold is applied to the contact regions on the shank of the tip. A small shutter, figure ???, driven by an in-vacuum electric motor is used to shield just the probe tips from the evaporation source, so that the shanks are coated with metal. A close-up view of the split-tip probe can be seen in Fig. 1, and a view at lower magnification is given in Fig. 5. A significant challenge in the fabrication process is insuring a well-defined split and a continuous coating of metal down to the aperture of the probe. The reason why this is much more difficult than for NSOM tips is that the metal forms a continuous ring around the diameter of the NSOM probe. If there is stress in the metal layer, the film itself will hold the stress. When the metal is evaporated, the stress is typically tensile [ref]. This means that the metal will try to pull itself apart from the probe. If the metal is continuous, it will pull on itself, and usually remain stable. In the split tip, the metal is not continuous, so the stress must be held by the interface between the film and the underlying silica. Far from the tip, this is possible since the area is large, but as the tip is approached, the area is reduced and the curvature increased. We see process in the series of SEM micrographs, figure ??????. There appears to be a near perfect split in our split tip at low magnification. Figure 3.5 shows the tip at a magnification of $X 95$. The split appears well defined, but it is crucial to see this type of behavior at the aperture of the probe, rather than up the shaft. As we approach the probe aperture, we see certain imperfections, likely voids in the coating. At $X 2000$ magnification, we see cracking and peeling, which presents a significant problem. See figure 3.6.

The curling near the aperture, along with the observed cracking of the probe coating suggests the coating, a thin film of Al, experiences stress due to the differences in

thermal expansion (thermal stress) between the Al and the glass fiber. In general, stress in films results from the differences in thermal expansion (thermal stress) or from the microstructure of the deposited film (intrinsic stress). At substrate temperatures less than 20% of the melting point, intrinsic stress due to incomplete structure ordering dominates. Intrinsic stress results from the microstructure created in the film as atoms are deposited on the substrate. Tensile stress results from micro-voids in the thin film, because of the attractive interaction of the atoms across the voids. Thermal stress occurs because film depositions are usually made above room temperature. Upon cooling from the deposition temperature to room temperature, the difference in the thermal expansion coefficients of the substrate and the film causes thermal stress.

We can estimate the temperature rise in the probe with a simple calculation. The first process that can heat the probe is energy deposited by the metal evaporant, which is given by the evaporation rate onto a flat, untilted surface R ($1nm/s$) where the tip is, an angle correction $\cos(\theta + \psi)$ for the tip with half-angle ψ (6°) tilted up at angle θ (45°), the heat capacity c ($400J/kg/K$ for Al), density ρ ($2700kg/m^3$), temperature change T ($800K$ above ambient estimated by evaporant color), and area of the film A (at distance z from the tip):

$$\text{Energy input} = R\rho c\Delta T A \cos(\theta + \psi) \quad (3.1)$$

with

$$A = 2\pi z \frac{dz}{\cos\psi \tan\psi} \quad (3.2)$$

The second process that can heat the tip is radiation from the thermal evaporation source. Radiative heating power is given by

$$P = \rho A \varepsilon (T^4 - T_o^4) (SA) \quad (3.3)$$

which is also proportional to the area. The emissivity ε is approximately 0.06 for shiny aluminum and 0.8 for the glass fiber. The transition will take place in the first few nm of deposition. We calculate for a temperature of $930K$, a solid angle of $SA \sim 10^{-5}$, that the contribution from radiative heat-into the same area as for evaporation is about an order of magnitude smaller. Both have the same area-factor, so will enter the equations similarly. Cooling is primarily by conduction up the fiber taper, as determined by:

$$\nabla^2 T - \frac{\rho c}{\kappa} \frac{dT}{dt} = \frac{Q}{\kappa} \quad (3.4)$$

where κ ($1.5W/m/K$) is the thermal conductivity of quartz, ρ the density, c the heat capacity, and Q the thermal energy per volume. In steady state, the time derivative vanishes. Since the taper is a cone to a good approximation, and since symmetry and lack of significant radiation (and no convection) implies we can convert the thermal problem to one of spherical symmetry, with the energy input per volume given by that in equation (1) scaled by the inverse of the fraction of solid angle taken by one tapered fiber: $2/(1 - \cos \psi)$. This assumes that the energy is uniformly input, rather than at the sides of the taper, but is justified by the relatively shorter lateral thermal times. The energy input in (1) is divided by the volume of a shell at a radius z to get

$$\frac{Q}{\kappa} = \frac{R\rho c\Delta T \cos(\theta + \psi)}{\kappa(1 - \cos \psi) \cos \psi \tan \psi} \frac{1}{z} = D \frac{1}{z} = 633 K/m \frac{1}{z} \quad (3.5)$$

Equation (2) in spherical coordinates becomes, for steady state and uniform in angle,

$$\frac{1}{z^2} \frac{\partial}{\partial z} \left(z^2 \frac{\partial T}{\partial z} \right) = \frac{Q}{\kappa} \quad (3.6)$$

This is solved by a function of the form $T = A/z + B + Cz$. We set the derivative equal to zero at the end of the taper L ($0.5mm$) to indicate the reduction in heat flow at the end of the cone, and set the temperature at the end of the taper to ambient, T_o . This implies

$$T = D \frac{L^2}{2} \left(\frac{1}{z} \right) + T_o - DL + \frac{D}{2} z \quad (3.7)$$

Near the end of the fiber, the last two terms are small, and at $z = 1 \text{ micron}$, the temperature rise is $\sim 150K$ above ambient. When we cool the liquid nitrogen cold trap, we find that the temperature of the fiber holder decreases between 120 and 150K below ambient. Thus, the region near the probe tips during evaporation is at or reasonably close to room temperature during evaporation. This is what is required to minimize thermally induced stress.

Figure 3.7 shows the probe at $X 11,000$ magnification, clearly indicating the we are dealing with a case of tensile stress. The aluminum film on the right side of the split tends to bow in a few spots. We also see from this micrograph that tensile stress will relieve itself by microcracking of the film and the peeling of the cracked surface from the substrate. The stress distribution in this film is anisotropic; there are cracking patterns that depend on the stress distribution.

The most common way for measuring film stress is by measuring the deflection (bowing) of a thin film substrate (beam or disc) on which the film has been deposited. This is not possible here, since the substrate is much thicker than the film itself, the substrate is

coated on more than one side, and hence, no bowing seems to have occurred. Nevertheless, assuming knowledge of the mechanical properties of the substrate and film, film thickness, and the deflection, we can calculate the film stress. In particular, the film stress, σ_f , for a film of thickness t_f and Young's modulus E_f on a substrate of thickness t_s and Young's modulus E_s curved with a radius ρ and distances from the neutral plane to the point in the film and substrate of Y_f and Y_s respectively, is given by:

$$\sigma_f = \frac{t_f E_s}{5\rho} \left[\left(\frac{t_s}{t_f} \right)^2 + 6 \left(\frac{E_f}{E_s} \right) \left(\frac{Y_f}{t_f} \right) \right], \text{ where } -\frac{1}{2} \leq \frac{Y_f}{t_f} \leq \frac{1}{2} \quad (3.8)$$

The substrate stress σ_s is likewise given by:

$$\sigma_s = \frac{t_s E_s}{6\rho} \left[1 + 6 \left(\frac{Y_s}{t_s} \right) \right], \text{ where } -\frac{1}{2} \leq \frac{Y_s}{t_s} \leq \frac{1}{2} \quad (3.9)$$

Large film stresses often result in adhesion failure (de-adhesion), especially when the film has a high modulus or the thickness is large. Hence, we have identified two major contributors to our tensile stress problem:

1. Difference in heating and cooling rates of the substrate and film upon deposition; i.e., the difference in thermal expansion.
2. Film thickness regulation; i.e., the rate of film deposition.

The small size of the probe tip represents a particular problem, since its thermal mass is small - comparable to the thermal mass of the deposited film. This means that the tip end will heat significantly during the film growth process, from both radiative effects and energy carried by the metal evaporant, unless special care is take to prevent it. Tip heating means that significant thermal stress will result when the tip plus film cool to room temperature. We address these issues by simply doing the following:

1. Depositing a very thin aluminum film near the tip, on the order of 10 *nm*. Thus, tensile stress is reduced by avoiding a large value for t_f . Our substrate-film heating is also minimized, since the deposition duration is short.
2. Keeping the cold trap within the bell jar of the deposition chamber filled with liquid nitrogen, providing radiative and conduction cooling of the probe tips. This allows us to increase the rate of substrate and film cooling. This process facilitates the short deposition duration mentioned in (1).

3. Waiting 2-3 minutes for complete cooling and stabilization.
4. Repeating until desired thickness is achieved.
5. Apply a thicker coating (100–200nm) to the contact pads so that they will be reliable under repeated use.

These steps minimize the thermal stress by keeping the tip as close as possible to room temperature during the deposition as is possible, through cooling and reduced thermal input. The stress is less important for the contacts, since they are in the region where the fiber is its full size, with sufficient thermal mass to prevent significant thermal variation.

The result yields well defined 'split' behavior in our probes with no sign of stress conditions previously observed. At greater magnifications (Figure 3.8), we are able to observe the detailed features of the aperture to display the consistency and control of both the split and the deposition of the material used (*Al*). We also observe residual material in the split of the probe, away from the aperture. This threatens the required isolation of the electrodes that we have deposited on either side of the probe, but is not unexpected. Mathematically, one expects a perfectly-aligned deposition to uniformly ($\cos \theta$) approach zero at the point where the probe surface is perpendicular to the evaporation source. Lack of isolation will result in the two sides shorting together. The effect is most dramatic very near the tip, where the distances involved are short. Figure 3.9 provides a detailed view of the split. The split is, in fact, not completely void, but contains small grains of material. The grains are sparse within the split and vary in size from a few nm to tens of nm. The fact that the material is sparse and composed of 'balls' and individual grains (not a relatively smooth coating) is likely due to Ostwald Ripening or coarsening. The metal nucleates as small, dispersed particles initially, but the smaller particles slowly disappear as materials 'evaporates' onto a few that grow relatively large. The smaller particles act as "nutrients" for the larger particles. As the larger particles grow, the area around them is depleted of metal. This is a spontaneous, diffusion process that occurs because large particles are more energetically favored than smaller ones.

Another factor that improves the electrical isolation is oxidation. Very thin metal within the split will be completely oxidized (if we use *Al*). This can be enhanced by exposing the probes to a few hundred *mTorr* of pure oxygen for 1/2 hour [ref: I have one] as a preliminary to venting the system. We follow this process with *Al* probes.

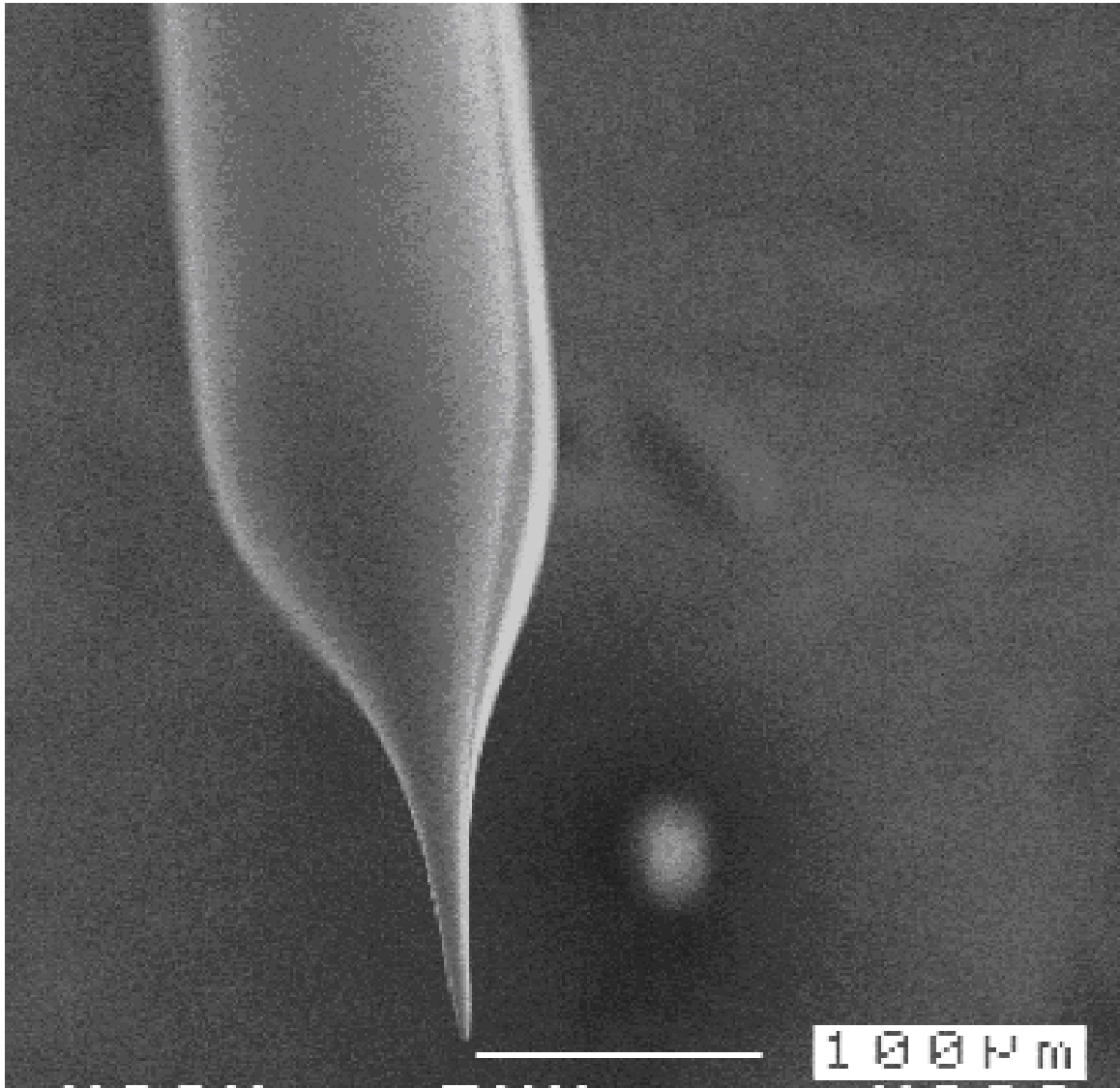


Figure 3.5: At $X 95$, the "split" looks deceptively well behaved.

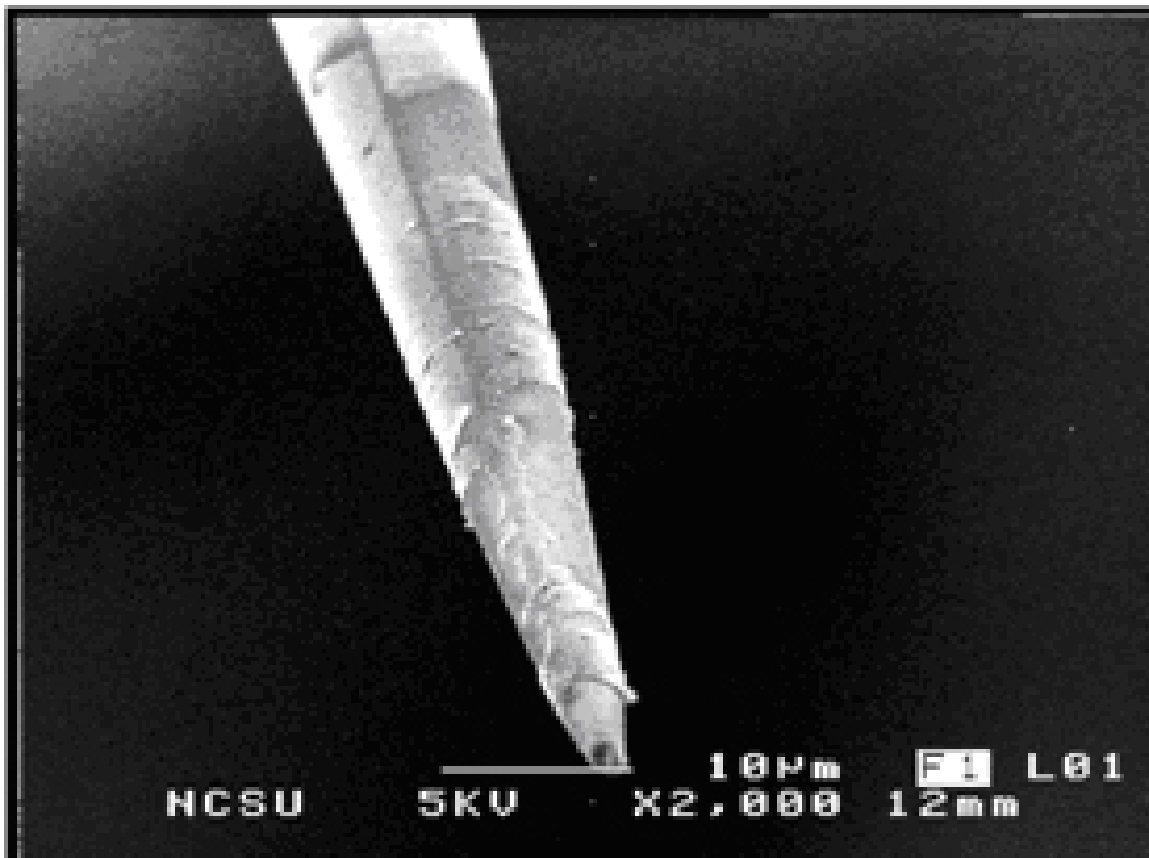


Figure 3.6: This X 2000 magnification view, shows significant damage and peeling toward the apex of the probe.

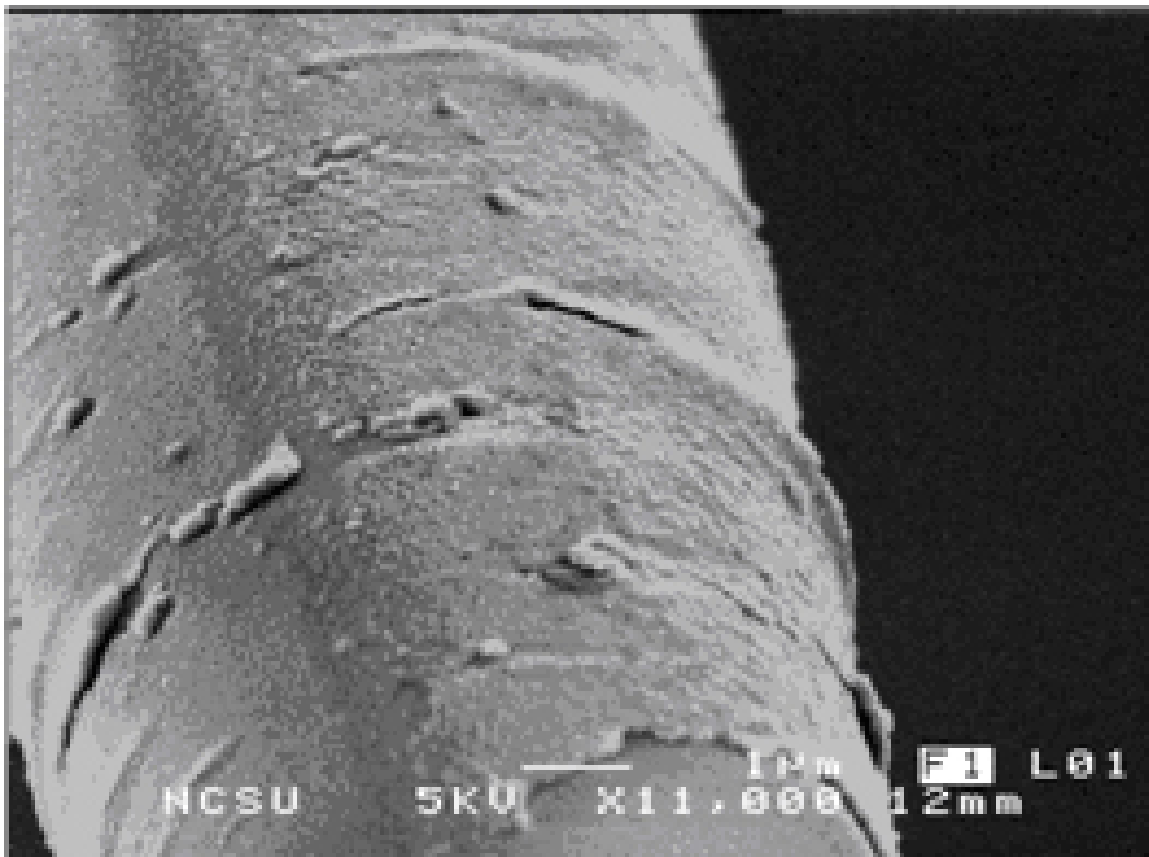


Figure 3.7: This X 11000 magnification view, shows significant damage due to tensile stress.

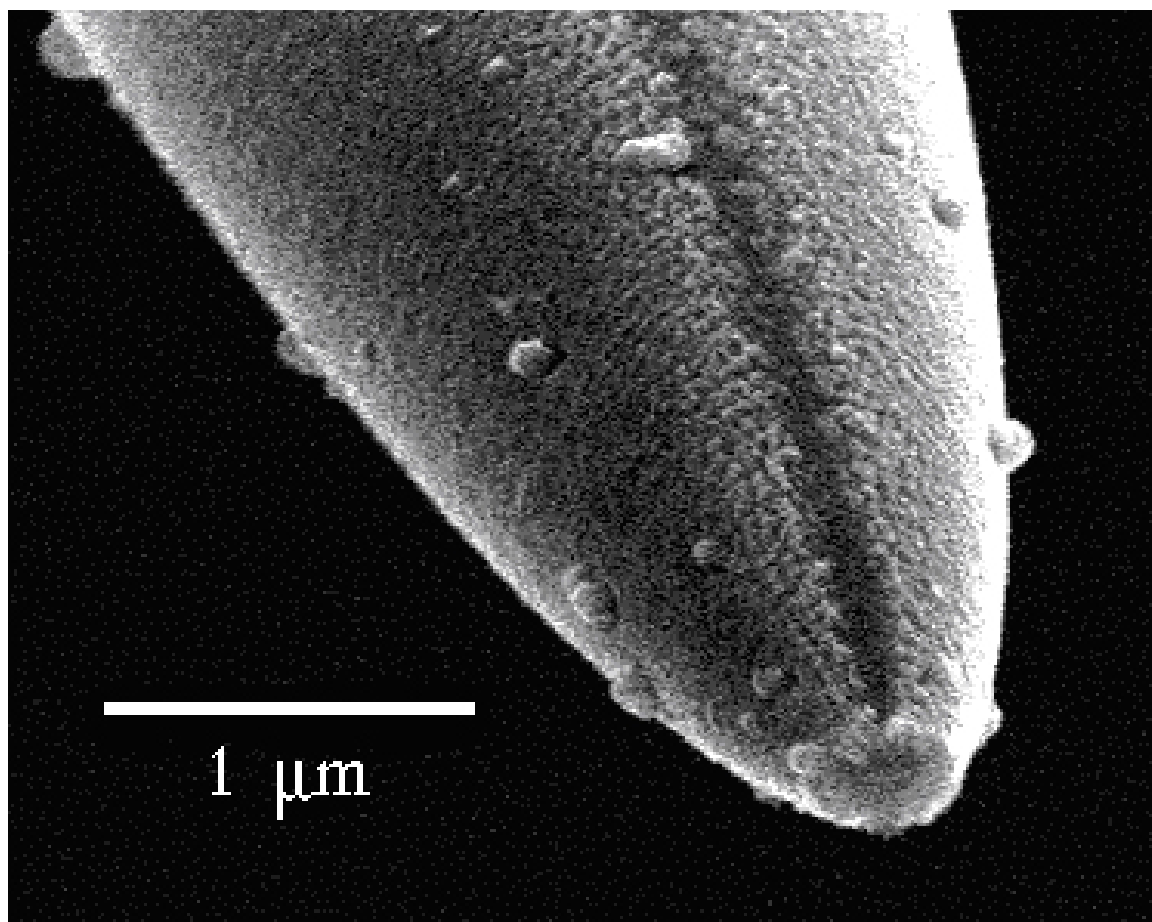


Figure 3.8: With the proper approach to the fabrication process, the integrity of the split can be seen down to aperture ($\sim 100\text{ nm}$ in diameter).

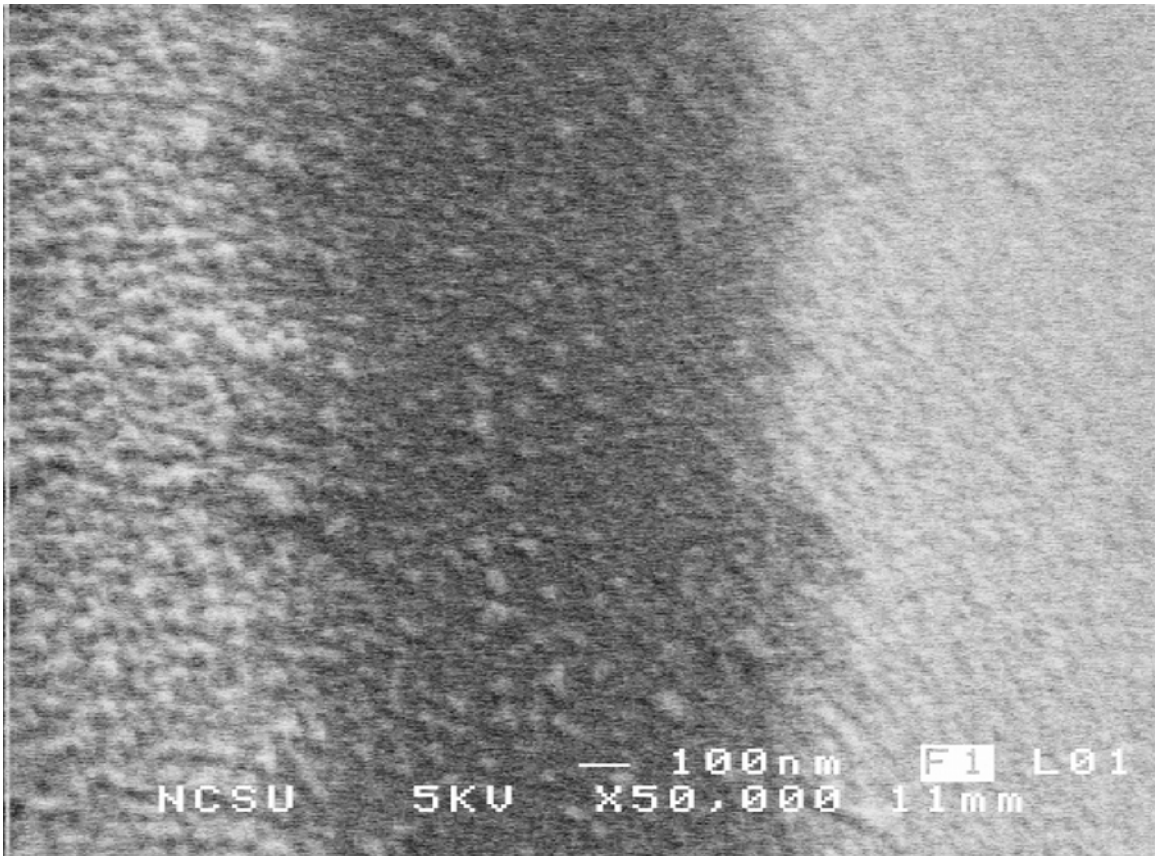


Figure 3.9: This X 50000 magnification view, reveals the fact that the split is not completely void of material.

Chapter 4

Modeling The Tip

4.1 Mathematical Modeling

Mathematical modeling has been used as a tool to understand various dynamical processes for centuries. However, the marriage of computer technology and mathematical modeling has recently allowed researchers to investigate problems that were once described as impossible and frivolous tasks. The ability to study system dynamics with elegance, speed and accuracy has been a great benefit for the advancement of scientific research.

While mathematics is undoubtedly a powerful tool, its power must be handled with great care and the highest respect when modeling. To use models properly requires not only an understanding of mathematics, but also a fundamental knowledge of the dynamic process under study. Once a mathematical model is developed for a particular system, this does not constitute the end of the problem. In fact, modeling can be thought of as an iterative process. After a model is constructed, it must be tested (preferably against real experimental data) for validity. This step is followed by continuous refinement until the mathematical model mimics the dynamical process as accurately as computationally possible.

Although computational mathematics has several advantages, the disadvantages must also be acknowledged. Nature (and other mechanical processes) is very complex and often involves several highly coupled dynamics all happening at once. Thus when building a mathematical model, the investigator must be careful not to construct a model that can not be understood at each intermediate step. To this end, assumptions in the development of a model may be physical, biological or purely mathematical [1]. It is quite common for

researchers to impose restrictions on the model that compromises the true dynamics of the process. Otherwise, the model will be intractable and no further insight into the phenomena under scrutiny will be gained.

4.2 Modeling the Split-Tip

The flat end of the split-tip probe defines the deposition region between the electrodes. Its size can be from several hundred nanometers down to $\sim 10nm$. We can estimate the field strength if we assume a flat capacitor model. For example, a $50nm$ tip with $0.5V$ applied would have a field of order $10^7V/m$. This is a very large electric field, and it is therefore not surprising that we have, on occasion, found that the probe tip is damaged by the high fields. We observe this as an irreversible change in our ability to control the polarization of the light emanating from the probe. It results from damage to the silica. The result illustrates two points:

1. Damage, or breakdown, is possible only when an energy threshold, or voltage threshold if the electrons are emitted from a conductor. A clean system has a very large breakdown system, since lower energy electronic states are not available. Thus, huge electric fields are possible with the nano-split-tip. Even if the minimal voltages are exceeded, breakdown usually doesn't occur until a fluctuation aids the process. A likelihood of a large fluctuation in a nanoscale volume is small, so even larger fields may be possible.
2. We can apply very large fields to the molecules that are being oriented. This is a common occurrence in nanoscale science, when distances get small, and results in new physics as energetic electrons can be injected into materials - potentially causing damage [13, 14, ,].

These fields can allow access to nonlinearities in the electric field interaction. We will probably not need to use fields this large for orienting molecules, but it is important not to exceed the probe damage thresholds in order not to cause artifacts in the following optical characterization. The high fields may be useful for inducing bonding to the surface, although we do not expect to require them.

4.3 Cartesian Coordinates

A simple estimate in cartesian coordinates: an infinitely long, rectangular box (or waveguide) along the z -axis, with a potential V at $x = \pm b$ and $V = 0$ at $y = 0, a \dots$

$$V(\phi, z) = \begin{cases} -V & \text{for } x = 0 \\ V & \text{for } x = a \\ 0 & \text{for } y = 0 \\ 0 & \text{for } y = a \\ 0 & \text{for } z = 0 \\ 0 & \text{for } z = a \end{cases}$$

We seek a solution to Laplace's equation in cartesian coordinates:

$$\nabla^2 \Phi = 0 \Rightarrow \frac{\partial^2 \Phi}{\partial x^2} + \frac{\partial^2 \Phi}{\partial y^2} + \frac{\partial^2 \Phi}{\partial z^2} = 0 \quad (4.1)$$

We will try a solution of the form $\Phi(x, y, z) = X(x)Y(y)Z(z)$.

$$\nabla^2 \Phi \Rightarrow X''(x)Y(y)Z(z) + X(x)Y''(y)Z(z) + X(x)Y(y)Z''(z) = 0 \quad (4.2)$$

Divide by $X(x)Y(y)Z(z)$ to get

$$\nabla^2 \Phi = \frac{X''(x)}{X(x)} + \frac{Y''(y)}{Y(y)} + \frac{Z''(z)}{Z(z)} = 0 \quad (4.3)$$

Applying the boundary conditions to this expression will result in two inhomogeneous equations; therefore, we must break our original problem into two separate problems, each yielding only one inhomogeneous expression upon applying the boundary conditions.

Problem 1:

$$V(\phi, z) = \begin{cases} 0 & \text{for } x = 0 \\ V & \text{for } x = a \\ 0 & \text{for } y = 0 \\ 0 & \text{for } y = a \\ 0 & \text{for } z = 0 \\ 0 & \text{for } z = a \end{cases}$$

In equation 4.3, \exists a constant $\lambda + \mu \ni$

$$\frac{X''(x)}{X(x)} = \lambda^2 + \mu^2, \frac{Y''(y)}{Y(y)} = -\mu, \frac{Z''(z)}{Z(z)} = -\lambda \quad (4.4)$$

$$\frac{\partial^2 Y}{\partial y^2} - \mu^2 Y = 0 \quad (4.5)$$

has solution

$$Y = A \sin(\mu y) + B \cos \mu(y) \quad (4.6)$$

The solution must satisfy boundary conditions that $\Phi = 0$ at $y = 0, L$. Therefore, B must vanish. Hence,

$$Y = A \sin(\mu y), \text{ where } \mu = \frac{m\pi}{a}, m \in \mathbb{Z}^+ \quad (4.7)$$

Similarly, we have for Z

$$\frac{\partial^2 Z}{\partial \phi^2} - \lambda^2 Z = 0 \quad (4.8)$$

which has solution

$$Z = C \sin(\lambda z), \text{ where } \lambda = \frac{l\pi}{a}, l \in \mathbb{Z}^+ \quad (4.9)$$

Now,

$$\frac{\partial^2 X}{\partial x^2} - (\lambda^2 + \mu^2)X = 0 \quad (4.10)$$

has solution

$$X = E \sinh\left(\sqrt{\lambda^2 + \mu^2}x\right) + F \cosh\left(\sqrt{\lambda^2 + \mu^2}x\right) \quad (4.11)$$

Satisfying the boundary condition, $\Phi = 0$ at $x = 0$, we have

$$X = E \sinh\left(\sqrt{\lambda^2 + \mu^2}x\right) \quad (4.12)$$

We can now write Φ in a general form:

$$\Phi(x, y, z) = X(x)Y(y)Z(z) = \sum E \sinh\left(\sqrt{\lambda^2 + \mu^2}x\right) A \sin\left(\frac{m\pi}{a}y\right) C \sin\left(\frac{l\pi}{a}z\right) \quad (4.13)$$

Let E, A, and C be absorbed into one coefficient, G. Then,

$$\Phi(x, y, z) = \sum_{l=1}^{\infty} \sum_{m=1}^{\infty} G_l m \sinh\left(\sqrt{\lambda^2 + \mu^2}x\right) \sin\left(\frac{m\pi}{a}y\right) \sin\left(\frac{l\pi}{a}z\right) \quad (4.14)$$

This expression for Φ satisfies all homogeneous conditions for any choice of $G_l m$, provided that the resulting series converges. To find $G_l m$, we use the inhomogeneous condition at $x = a$.

$$\Phi(a, y, z) = \sum_{l=1}^{\infty} \sum_{m=1}^{\infty} G_{lm} \sinh\left(\sqrt{\lambda^2 + \mu^2}a\right) \sin\left(\frac{m\pi}{a}y\right) \sin\left(\frac{l\pi}{a}z\right) \quad (4.15)$$

To solve for G_{lm} , we multiply both sides by $\sin(m\pi/a)y \sin(l\pi/a)z$ and integrate from 0 to a . This yields

$$G_{lm} = \begin{cases} 0 & \text{for } l, m \text{ even} \\ \frac{16V}{lm\pi^2 \sinh\left(\sqrt{\left(\frac{l\pi}{a}\right)^2 + \left(\frac{m\pi}{a}\right)^2}a\right)} & \text{for } l, m \text{ odd} \end{cases}$$

So, let $l = 2n - 1$ and $m = 2p - 1$ for $n, p, \in \mathbb{Z}^+$. Then,

$$G_{np} = \frac{16V}{(2n-1)(2p-1)\pi^2 \sinh\left(\sqrt{\left(\frac{(2n-1)\pi}{a}\right)^2 + \left(\frac{(2p-1)\pi}{a}\right)^2}a\right)}, \text{ for } n, p \in \mathbb{Z}^+ \quad (4.16)$$

Hence,

$$\Phi_1(x, y, z) = \frac{16V}{\pi^2} \sum_{n,p} \frac{\sin\left[\frac{(2n-1)\pi z}{a}\right] \sin\left[\frac{(2p-1)\pi y}{a}\right] \sinh\left(\sqrt{\left(\frac{(2n-1)\pi}{a}\right)^2 + \left(\frac{(2p-1)\pi}{a}\right)^2}x\right)}{\sinh\left(\sqrt{\left(\frac{(2n-1)\pi}{a}\right)^2 + \left(\frac{(2p-1)\pi}{a}\right)^2}a\right)} \quad (4.17)$$

Problem 2:

$$V(\phi, z) = \begin{cases} -V & \text{for } x = 0 \\ 0 & \text{for } x = a \\ 0 & \text{for } y = 0 \\ 0 & \text{for } y = a \\ 0 & \text{for } z = 0 \\ 0 & \text{for } z = a \end{cases}$$

The approach is the same as in problem 1, with the exception that $x \rightarrow a - x$. This yields

$$\Phi_2(x, y, z) = \frac{16V}{\pi^2} \sum_{n,p}^{\infty} \frac{\sin\left[\frac{(2n-1)\pi z}{a}\right] \sin\left[\frac{(2p-1)\pi y}{a}\right] \sinh\left(\sqrt{\left(\frac{(2n-1)\pi}{a}\right)^2 + \left(\frac{(2p-1)\pi}{a}\right)^2} (a-x)\right)}{\sinh\left(\sqrt{\left(\frac{(2n-1)\pi}{a}\right)^2 + \left(\frac{(2p-1)\pi}{a}\right)^2} a\right)} \frac{\sinh\left(\sqrt{\left(\frac{(2n-1)\pi}{a}\right)^2 + \left(\frac{(2p-1)\pi}{a}\right)^2} (a-x)\right)}{\sinh\left(\sqrt{\left(\frac{(2n-1)\pi}{a}\right)^2 + \left(\frac{(2p-1)\pi}{a}\right)^2} a\right)} \quad (4.18)$$

Finally, the sum of the two results ($\Phi_1 + \Phi_2$) gives us

$$\begin{aligned} \Phi(x, y, z) &= \frac{16V}{\pi^2} \sum_{n,p}^{\infty} \frac{\sin\left[\frac{(2n-1)\pi z}{a}\right] \sin\left[\frac{(2p-1)\pi y}{a}\right]}{\sinh\left(\sqrt{\left(\frac{(2n-1)\pi}{a}\right)^2 + \left(\frac{(2p-1)\pi}{a}\right)^2} a\right)} \\ &\times \left\{ \sinh\left(\sqrt{\left(\frac{(2n-1)\pi}{a}\right)^2 + \left(\frac{(2p-1)\pi}{a}\right)^2} (x)\right) \right. \\ &\left. - \sinh\left(\sqrt{\left(\frac{(2n-1)\pi}{a}\right)^2 + \left(\frac{(2p-1)\pi}{a}\right)^2} (a-x)\right) \right\} \quad (4.19) \end{aligned}$$

4.4 Cylindrical Coordinates

We get a better estimate of the electric field at probe tip by considering a hollow right cylinder of radius a with its axis fixed along the z -axis. The surface is made of two equal half-cylinders, one at potential V and the other at potential $-V$, so that

$$V(\phi, z) = \begin{cases} V & \text{for } -\frac{\pi}{2} < \phi < \frac{\pi}{2} \\ -V & \text{for } \frac{\pi}{2} < \phi < \frac{3\pi}{2} \end{cases}$$

The potential on the end faces is *zero*.

We start with Laplace's equation:

$$\nabla^2 \Phi = 0 \Rightarrow \frac{1}{r} \frac{\partial}{\partial r} \left(\frac{1}{r} \frac{\partial \Phi}{\partial r} \right) + \frac{1}{r^2} \frac{\partial^2 \Phi}{\partial \phi^2} + \frac{\partial^2 \Phi}{\partial z^2} = 0 \quad (4.20)$$

Try $\Phi(r, \phi, z) = R(r)Z(z)Q(\phi)$. Separating the Laplace equation in cylindrical coordinates, we find three differential equations which must be satisfied.

$$\frac{\partial^2 Z}{\partial z^2} - k^2 Z = 0 \quad (4.21)$$

has solution

$$Z = A \sin(kz) + B \cos(kz) \quad (4.22)$$

The solution must satisfy boundary conditions that $\Phi = 0$ at $z = 0, L$. Therefore, B must vanish. Hence,

$$Z = A \sin(kz), \text{ where } k = \frac{n\pi}{L}, m \in \mathbb{Z}^+ \quad (4.23)$$

Similarly, we have for Q

$$\frac{\partial^2 Q}{\partial \phi^2} - m^2 Q = 0 \quad (4.24)$$

which has solution

$$Q = C \sin(m\phi) + D \cos(m\phi), \text{ where } m \in \mathbb{Z}^+ \quad (4.25)$$

The radial part must satisfy

$$\frac{\partial^2 R}{\partial x^2} + \frac{1}{x} \frac{\partial R}{\partial x} - \left(1 + \frac{m^2}{x^2}\right) R = 0, \text{ where } x = kr \quad (4.26)$$

The solutions are the modified Bessel Functions:

$$R(x) = EI_m(x) + FK_m(x), \text{ where } m \in \mathbb{Z}^+ \quad (4.27)$$

I_m and K_m are related to other Bessel and Neumann functions via

$$I_m(kr) = i^{-m} J_m(ikr), \text{ where } m \in \mathbb{Z}^+ \quad (4.28)$$

and

$$K_m(kr) = \frac{\pi}{2} i^{m+1} H_m^{(1)}(ikr) \quad (4.29)$$

The potential is finite at $r = 0$, so

$$H_m^{(1)}(0) = J_m(0) + iN_m(0) = 0 \quad (4.30)$$

But $K_m \neq 0$, so $F = 0$. We can now write Φ in a general form:

$$\Phi(r, \phi, z) = R(r)Z(z)Q(\phi) = \sum A \sin\left(\frac{n\pi}{L}z\right) (C \sin(m\phi) + D \cos(m\phi)) EI_m\left(\frac{n\pi}{L}r\right) \quad (4.31)$$

Let A and E be absorbed into C and D .

$$\Phi(r, \phi, z) = \sum_{m=0}^{\infty} \sum_{n=0}^{\infty} \sin\left(\frac{n\pi}{L}z\right) I_m\left(\frac{n\pi}{L}r\right) (C_{mn} \sin(m\phi) + D_{mn} \cos(m\phi)) \quad (4.32)$$

The coefficients C_{mn} and D_{mn} are to be determined by the boundary conditions at $r = a$:

$$V(\phi, z) = \sum_{m=0}^{\infty} \sum_{n=0}^{\infty} \sin\left(\frac{n\pi}{L}z\right) I_m\left(\frac{n\pi}{L}a\right) (C_{mn} \sin(m\phi) + D_{mn} \cos(m\phi)) \quad (4.33)$$

This is a double Fourier transform of $V(\phi, z)$. Multiplying both sides by $\sin(m'\phi)$ and integrating over ϕ yields

$$\begin{aligned} \int_0^{2\pi} V(\phi, z) \sin(m'\phi) d\phi &= \sum_{n=0}^{\infty} \sin\left(\frac{n\pi}{L}z\right) I_m\left(\frac{n\pi}{L}a\right) \{C_{mn} \cdot \pi \delta_{m'm} + 0\} \\ &= \pi \sum_{n=0}^{\infty} C_{m'n} \sin\left(\frac{n\pi}{L}z\right) I_{m'}\left(\frac{n\pi}{L}a\right) \end{aligned} \quad (4.34)$$

where we have used

$$\int_0^{2\pi} \sin(m\phi) \sin(m'\phi) d\phi = \pi \delta_{m'm} \quad \text{and} \quad \int_0^{2\pi} \cos(m\phi) \sin(m'\phi) d\phi = 0 \quad (4.35)$$

Multiplying both sides by $\sin\left(\frac{n'\pi}{L}z\right)$ and integrating over z yields

$$\begin{aligned} \int_0^L \sin\left(\frac{n'\pi}{L}z\right) \int_0^{2\pi} V(\phi, z) \sin(m'\phi) d\phi dz &= C_{mn} I_m\left(\frac{n\pi}{L}a\right) \int_0^L \sin\left(\frac{n'\pi}{L}z\right) \sin\left(\frac{n\pi}{L}z\right) dz \\ &= C_{mn} I_m\left(\frac{n\pi}{L}a\right) \pi \frac{L}{2} \delta_{n'n} \\ \int_0^L \sin\left(\frac{n\pi}{L}z\right) \int_0^{2\pi} V(\phi, z) \sin(m'\phi) d\phi dz &= \pi \frac{L}{2} C_{mn} I_m\left(\frac{n\pi}{L}a\right) \end{aligned} \quad (4.36)$$

Now, the left-hand side of equation 4.36 becomes

$$\begin{aligned} \int_0^L \sin\left(\frac{n\pi}{L}z\right) \int_0^{2\pi} V(\phi, z) \sin(m'\phi) d\phi dz &= \int_0^L \sin\left(\frac{n\pi}{L}z\right) dz \\ &\quad \times \left\{ \int_{-\frac{\pi}{2}}^{\frac{\pi}{2}} (+V) \sin(m'\phi) d\phi \right. \\ &\quad \left. + \int_{\frac{\pi}{2}}^{\frac{3\pi}{2}} (-V) \sin(m'\phi) d\phi \right\} \\ &= \frac{L}{n\pi} \{1 - (-1)^n\} \cdot 0 \end{aligned} \quad (4.37)$$

Upon putting this result back into equation 4.36, we see that

$$\boxed{C_{mn} = 0} \quad (4.38)$$

Likewise, we find $D_m n$ by multiplying both sides by $\cos(m'\phi)$ and $\sin\left(\frac{n'\pi}{L}z\right)$ and continuing with the same analysis:

$$\begin{aligned}
\int_0^L \sin\left(\frac{n\pi}{L}z\right) \int_0^{2\pi} V(\phi, z) \cos(m'\phi) d\phi dz &= \pi \frac{L}{2} D_{mn} I_m\left(\frac{n\pi}{L}a\right) \\
&= \int_0^L \sin\left(\frac{n\pi}{L}z\right) dz \\
&\quad \times \left\{ \int_{-\frac{\pi}{2}}^{\frac{\pi}{2}} (+V) \cos(m'\phi) d\phi \right. \\
&\quad \left. + \int_{\frac{\pi}{2}}^{\frac{3\pi}{2}} (-V) \cos(m'\phi) d\phi \right\} \\
&= \frac{L}{n\pi} \{1 - (-1)^n\} \\
&\quad \times \frac{V}{m} \left\{ 3 \sin\left(\frac{m\pi}{2}\right) - \sin\left(\frac{3m\pi}{2}\right) \right\} \quad (4.39)
\end{aligned}$$

Hence,

$$\boxed{D_{mn} = \frac{2}{\pi L I_m(n\pi a/L)} \frac{1}{n\pi} \{1 - (-1)^n\} \times \frac{V}{m} \left\{ 3 \sin\left(\frac{m\pi}{2}\right) - \sin\left(\frac{3m\pi}{2}\right) \right\}} \quad (4.40)$$

The $D_m n$'s are non-vanishing if both m and n are odd numbers. Let $m = 2k + 1$ and $n = 2l + 1$. Then,

$$D_{mn} = \frac{16(-1)^{k+1}V}{(2k+1)(2l+1)\pi^2} \frac{1}{I_{2k+1}[(2l+1)\pi a/L]} \quad (4.41)$$

Therefore, the potential

$$\boxed{\Phi(r, \phi, z) = \sum_{k=0}^{\infty} \sum_{l=0}^{\infty} \frac{16(-1)^{k+1}V}{(2k+1)(2l+1)\pi^2} \frac{I_{2k+1}[(2l+1)\pi r/L]}{I_{2k+1}[(2l+1)\pi a/L]} \sin\left\{\frac{(2l+1)\pi}{L}z\right\} \cos\{(2k+1)\phi\}} \quad (4.42)$$

4.5 Finite Element Approach

The best estimate of the electric field most likely follows a finite element calculation. We used a truncated-cone model for the probe and coating. One side of the probe was set to ground, and the other to a 1 volt potential. The resulting field is shown in 4.1. The simple estimate noted above for the field magnitude is quite good. As expected, the field is largest close to the surface near the minimum separation of the two electrodes. The field

pattern drops more slowly at larger distances. Several orientations of the probe are shown in the figure so that the symmetry of the field pattern can be ascertained. An electric field of magnitude $> 10^7 V/m$ is available over much of the aperture at operating distances (few 10 's of nm) above the surface. There is a minimum in the field magnitude near the center of the aperture, but this is not important since the field is still sufficient there.

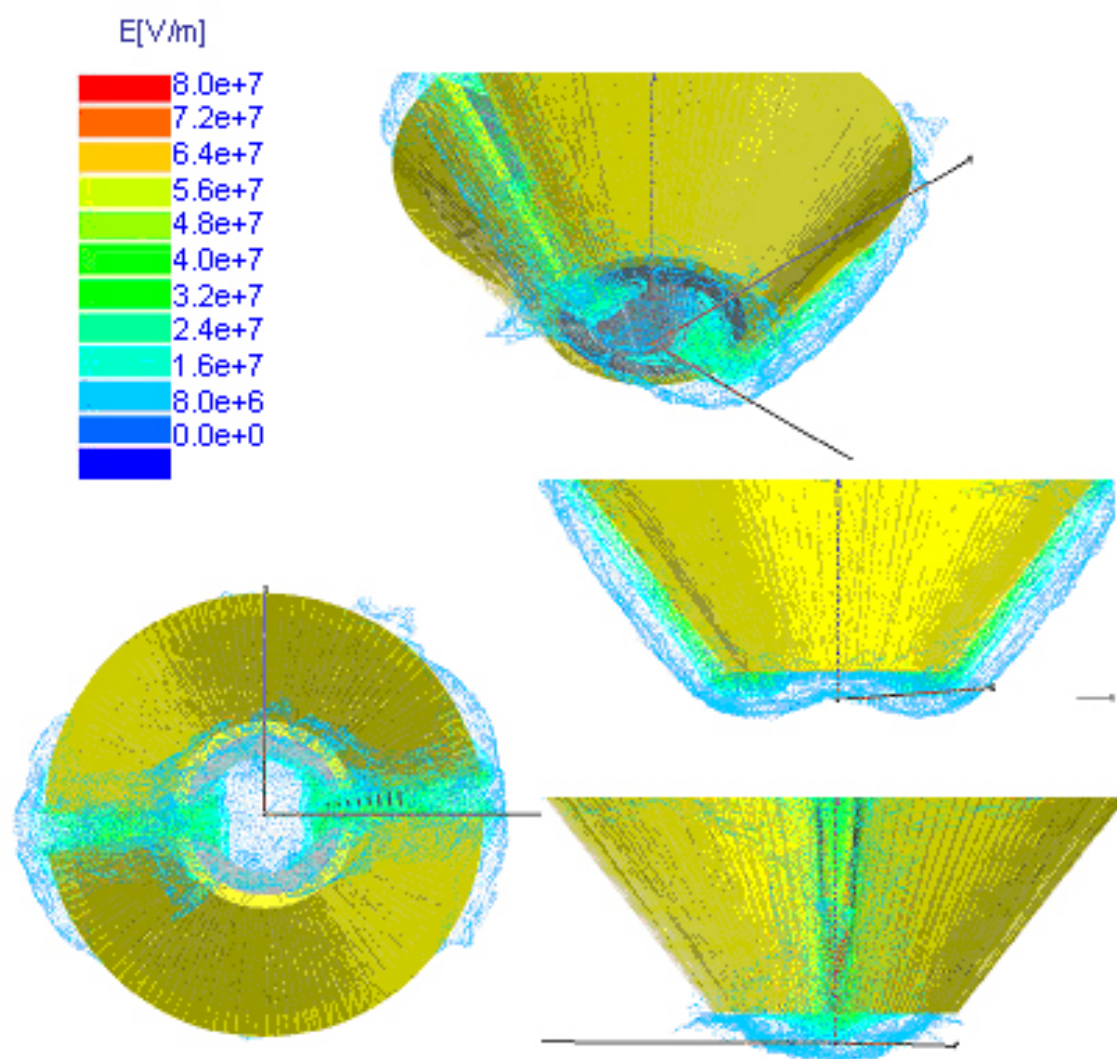


Figure 4.1: The Electric Field of a Split-Tip Probe

Chapter 5

Applications: Molecular Orientation

5.1 Molecular Polarization

A molecule that is polarizable or that has a permanent dipole moment can be oriented in an electric field. This is especially important for the conjugated polymers often used in nonlinear optics or as conductors, since they have a very large polarizability tensor α of order 1 nm^3 or $10^{-13} \text{ C}^2\text{m}^2/\text{J}$. A dipole moment \mathbf{d} is generated by placing the molecule in an electric field \mathbf{E} :

$$\mathbf{d} = \alpha\mathbf{E} \quad (5.1)$$

This dipole moment is along the molecule, which may not be parallel to the field due to the other constraints and the tensor nature of the polarizability. If it is not along the field, then the dipole will experience a torque

$$\boldsymbol{\tau} = \mathbf{d} \times \mathbf{E} \quad (5.2)$$

The torque induces a rotation of the molecule. This will either be balanced by a torque due to its neighbors, or as in our case for which the molecules are free in solution, work against viscous forces to align the molecule with the field. Without viscous forces, the molecule would oscillate about the aligned orientation, but dissipation dominates the motion in solution at these short length scales. For Stokes flow, applicable in the dissipative regime, the evolution of the angle of the dipole θ is given in terms of the angle of the field ϕ and

electric field amplitude E_0 as:

$$I \frac{d^2}{dt^2} = -\alpha \left(\frac{E_0^2}{4} \right) \sin[2(\theta - \phi)] - \gamma \frac{d}{dt} \quad (5.3)$$

with γ the damping constant. [] Since dissipation dominates, we can ignore the left hand side of equation B.3 and solve for $\xi = 2(\theta - \phi)$ in

$$I \frac{d\xi}{dt} = -\alpha \left(\frac{E_0^2}{2\gamma} \right) \sin \xi. \quad (5.4)$$

The $\sin \xi$ term on the right hand side can be replaced by its argument for small ξ (or order of magnitude calculations) to obtain

$$\xi = \xi_0 \exp \left[-\alpha \left(\frac{E_0^2}{2\gamma} \right) t \right] \quad (5.5)$$

for the decay of the relative angle ξ . The time constant can be evaluated from the above , E_0 from the last section, and γ from the relation for a rod of length L and radius a :

$$\gamma = \frac{(\pi\eta L^3)}{3[\ln(L/2a) - 0.66]} \quad (5.6)$$

with η the viscosity of water, 1 centiPoise. The use of a continuum equation for near-atomic sized structures is justified by work on modeling scanning probe tip interactions by Landman's group, and carbon nanotubes by Yakobson. [] For a length L of 10 nm and $a = 1$ nm, the orientation is immeasurably fast, indicating that the time to orient a small molecule with a large polarizability in a very strong local electric field is inconsequential.

5.2 Nano-lithography

The following comparison will concentrate primarily on scanning probe efforts for nanoscale fabrication. Proximal probe lithography has been used for several years. Early work included using an scanning tunneling microscope (STM) as an electron source with e-beam resists [28] or for electron-assisted chemical vapor deposition, [11] single atom manipulation at low temperature [12] or room temperature [3, 45], the creation of gold bumps on a surface with an STM current pulse, [25] and the growth of single layer high gold terraces on the bottom surface of a gold film with hot electrons injected from an STM tip, and their observation with ballistic electron emission microscopy (BEEM). [13, 14, 15, 16] More recent examples of high lateral resolution patterning with proximal probes

includes optical modification of materials with a near-field scanning optical microscope (NSOM), [6, 24] and 'dip-pen' nanolithography with an atomic force microscope (AFM). [34] Although the resolution of many of these probe methods is very high, the interactions with the samples are symmetric, so lateral (in the plane of the sample) orientation cannot be controlled. The proposed project addresses this issue by using a nonsymmetric 'split-probe' to control orientation through a proximal probe interaction while maintaining nanometer-scale resolution. This added dimension of control represents a significant advance.

A problem with proximal probes for large-scale patterning is that they are usually slow. Several approaches were proposed including rapid motion of the substrate – a spinning disk, [26, 27] utilizing many probe microscopes in parallel, [19, 20] and using the microscope only for small, specific regions on the sample as has been done for metrological purposes on an IBM process line. [21] Although these ideas can be made to work, one must still be very concerned about the complexity of the systems and the long-term reliability. Tip wear will always be a problem with scanning probe systems. We therefore believe that the proximal probe should be used where it gives the most advantage - in the developmental and model-building stages. Later, industrial-scale manufacturing stages should be performed with more naturally parallel and robust systems. Our method of oriented deposition should be extendable to a 'smart-mask' system.

Conjugated Polymers are being intensively researched because of their promising optoelectric properties. Poly(*p*-phenylene vinylene) (PPV) is one such conjugated polymer. It is the prototypical conjugated polymer that has been extensively studied over the past 20 years.

The split-tip probe enables the fabrication of highly oriented, nano-scale-patterned materials. The greatest impact will probably be for electronic materials, where the orientation will increase the conductivity and may help to reduce the voltages required for operation of polymeric electronics. There should also be an impact on other materials where an anisotropic optical response is desired, or in biomedical applications. The latter application requires molecular orientation for cellular recognition. These are discussed in more detail below, and serve to define the materials systems that we will investigate.

High Performance Conducting Polymer Films

The conductivity of conducting polymer films is improved by a process called poling, in which a large electric field is applied to the material to partially align the molecules

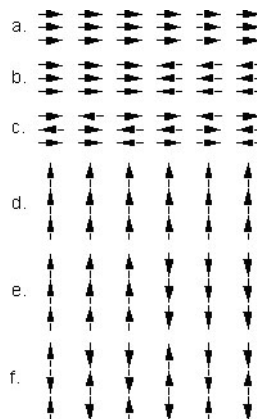


Figure 5.1: The arrows indicate which way the molecules are oriented in several configurations, which will be studied, as described more fully in the text. The current flows from left to right. These are schematic: there will be many more molecules in each direction than shown.

and dramatically increase the conductivity. The higher local fields provided by our probe and poling during growth should result in almost all of the molecules oriented in the same direction while they are defined into wires on the nanometer scale. These are two major impacts in the conducting polymeric materials arena. Figure 5.1 shows example structures that could be fabricated. The material is deposited in the gap between the contacts. The size of the structure that can be made without manual coarse adjustment is limited by the instrument scan range of ~ 25 microns.

Conducting polymers are typically semiconductors with similar bandgaps due to the common π -conjugated bonding found in these polymers. [1] The materials display a broad range of conductivities. The conductivity is strongly dependent on the morphology, [22, 23] which consists of ordered domains separated by disordered regions [1-3] in material prepared by standard practices. Our deposition method should yield wires with nearly perfect orientation, due to the strong poling field we can use during growth. These should show much higher conductivity, which we will measure, and the ability to carry large current densities with a long lifetime.

New Device Opportunities

The ability to orient a conducting polymer molecules virtually 100% in the same direction, which can vary on a nanometer-scale length, allows new possible device configu-

rations that depend upon the orientation of an asymmetric molecule rather than different doping of regions of less-ordered molecules. The field provided by the probe should be sufficient to prevent the depolarization field from previously deposited molecules from affecting the orientation of later molecules. Some example structures are shown in Figure 5.1, where the arrows represent the direction of the permanent dipole moment of the molecules (much enlarged). We can investigate conduction along the molecules, expected to be good, with all molecules aligned, Figure 5.1(a), with an interface, that should act as a potential barrier from an analysis of the electrostatics, Figure 5.1(b), and with both orientations in a film produced by alternating the field direction during the deposition process, Figure 5.1(c). Studies of the properties when molecules are oriented perpendicular to the current flow direction will also be possible, with a similar array of orientation possibilities, Figure 5.1(d-f).

Reduced Driving Voltage

Most conducting polymeric devices such as polymer LED's require a very large driving voltage. This reduces efficiency and inconvenient power supplies. Our technique can impact this area by providing a means to reduce drive voltage, improve the quantum efficiency by reducing defect quenching [24] and increase the capability for high current densities so that electrically pumped polymer laser diodes can be fabricated. [25] The addition of secondary molecules near an electrode [26] to improve efficiency and lifetime [27] is also possible. This could be done by combining the 'dip-pen' lithography with our orienting capabilities. Optimization of the electrode/polymer interface, especially the band offsets, [27, 28] will reduce the drive voltage. The NSOM technique (with the deposition probe) can be used to create light emission maps of the device, to test that the structures are behaving as expected.

Electrical Connection to Tissue

When cells are adjacent in a tissue, they recognize each other by the proteins displayed. A cell constructs a protein tunnel that connects its ion channels to those of its neighbor so that when it signals (changes the ion current pattern), the next cell receives the message. There are many types of ion channels in cells, but only like-types are connected. Thus, one way to optimize specificity in communications between man-made electronics and tissue is to mimic the protein distribution of a particular ion channel of interest, using the orienting capabilities of split-tip probe fabrication, and let the cell build the connectors.

Chapter 6

Conclusion

We have described the design and fabrication of a novel split-tip probe, which can be used to explore the possibility of depositing molecules with specific in-plane orientation that can be controllably varies over 10's of nanometers. We found that the fabrication is significantly more difficult than standard NSOM probes due to the inherent unstable nature of the small metal plates under tension. Theoretical models of the heating during evaporation help to design a method for the fabrication of low stress films required in this unusual deposition geometry. The probes, once fabricated, perform well in topographic and optical microscopy in addition to the unique function enabled by the split tip.

Bibliography

- [1] E. Abbe. Beiträge zur Theories des Mikroskops und der mikroskopischen Wahrnehmung. *Arch. f.Mikr. Anat.*, 9:413–468, 1873.
- [2] S. Akamine, T. R. Albrecht, M. J. Zdeblick, and C. F. Quate. Microfabricated scanning tunneling microscope. *IEEE Elect. Device Lett.*, 10:490, 1989.
- [3] P. Avouris, I.W. Lyo, and Y. Hasegawa. Stm-induced modification and electrical properties of surfaces on the atomic and nanometer scales. In P. Avouris, editor, *Atomic and Nanometer-Scale Modification of Materials: Fundamentals and Applications*, page 11. Kluwer, Dordrecht, 1993.
- [4] E. J. Ayars. *Near-Field Raman Spectroscopy*. PhD thesis, North Carolina State University, Raleigh, Department of Physics, 2000.
- [5] H. A. Bethe. Theory of diffraction by small holes. *Phys. Rev.*, 66:163, 1944.
- [6] K. Birkelund, M. Mllenborn, F. Grey, F. Jensen, and S. Madsen. Combined AFM and laser lithography on hydrogen-passivated amorphous silicon. *Superlattices and Microstructures*, 20:555, 1996.
- [7] C. J. Bouwkamp. On the diffraction of electromagnetic waves by small circular disks and holes. *Phillips Research Report*, 5:401, 1950.
- [8] Robert W. Boyd. *Nonlinear Optics*. Academic Press, San Diego, 1992.
- [9] A.J. Campbell, M.S. Weaver, D.G. Lidzey, D.D.C. Bradley, E. Werner, W. Brtting, and M. Schwoerer. Conduction and trapping in electroluminescent polymer devices. In *Proceedings of Organic Light-Emitting Devices II*, volume 3476, page 98, San Diego, CA, 1998. SPIE.

- [10] Daniel Courjon. *Near-Field Microscopy and Near-Field Optics*. Imperial College Press, London, 2003.
- [11] A.L. deLozanne, E.E. Ehrichs, and W.F. Smith. Four-point resistance measurements of wires written with a scanning tunneling microscope. In P. Avouris, editor, *Atomic and Nanometer-Scale Modification of Materials: Fundamentals and Applications*, page 133. Kluwer, Dordrecht, 1993.
- [12] D. M. Eigler and E. K. Schweizer. Positioning single atoms with a scanning tunneling microscope. *Nature*, 344:524, 1990.
- [13] H. D. Hallen, A. Fernandez, T. Huang, R. A. Buhrman, and J. Silcox. Gold-silicon interface modification studies. *J. Vac. Sci. Technol.*, B9:545, 1991.
- [14] H. D. Hallen, A. Fernandez, T. Huang, R. A. Buhrman, and J. Silcox. Hot electron interactions at the passivated gold-silicon interface. *Phys. Rev. Lett.*, 69:2931, 1992.
- [15] H.D. Hallen. Ballistic electron emission microscopy: from electron transport studies to nanoscale materials science. In C.R.K. Marrian, editor, *Technology of Proximal Probe Lithography*. SPIE Press, Bellingham, 1993.
- [16] H.D. Hallen and R.A. Buhrman. Beem, a probe of nanoscale modifications. In P. Avouris, editor, *Atomic and Nanometer-Scale Modification of Materials: Fundamentals and Applications*. Kluwer, Dordrecht, 1993.
- [17] P. Hoffmann, B. Dutoit, and R. P. Salath. Comparison of mechanically drawn and protection layer chemically etched optical fiber tips. *Ultramicroscopy*, 61:165, 1995.
- [18] S. H. Huerth, M. P. Taylor, H. D. Hallen, and B. H. Moeckly. Electromigration in ybco using a metal clad near-field scanning optical microscope probe. *Appl. Phys. Lett.*, 77:2127, 2000.
- [19] Suzanne Huerth, Michael Taylor, Michael Paesler, and Hans Hallen. Near-field scanning optical microscopy of electromigration in ybco. In *Proceedings of the Second Asia-Pacific Workshop on Near-field Optics*, Beijing, China, 1999.
- [20] Z. Oblakowski J. Joo, J.P. Pouget G. Du, E. J. Oh, J. M. Wiesinger, Y. Min, A.G. MacDiarmid, and A.J. Epstein. Microwave dielectric response of mesoscopic metallic regions and the intrinsic metallic state of polyaniline. *Phys. Rev.*, B49:2977, 1994.

- [21] G. E. Jabbour, S. E. Shaheen, M. M. Morrell, B. Kippelen, N. R. Armstrong, and N. Peyghambarian. Aluminum composite cathodes. *Optics and Photonics News*, page 25, 1999.
- [22] Satoshi Kawata, Motoichi Ohtsu, and Masahiro Irie, editors. *Nano-Optics*. Springer-Verlag, Berlin, 2002.
- [23] H. Liang. *Studies of Near-Field Nonlinear Optical Imaging of Thin Films and Transient Photoconductivity in Conjugated Polymers*. PhD thesis, University of Maryland, College Park, Department of Electrical & Computer Engineering, 2005.
- [24] S. Madsen, M. Mllenborn, K. Birkelund, and F. Grey. Optical near-field lithography on hydrogen-passivated silicon surfaces. *Appl. Phys. Lett.*, 69:544, 1996.
- [25] H. J. Mamin, P. H. Guethner, and D. Rugar. Atomic emission from a gold scanning tunneling microscope tip. *Phys. Rev. Lett.*, 65:2148, 1990.
- [26] H. J. Mamin and D. Rugar. Thermomechanical writing with an atomic force microscope tip. *Appl. Phys. Lett.*, 61:1003, 1992.
- [27] H.J. Mamin, D. Rugar, and R. Erlandsson. Afm data storage using thermomechanical writing. In P. Avouris, editor, *Atomic and Nanometer-Scale Modification of Materials: Fundamentals and Applications*, page 149. Kluwer, Dordrecht, 1993.
- [28] C.R.K. Marrian, E.A. Dobisz, and J.A. Dagata. Low voltage e-beam lithography with the stm. In C.R.K. Marrian, editor, *Technology of Proximal Probe Lithography*, page 58. SPIE Press, Bellingham, 1993.
- [29] N. S. Murthy, G. G. Miller, and R. H. Baughman. Structure of polyacetylene-iodine complexes. *J. Chem. Phys.*, 89:2523, 1988.
- [30] Hari Singh Nalwa and Seizo Miyata, editors. *Nonlinear Optics of Organic Molecules and Polymers*.
- [31] Motoichi Ohtsu and Hirokazu Hori. *Near-Field Nano-Optics*. Kluwer Academic/Plenum Publishers, New York, 1999.
- [32] M. A. Paesler and P. J. Moyer. *Near-Field Optics Theory, Instrumentations, and Applications*. John Wiley & Sons, Inc., New York, 1996.

- [33] I. D. Parker. Carrier tunneling and device characteristics in polymer light-emitting diodes. *J. Appl. Phys.*, 75:1656, 1994.
- [34] R. D. Piner, J. Zhu, F. Xu, S. Hong, and C. A. Mirkin. "Dip-Pen" nanolithography. *Science*, 283:661, 1999.
- [35] Paras Prasad. *Introduction to Nonlinear Optical Effects in Molecules and Polymers*. John Wiley & Sons, Inc., New York, 1991.
- [36] R. Riehn, A. Charas, J. Morgado, and F. Cacialli. Near-field optical lithography of a conjugated polymer. *Applied Physics Letters*, 82:526–528, January 2003.
- [37] J. R. Salem S. Karg, J. C. Scott and M. Angelopoulos. Increasing brightness and lifetime of polymer light emitting diodes with polyaniline anodes. *Synthetic Metals*, 80:111, 1996.
- [38] J. Campbell Scott, George G. Malliaras, J.R. Salem, P.J. Brock, Luisa Bozano, and Sue A. Carter. Injection, transport and recombination in organic light-emitting diodes. In *Proceedings of Organic Light-Emitting Devices II*, volume 3476, page 111, San Diego, CA, 1998. SPIE.
- [39] Zouheir Sekkat and Wolfgang Knoll, editors. *Photoreactive Organic Thin Films*.
- [40] Raoul Stöckle, Christian Fokas, Volker Deckert, Renato Zenobi, Beate Sick, Bert Hecht, and Urs P. Wild. High-quality near-field optical probes by tube etching. *Appl. Phys. Lett.*, 75(2):160–162, 1999.
- [41] E. H. Syngé. A suggested method for extending microscopic resolution into the ultra-microscopic region. *Philos. Mag.*, 6:356, 1928.
- [42] E. H. Syngé. An application of piezoelectricity to microscopy. *Philos. Mag.*, 13:297, 1932.
- [43] N. Tessler, G. J. Denton, and R. H. Friend. Lasing from conjugated-polymer microcavities. *Nature*, 382:695, 1996.
- [44] G. A. Valaskovic, M. Holton, and G. H. Morrison. Parameter control, characterization, and optimization in the fabrication of optical fiber near-field probes. *Appl. Opt.*, 34:1215, 1995.

- [45] L.J. Whitman, J. A. Stroscio, R.A. Dragoset, and R.J. Celotta. Alkali metals on iii-v (100) semiconductor surfaces: Overlayer properties and manipulation via stm. In P. Avouris, editor, *Atomic and Nanometer-Scale Modification of Materials: Fundamentals and Applications*, page 25. Kluwer, Dordrecht, 1993.
- [46] R. L. Williamson and M. J. Miles. Fabrication of probe tips for reflection snom: Chemical etch and heating pulling methods. *J. Vac. Sci. Tech.*, 80:4804, 1996.
- [47] R. L. Williamson and M. J. Miles. Melt-drawn scanning near-field optical microscopy probe profiles. *J. Appl. Phys.*, 80:4804, 1996.
- [48] B. I. Yakobson, P. J. Moyer, and M. A. Paesler. Kinetic limits for sensing tip morphology in near-field scanning optical microscopes. *J. Appl. Phys.*, 73:7984, 1993.
- [49] M. Yan, L. J. Rothberg, F. Papadimitrakopoulos, M. E. Galvin, and T. M. Miller. Defect quenching of conjugated polymer luminescence. *Phys. Rev. Lett.*, 73:744, 1994.
- [50] J. J. Yao, S. C. Arney, and N. C. McDonald. Fabrication of high frequency two-dimensional nanoactuators for scanned probe devices. *J. of Microelectromechanical Systems*, 1:14, 1992.

Appendices

Appendix A

Novel Split-Tip Proximal Probe for Fabrication of Nanometer-Textured, In-Plane Oriented Polymer Films

M. P. Taylor, B. A. Clark III and H. D. Hallen

Physics Department, North Carolina State University, Raleigh, NC 27695-8202

Novel fabrication schemes are required to deposit nanoscale materials that contain molecules oriented in the plane of the surface. Such a symmetry breaking allows devices to be fabricated in this plane, as has proven successful in semiconductor devices. We discuss here the fabrication of a novel split-tip optical nanoprobe that can be used to both orient the molecules with a strong, local electric field, and deposit the molecules with ultraviolet light injected through the probe into the region of aligned molecules. The production of such a split-tip probe is significantly different than that of the related near-field scanning optical microscope (NSOM) probe since the stresses in the metal layer must be held by the metal film - silica interface rather than within the film as it circles the silica. Mounting of the probe to insure reliable electrical contacts is also described.

Keywords: nanoscale deposition, conducting polymers, NSOM, nanoscale characterization

Introduction

Many complex materials and polymer or other molecular-based electronic devices depend upon the orientation of the components for their properties. This requirement places severe constraints on deposition techniques when lateral resolution on the nanometer

length scale is required. We describe the fabrication of a scanning probe that can be used [1] to deposit polymer molecules that are oriented in the plane of the surface. This orientation is complementary to self-assembled monolayers, SAMs, for which the orientation is perpendicular to the surface, and obviates the need for deposition of an electrode on top of the SAM polymer molecules. The latter process is difficult, and often results in damage or destruction of the SAM due to the energy carried by the deposited species [2, 3]. The probe enables new device structures, since it can reverse the orientation of deposited, non-symmetric molecules within nanometers. The result will be a potential barrier at the interface, which can be gated to provide device operation.

We present here the fabrication and electric connection of the central tool to enable this technique - the split-tip probe. The fabrication process is not obvious. We show here that methods developed for fabrication of near-field scanning optical microscope (NSOM) probes do not work well for fabrication of split-tips. The primary reason for failure is film stress and shorting problems. We model and show how these methods can be modified to successfully produce split tips. The electrical connection to the probes is also difficult, due to the combined requirements of multiple connectivity without shorting on a 125 micron diameter fiber, while simultaneously mounting the fiber for successful lateral force microscopy so that the split tip can operate on a scanning proximal probe microscope system.

The split-tip probe, which is mounted onto a standard scanning proximal probe microscope, consists of two electrically isolated and independently contacted metal electrodes deposited on opposite sides of a tapered optical fiber, similar to those used for near-field scanning optical microscopy (NSOM). An electron microscope image of one of these split-tip probes is shown in Fig. A.1. We use Al or Au for these tips. The NSOM system has the required optical hardware for coupling laser light into the region between the split-tip electrodes, which is exactly where it is needed for initiating the deposition to the surface. The probe not only guides the deposition, but can characterize the quality of the resulting material by (1) measurement of topography by the NSOM-like scanning probe, or (2) measuring orientation with polarization-dependent NSOM imaging with the probe that is also used for deposition.

Design Requirements

Before we describe the fabrication of the probe, we briefly describe the deposition

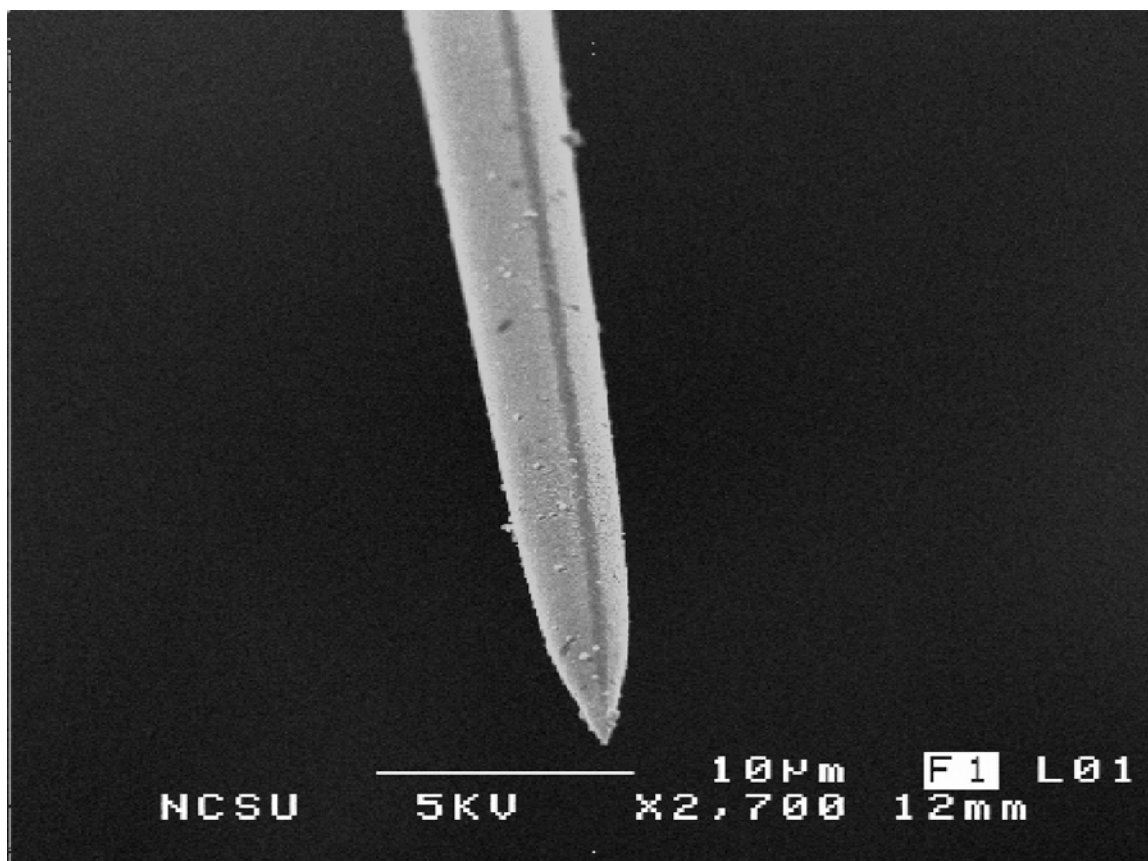


Figure A.1: The split-tip probe

The split-tip probe. The electrodes are on the left and right sides, and the aperture is at the bottom.

scheme that it will be used for and some of the other criteria that impact the design of the probe. A schematic of the probe tip near the sample as molecules are being deposited with a fixed orientation to the sample surface is shown in Fig. B.2. In this cut-away view, the electrodes are on the left and right sides of the tip. The electric field is localized in the region of the split, and is highest where the split is narrow - near the tip apex. Molecules that are in solution will be oriented where the field is high, but not elsewhere. When the tip moves to a new location, it aligns the molecules, then initiates the deposition to the sample with a pulse of ultraviolet light. The tip then moves to a new location, orients the molecules as they should be in the new location, and links them to the surface. It is important that molecules not under the probe tip do not attach to the surface, since they are not oriented.

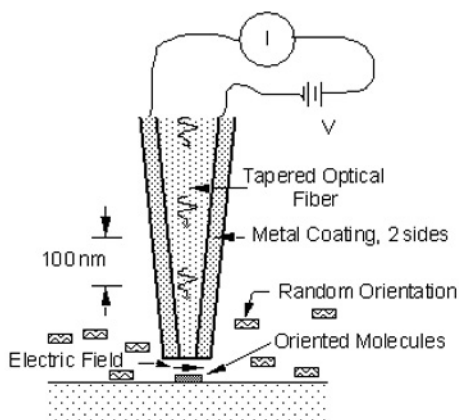


Figure A.2: A schematic of the probe illustrates the major features.

The schemes for insuring this are below. The molecules are shown in solution. This is not necessary. They could also be deposited 'dry' onto the surface, those in the regions of interest be rotated by the field and linked to the surface, then the remainder washed off. Another alternative is to load the tip with molecules as in the 'dip-pen' lithography scheme, [4] oriented and attached as in liquid, then another molecule chosen for a different position. All of these schemes have the same requirements for the probe.

The requirements for the tip are that two electrodes must be electrically isolated from each other, that ultraviolet light must be able to propagate through the probe to the region between the electrodes, that deposition must not occur on the probe itself, that the probe must be compatible with a microscope system, that the probe must not be 'shorted' by the solution or the molecules that are in the solution, that the probe be usable in a probe-surface distance regulation scheme and that the probe have a reasonable lifetime.

Probe Fabrication

Our 'split-tip' probe resembles an NSOM probe, and it is fabricated using a process similar to that used for our NSOM tips, but with a few significant differences that make the process work. We use either a Sutter Instruments puller, modified to work better with fibers, [5, 6, 7, 8] or chemical etching [9] to taper the end of an optical fiber. We need to pull the fibers when we want a large separation of the electrodes, since the fiber gets a flat face

as it cleaves in the fiber pulling apparatus, as can be seen in Fig. A.3. This shape contrasts with the sharp point at the tip of properly-etched fibers. Thus, if the electrodes are to be brought in close proximity to the surface, they need to be close together with etched fibers, but may be further apart when pulled fibers are used. Etched fibers are more reproducible to fabricate in large quantities, and have a higher optical throughput. We initially used only pulled fiber probes for the fabrication of split-tip probes, since we were concerned that the electrodes might short near the tip, but we now use both types without shorting problems.

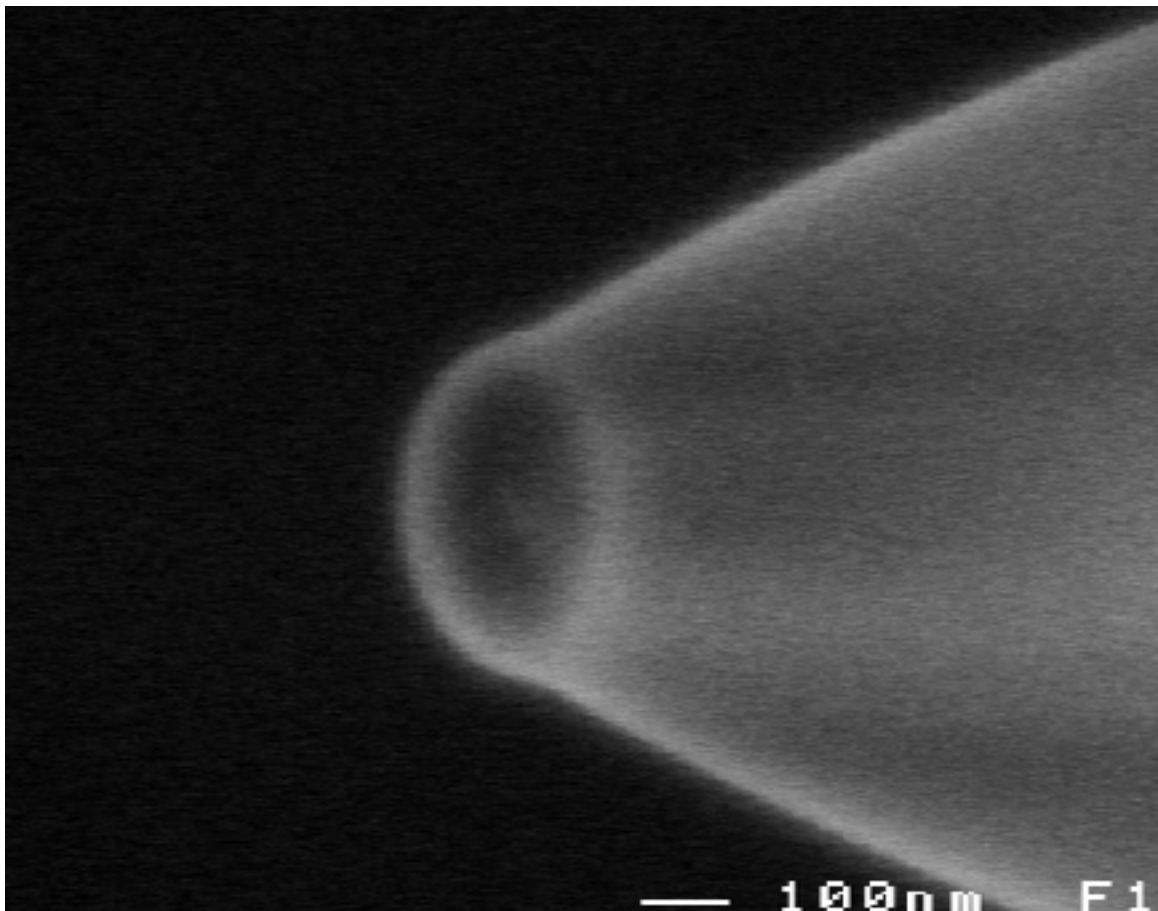


Figure A.3: SEM image of a larger-aperture tapered fiber fabricated by the heat-and-pull method. Note the flat cleaved end that is formed when this fabrication scheme is used, as opposed to the sharp point of etched fibers.

Once the fibers are shaped, metal is coated on one side, then the fiber is rotated 180° , and the other electrode is deposited. This forms a split metal structure with the two metal sides electrically isolated. The metal coating must be thin so that the two sides do

not short together. Our probe-holding fixture, shown in Figure A.4 4, in the deposition chamber allows an accurate flipping of the probes in vacuum. The probes are mounted on holders that keep the probes straight and separated by a sufficient distance that they do not shadow each other during evaporation. Between 8 and 10 probes are held in each unit. Two units can be used at once in the evaporator system, facing each other. The probe holder is mounted on a large gear, and the fiber tails run through a series of holders, also mounted on the gear, in the direction so that they do not unravel during the rotation of the gear. The gear is turned by a smaller gear attached to a small electric motor. We have found that the motors work reliably in vacuum when they are driven by a voltage lower than their maximum rating, which also has the advantage that they spin more slowly. Although it is commonly taught that the back-voltage generated by the motor limits the current and that lower voltages result in motor over-current failure, we have found that the current is limited primarily by the resistance of the wires, when these small motors are under load. We have found that motor failure is usually the result of shorting from metal deposition or an increase in friction in the mechanism, often due to effects of metal deposition. The two gears provide a reduction of the motor rotation by a factor of . Copper braiding attaches the axle of the larger gear shaft to a liquid nitrogen cold trap mounted directly over the rotation units. In this way, the fibers can be cooled by radiation (with approximately π steradians of solid angle towards the cold trap) or by conduction through the Cu braids, shaft, gear, holder, and fiber shanks. The evaporation chamber allows three different source materials can be used during one pump-down. We use Al or Au. Following the initial deposition, a thicker coating of gold is applied to the contact regions on the shank of the tip. A small shutter, driven by an in-vacuum electric motor is used to shield just the probe tips from the evaporation source, so that the shanks are coated with metal.

A significant challenge in the fabrication process is insuring a well-defined split and a continuous coating of metal down to the aperture of the probe. The reason why this is much more difficult than for NSOM tips is that the metal forms a continuous ring around the diameter of the NSOM probe. If there is stress in the metal layer, the film itself will hold the stress. When the metal is thermally evaporated, the stress is typically tensile [ref]. This means that the metal will try to pull itself apart from the probe. If the metal is continuous, it will pull on itself, and usually remain stable. In the split tip, the metal is not continuous, so the stress must be held by the interface between the film and the underlying silica. Far from the tip, this is possible since the area is large, but as the tip is approached,



Figure A.4: A tip holding fixture used for the coating of split-tip fibers.

the area is reduced and the curvature increased. We see process in the series of SEM micrographs. There appears to be a near perfect split in our split tip at low magnification, Figure (a). At a magnification of $X95$, the split appears well defined, but it is crucial to see this type of behavior at the aperture of the probe, rather than up the shaft. As we approach the probe aperture, we see certain imperfections, such as voids in the coating. At $X2000$ magnification, Figure (b), we see cracking and peeling, which presents a significant problem. Figure (c) shows the probe at $X11,000$ magnification, clearly indicating the we are dealing with a case of tensile stress. The aluminum film on the right side of the split tends to bow in a few spots. We also see from this micrograph that tensile stress will relieve itself by microcracking of the film and the peeling of the cracked surface from the substrate. The stress distribution in this film is anisotropic; there are cracking patterns that depend on the stress distribution.

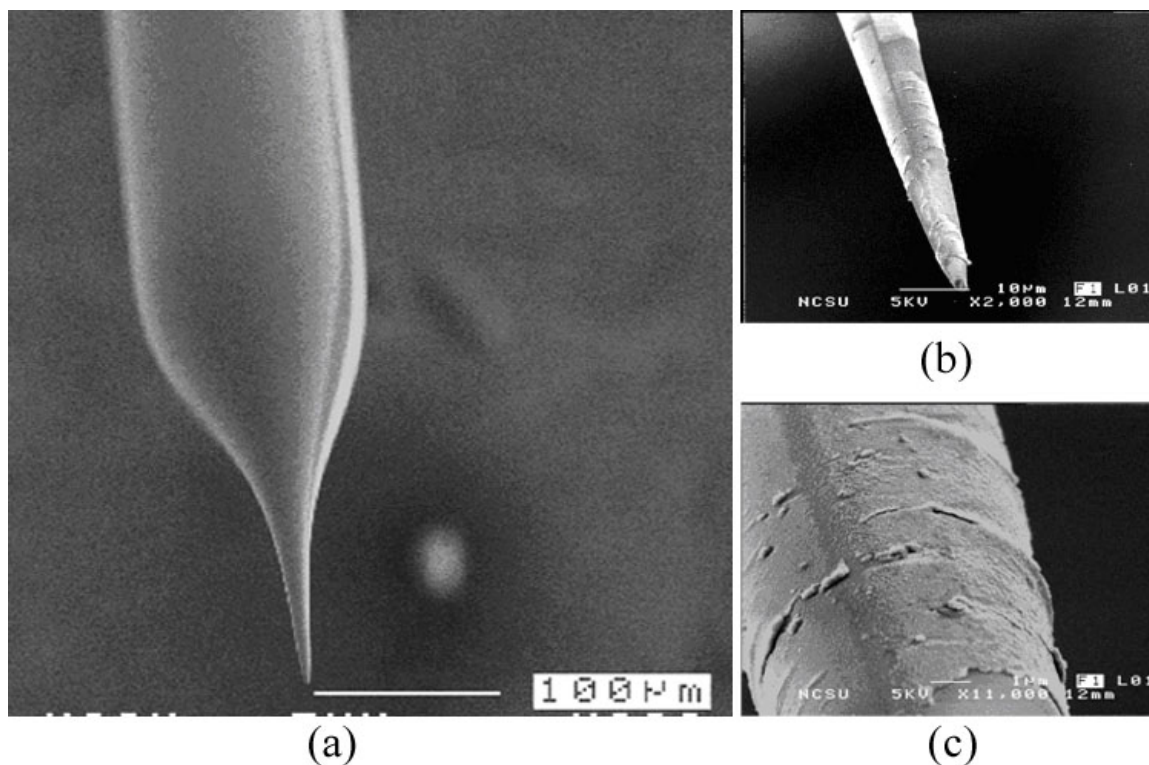


Figure A.5: The split line can be observed slightly to the left of the probe center, from this viewpoint. Peeling of the metal layer is complete near the tip and buckling is evident elsewhere. The end of the tip was broken, presumably as the metal left. (a)-(c) are increasing magnification, at the scale in the image.

The curling near the aperture, along with the observed cracking of the probe coating suggests the coating, a thin film of Al, experiences stress due to the differences in thermal expansion (thermal stress) between the Al and the glass fiber. In general, stress in films results from the differences in thermal expansion (thermal stress) or from the microstructure of the deposited film (intrinsic stress). At substrate temperatures less than 20% of the melting point, intrinsic stress due to incomplete structure ordering dominates. Intrinsic stress results from the microstructure created in the film as atoms are deposited on the substrate. Tensile stress results from micro-voids in the thin film, because of the attractive interaction of the atoms across the voids. Thermal stress occurs because film depositions are usually made above room temperature. Upon cooling from the deposition temperature to room temperature, the difference in the thermal expansion coefficients of the substrate and the film causes thermal stress.

The most common way for measuring film stress is by measuring the deflection (bowing) of a thin film substrate (beam or disc) on which the film has been deposited. This is not possible here, since the substrate is much thicker than the film itself, the substrate is coated on more than one side, and hence, no bowing seems to have occurred. Nevertheless, assuming knowledge of the mechanical properties of the substrate and film, film thickness, and the deflection, we can calculate the film stress. In particular, the film stress, σ_f , for a film of thickness t_f and Young's modulus E_f on a substrate of thickness t_s and Young's modulus E_s curved with a radius ρ and distances from the neutral plane to the point in the film and substrate of Y_f and Y_s respectively, is given by:

$$\sigma_f = \frac{t_f E_s}{5\rho} \left[\left(\frac{t_s^2}{t_f} \right) + 6 \left(\frac{E_f}{E_s} \right) \left(\frac{Y_f}{t_f} \right) \right], \text{ where } -\frac{1}{2} \leq \frac{Y_f}{t_f} \leq \frac{1}{2} \quad (\text{A.1})$$

The substrate stress σ_s is likewise given by:

$$\sigma_s = \frac{t_s E_s}{6\rho} \left[1 + 6 \left(\frac{Y_s}{t_s} \right) \right], \text{ where } -\frac{1}{2} \leq \frac{Y_s}{t_s} \leq \frac{1}{2} \quad (\text{A.2})$$

Large film stresses often result in adhesion failure (de-adhesion), especially when the film has a high modulus or the thickness is large. Hence, we have identified two major contributors to our tensile stress problem:

1. Difference in heating and cooling rates of the substrate and film upon deposition; i.e., the difference in thermal expansion.
2. Film thickness regulation; i.e., the rate of film deposition.

The small size of the probe tip represents a particular problem, since its thermal mass is small - comparable to the thermal mass of the deposited film. This means that the tip end will heat significantly during the film growth process, from both radiative effects and energy carried by the metal evaporant, unless special care is take to prevent it. Tip heating means that significant thermal stress will result when the tip plus film cool to room temperature.

We can estimate the temperature rise in the probe with a simple calculation. The first process that can heat the probe is energy deposited by the metal evaporant, which is given by the evaporation rate onto a flat, untilted surface R ($1nm/s$) where the tip is, an angle correction $\cos(\theta + \psi)$ for the tip with half-angle ψ (6°) tilted up at angle θ (45°), the heat capacity c ($400J/kg/K$ for Al), density ρ ($2700kg/m^3$), temperature change T ($800K$

above ambient estimated by evaporant color), and area of the film A (at distance z from the tip):

$$\text{Energy input} = R\rho c\Delta T A \cos(\theta + \psi) \quad (\text{A.3})$$

with

$$A = 2\pi z \frac{dz}{\cos \psi \tan \psi} \quad (\text{A.4})$$

The second process that can heat the tip is radiation from the thermal evaporation source. Radiative heating power is given by

$$P = \rho A \varepsilon (T^4 - T_o^4) (SA) \quad (\text{A.5})$$

which is also proportional to the area. The emissivity ε is approximately 0.06 for shiny aluminum and 0.8 for the glass fiber. The transition will take place in the first few nm of deposition. We calculate for a temperature of $930K$, a solid angle of $SA \sim 10^{-5}$, that the contribution from radiative heating into the same area as for evaporation is about an order of magnitude smaller. Both have the same area-factor, so will enter the equations similarly. Cooling is primarily by conduction up the fiber taper, as determined by:

$$\nabla^2 T - \frac{\rho c}{\kappa} \frac{dT}{dt} = \frac{Q}{\kappa} \quad (\text{A.6})$$

where κ ($1.5W/m/K$) is the thermal conductivity of quartz, ρ the density, c the heat capacity, and Q the thermal energy per volume. In steady state, the time derivative vanishes. Since the taper is a cone to a good approximation, and since symmetry and lack of significant radiation (and no convection) implies we can convert the thermal problem to one of spherical symmetry, with the energy input per volume given by that in equation (1) scaled by the inverse of the fraction of solid angle taken by one tapered fiber: $2/(1 - \cos \psi)$. This assumes that the energy is uniformly input, rather than at the sides of the taper, but is justified by the relatively shorter lateral thermal times. The energy input in (1) is divided by the volume of a shell at a radius z to get

$$\frac{Q}{\kappa} = \frac{R\rho c\Delta T \cos(\theta + \psi)}{\kappa(1 - \cos \psi) \cos \psi \tan \psi} \frac{1}{z} = D \frac{1}{z} = 633 K/m \frac{1}{z} \quad (\text{A.7})$$

Equation (2) in spherical coordinates becomes, for steady state and uniform in angle,

$$\frac{1}{z^2} \frac{\partial}{\partial z} \left(z^2 \frac{\partial T}{\partial z} \right) = \frac{Q}{\kappa} \quad (\text{A.8})$$

This is solved by a function of the form $T = A/z + B + Cz$. We set the derivative equal to zero at the end of the taper L ($0.5mm$) to indicate the reduction in heat flow at the end of the cone, and set the temperature at the end of the taper to ambient, T_o . This implies

$$T = D \frac{L^2}{2} \left(\frac{1}{z} \right) + T_o - DL + \frac{D}{2} z \quad (\text{A.9})$$

Near the end of the fiber, the last two terms are small, and at $z = 1 \text{ micron}$, the temperature rise is $\sim 150K$ above T_0 .

When we cool the liquid nitrogen cold trap, we find that the temperature of the fiber holder decreases between 120 and 150K below ambient. Thus, the region near the probe tips during evaporation is at or reasonably close to room temperature during evaporation. This is what is required to minimize thermally induced stress.

We use the following protocol for fabricating the probes:

1. Cooling the tips as described in the paragraphs above, or coating in multiple steps, with a 2-3 minute cooling period between each step.
2. Depositing a very thin aluminum film near the tip, on the order of 10 nm. Thus, tensile stress is reduced by avoiding a large value for t_f . Our substrate-film heating is also minimized, since the deposition duration is short. This also reduces the chance of shorting, discussed below.
3. Apply a thicker coating (100-200 nm) to the contact pads so that they will be reliable under repeated use.

These steps minimize the thermal stress by keeping the tip as close as possible to room temperature during the deposition as is possible, through cooling and reduced thermal input. The stress is less important for the contacts, since they are in the region where the fiber is its full size, with sufficient thermal mass to prevent significant thermal variation.

The result yields well defined 'split' behavior in our probes with no sign of stress conditions previously observed. At greater magnifications (Figure B.1), we are able to observe the detailed features of the aperture to display the consistency and control of both the split and the deposition of the material used (Al). We also observe residual material in the split of the probe, away from the aperture. This threatens the required isolation of the electrodes that we have deposited on either side of the probe, but is not unexpected. Mathematically, one expects a perfectly-aligned deposition to uniformly ($\cos \theta$) approach

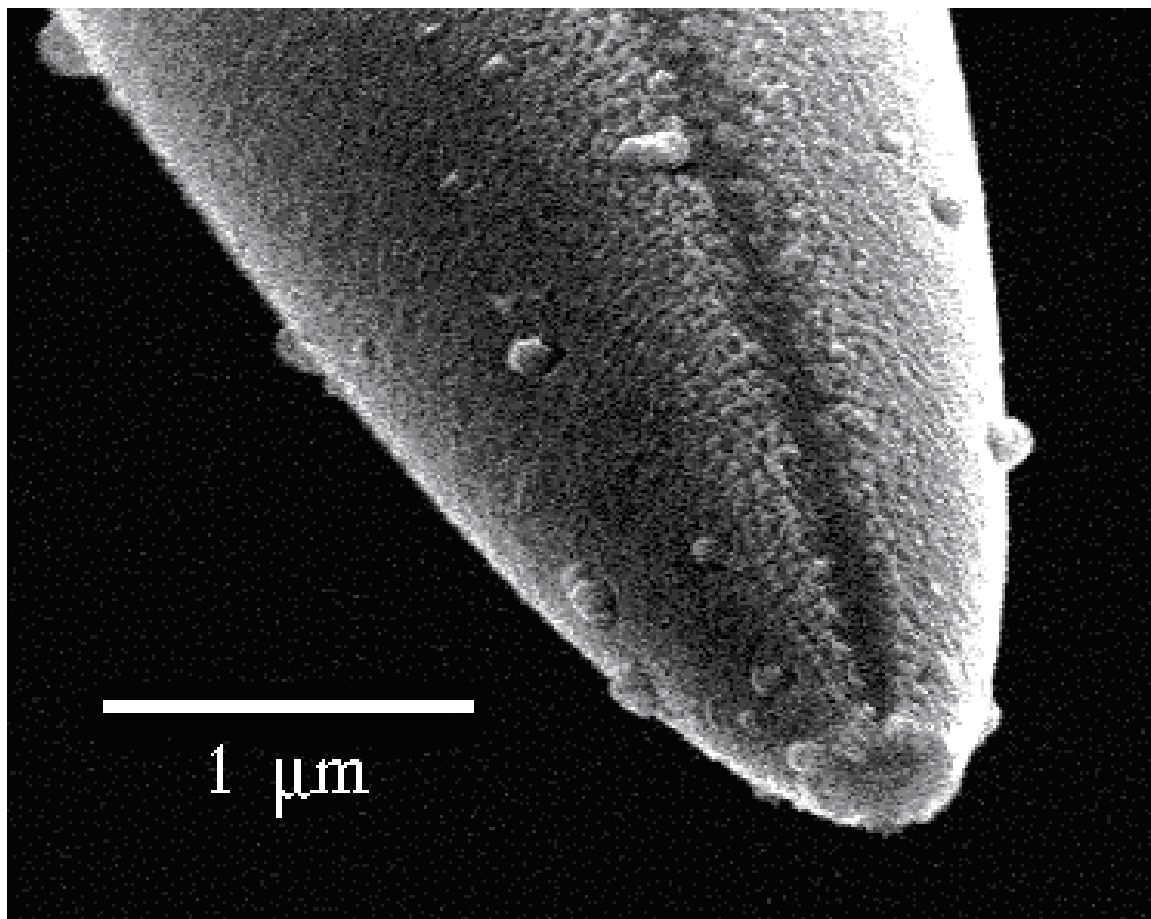


Figure A.6: The tip of a split-tip probe fabricated with the optimal procedure discussed in the text.

zero at the point where the probe surface is perpendicular to the evaporation source. Lack of isolation will result in the two sides shorting together. The effect is most dramatic very near the tip, where the distances involved are short. Figure A.7 provides a detailed view of the split. The split is, in fact, not completely void, but contains small grains of material. The grains are sparse within the split and vary in size from a few nm to tens of nm. The fact that the material is sparse and composed of 'balls' and individual grains (not a relatively smooth coating) is likely due to Ostwald Ripening or coarsening. The metal nucleates as small, dispersed particles initially, but the smaller particles slowly disappear as materials 'evaporates' onto a few that grow relatively large. The smaller particles act as "nutrients" for the larger particles. As the larger particles grow, the area around them is depleted of

metal. This is a spontaneous, diffusion process that occurs because large particles are more energetically favored than smaller ones.

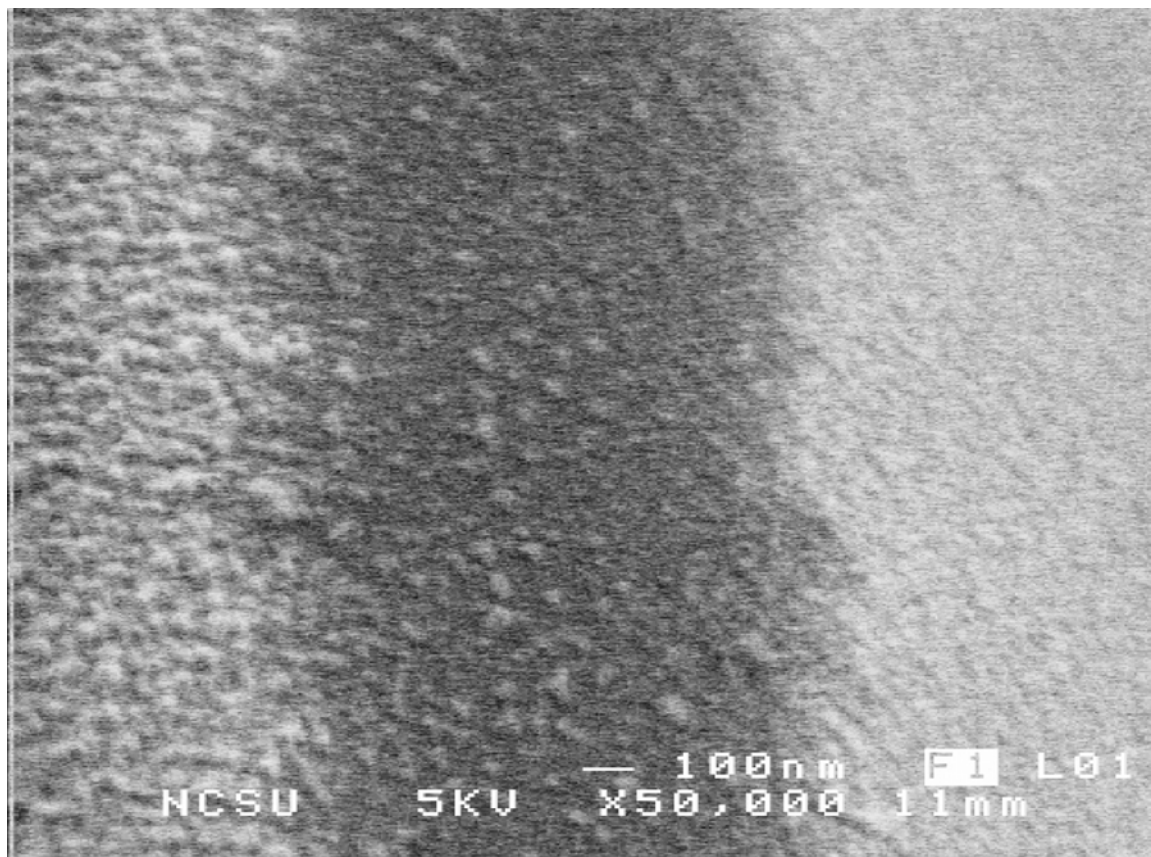


Figure A.7: This X 50000 magnification view, reveals the fact that the split is not completely void of material.

Another factor that improves the electrical isolation is oxidation. Very thin metal within the split will be completely oxidized (if we use Al). This can be enhanced by exposing the probes to a few hundred *mTorr* of pure oxygen for 1/2 hour [10] as a preliminary to venting the system. We follow this process with Al probes.

Probe Mounting

The split-tip probe needs independent electrical contact to the two sides. Due to the concerns noted above, we need to be able to verify contact and lack of shorting between the two sides. Further, the probe must be compatible with mounting into a scanning

proximal probe microscope. The latter entails mounting the probe tip onto the side of a quartz tuning fork (a few mm in length, with 32768 Hz free resonance) that is mounted to the microscope. To prevent shear from removing the metal layer near the contacts, the fiber must be held securely in place, without translation or rotation. Our system allows for these constraints by rigidly holding the fiber in a V-groove/clamp with 2 gold wires pressed against each side. This is shown in figure 9. This part can be translated and rotated to bring the fiber probe it is holding up against the tuning fork. Both are mounted to a glass plate that fits onto the scanning proximal probe microscope, so the operation can be performed conveniently away from the microscope under a dissection microscope. Once the probe is against the tuning fork, glue is applied to the joint and the adjustments left fixed. We have found that the clamping of the fiber as shown in figure 9 does not impact the lateral force microscopy as used in NSOM [11]. We have not observed any significant differences in the resonance behavior of the split tips compared to uncoated or uniformly-coated NSOM probes either.

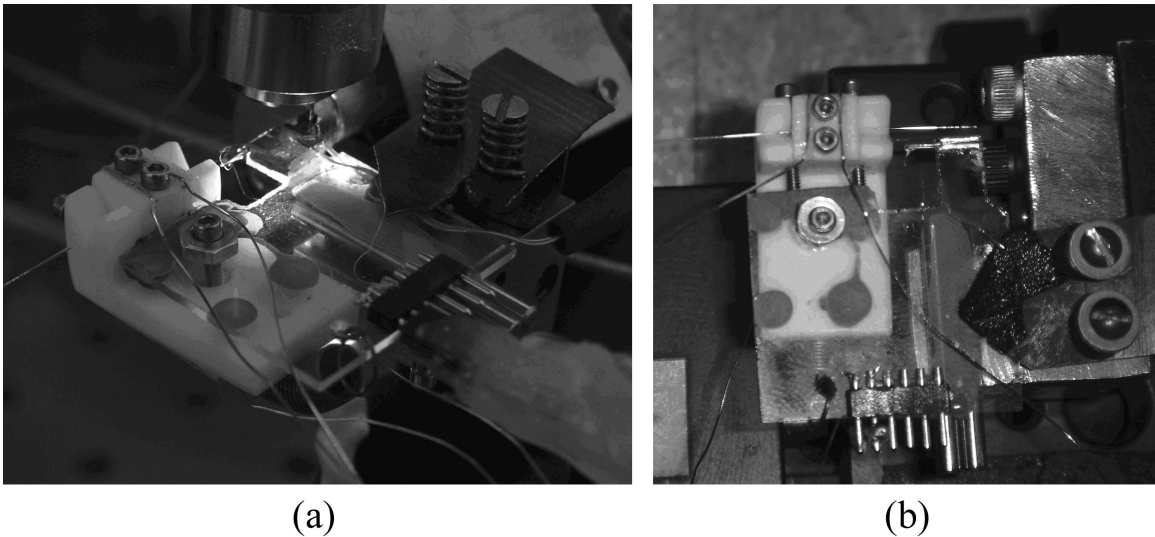


Figure A.8: A photograph of the tip holder - a piece of glass shaped to hold the tip on a tuning fork (upper right portion), the Teflon holder on the upper left keeps the gold wires positioned for contact with the fiber. The fiber can be seen passing through the groove in the Teflon where it contacts the wires, and on to the tuning fork (partially hidden).

The operating sequence once the probe is mounted is to check that contact is established on each side by measuring the resistance between the wires on the same side of

the probe with a multimeter. When both sides have contact, the resistance between the two sides is measured, and should be too large for the meter to register. Possible causes of a lower resistance include a twisting of the probe so that the split is shorted and a probe shorted during the deposition of the metal. This typically happens when there is an etching defect that leaves a mound or hollow on the taper near the tip. The geometry of the mound is such that metal can coat across the split on the edge of the mound. We have found that it is also possible to measure the resistance from one wire on the holder to the fiber coating itself, by using a thin (0.002 inch diameter) gold wire to make the contact to the coating. This contact is not as reliable as a fixed contact, however. Once the electrical characteristics of the probe and connections are verified, a variable voltage is applied to the probe. In cases where leakage current through the solution is possible, the ground lead is replaced by the virtual ground of a high gain current preamplifier, to monitor the magnitude of any shorting current.

Probe Use in a Near-Field Optical Microscope

The split-tip probe can be used to fabricate nanoscale-sized regions of molecules that are aligned in the plane of the surface. A verification of this is to create a large region that can be tested for alignment in a standard optical microscope in polarization mode. A thin film of a water soluble PPV precursor Poly (p-xylene tetrahydrothiophenium chloride), 2.5% in water was diluted 1:4 methanol. Small chips of glass coverslip used as substrates were spin-coated at 500 RPM for 15 s, then at 2000 RPM for 60 s, then at 3500 RPM for 40 s. This differs from the sapphire used in the thickness studies, since the sapphire is also optically anisotropic, confusing the analysis of the film layer. The glass substrates are optically isotropic.

The samples were loaded into a custom NSOM with a split-tip installed, and the system brought into feedback. A region to orient the molecules was chosen from a topographic image created with the split-tip in shear-force height imaging mode, Figure 10(a). A large area of the surface was covered in several 4-micron-square scans, with exposures from a Photon Systems HeAg laser at 224.3 nm wavelength. Exposures varied from an average of 5.8 to 50 pulses per point, where the points were spaced by 40 nm, approximately the optical resolution of the probe. Each pulse was 80 microseconds long and of 3 microJoules of energy. The pulse rate of the laser was 20 Hz. The size of the exposed region is consistent with deposition at all exposure times.

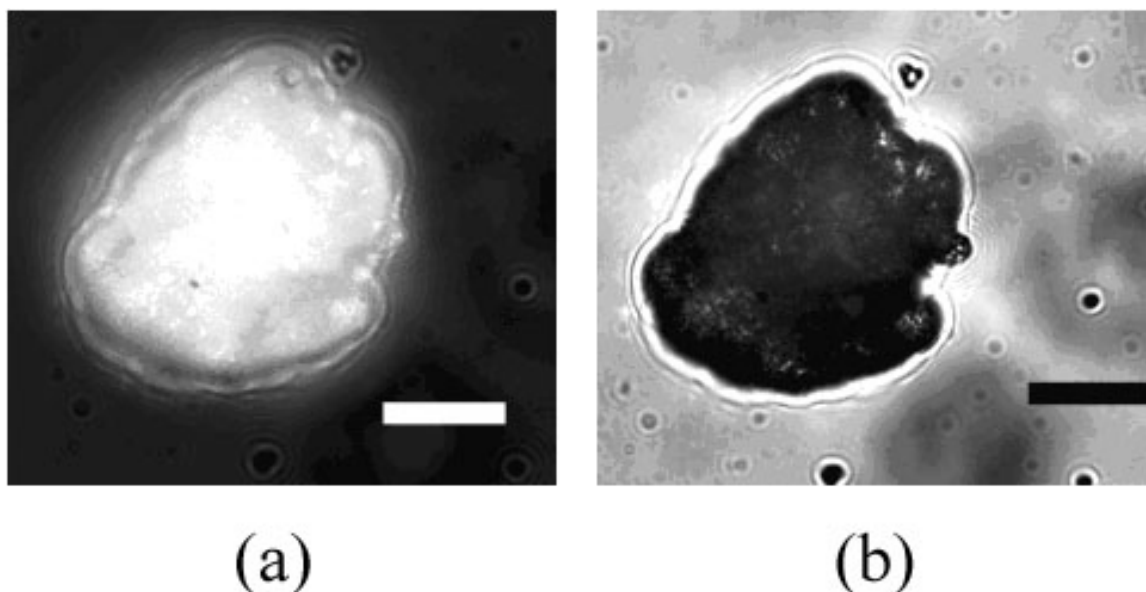


Figure A.9: (a) Topographic image of the spin-coated glass surface 1 micron horizontal and 300 nm vertical, with a 200 nm gray range. The region of molecular deposition is imaged with polarized microscopy. (a) Crossed polarizer configuration. (b) with the analyzer removed. The bars are 20 microns long

After exposure, the sample was removed from the NSOM and developed in pure methanol for 30 s, rinsed in DI water, and blow-dried with dry nitrogen. Optical analysis was performed in a Nikon TE2000-U inverted optical microscope using a 40X, 0.75 NA objective lens. Figure 6 shows optical micrographs of the region of deposited molecules. In the figure, the orientation of the split-tip should result in molecules aligned at about 45 degrees from vertical in the image, perpendicular to the edge of the region. The analyzer was set to pass light polarized vertically with respect to the image. When the incident polarization was set perpendicular to this, Fig. A.9(b), the region without molecules appears dark, as expected for crossed polarizers, but the region with molecules appears bright. This indicates that the molecules have rotated the polarization of the light, which implies that the deposition is at least partially ordered; the molecules have a preferred orientation. When the analyzer is removed, the background is bright. The region of molecules now appears dark. This is due to absorption of light by the molecules. Since undoped PPV is a semiconductor with a bandgap just over 1 eV, it should absorb light in the visible wavelength range. The exposure time in Fig A.9(b) is 8 times that of Fig. A.9(a).

Summary

We have described the design and fabrication of a novel split-tip probe, which can be used to explore the possibility of depositing molecules with specific in-plane orientation that can be controllably varies over 10's of nanometers. We found that the fabrication is significantly more difficult than standard NSOM probes due to the inherent unstable nature of the small metal plates under tension. Theoretical models of the heating during evaporation help to design a method for the fabrication of low stress films required in this unusual deposition geometry. The probes, once fabricated, perform well in topographic and optical microscopy in addition to the unique function enabled by the split tip.

References

- [1] M. P. Taylor and H.D. Hallen, "Fabrication of Nanoscale Polymer Structures with In-Plane Molecular Orientation". Manuscript.
- [2] Z. Zhu, D.L.Allara, N. Winograd, "Chemistry of metal atoms reacting with alkanethiol self-assembled monolayers," *Applied Surface Science*, v 252, n 19, Jul 30, 2006, p 6686-6688.
- [3] Emiel A. Speets, Paul Te Riele, Marc A. F. Van Den Boogaart, Lianne M Doeswijk, Bart Jan Ravoo, Guus Rijnders, Jurgen Brugger, David N.Reinhoudt, Dave H. A. Blank, "Formation of metal nano- And micropatterns on self-assembled monolayers by pulsed laser deposition through nanostencils and electroless deposition," *Advanced Functional Materials*, v 16, n 10, Jul 4, 2006, p 1337-1342.
- [4] R.D. Piner, J. Zhu, F. Xu, S. Hong and C.A. Mirkin, ""Dip-Pen" Nanolithography," *Science* 283, 661 (1999).
- [5] B.I. Yakobson, P.J. Moyer and M.A. Paesler, "Kinetic limits for sensing tip morphology in near-field scanning optical microscopes," *J. Appl. Phys.* 73, 7984 (1993).
- [6] R.L. Williamson and M.J. Miles, "Melt-drawn scanning near-field optical microscopy probe profiles," *J. Appl. Phys* 80, 4804 (1996).
- [7] Mufei Xiao and et al, "Fabrication of Probe Tips for Reflection SNOM: Chemical Etch and Heating Pulling Methods," *J. Vac. Sci. Tech.* B15, 1516 (1997).
- [8] G.A. Valaskovic, M. Holton and G.H. Morrison, "Parameter control, characterization, and optimization in the fabrication of optical fiber near-field probes," *Appl. Opt.* 34, 1215 (1995).
- [9] P. Hoffmann, B. Dutoit and R.-P. Salath, "Comparison of mechanically drawn and protection layer chemically etched optical fiber tips," *Ultramicroscopy* 61, 165 (1995).
- [10] Miller, R. E., W. H. Mallison, A. W. Kleinsasser, K. A. Delin and E. M. Macedo. 1993. Niobium trilayer Josephson tunnel junctions with ultrahigh critical current densities. *Appl. Phys. Lett.* 63, 1423-1425.

- [11] C.L. Jahncke, S. H. Huerth, Beverly Clark and H.D. Hallen, "Dynamics of the tip-sample interaction in near-field scanning optical microscopy and the implications for shear-force as an accurate distance measure," *Applied Physics Letters* 81 (21) 4055-7 (2002).

Appendix B

Fabrication of Nanoscale Polymer Structures with In-Plane Molecular Orientation

M. P. Taylor and H. D. Hallen

Physics Department, North Carolina State University, Raleigh, NC 27695-8202

Molecular electronics will need to be based upon very low defect, highly oriented molecules for performance and long-term reliability, especially under large current conditions. We propose a novel fabrication scheme designed to provide such high quality material with nanoscale lateral resolution, and demonstrate oriented molecular deposition with this scheme. The technique will fabricate nanoscale materials that contain molecules oriented in the plane of the surface. This is perpendicular to the self-assembled monolayer ordered materials, and should provide a more convenient device geometry. The electric and optical field near a novel split-tip probe is calculated, and discuss its use for orienting molecules with μ 100 nm resolution, so that this nanoscale functionality can be obtained. The 'nanopoling' scheme that we propose should be much more effective at orienting molecules than current poling methods due to the larger electric field that can be generated locally, as we demonstrate here.

Keywords: nanoscale deposition, conducting polymers, NSOM, nanoscale characterization

Introduction

Nanoscale materials are now fabricated by a variety of means, but the dominant methods rely on self-assembly or advanced lithography. Self-assembly can create structures in which the molecular orientation perpendicular to the surface is controlled by the

chemistry. This ordering is important for functionality. The problem with self-assembled monolayers (SAMs) is that the orientation perpendicular to the surface is not optimal for device fabrication. The vertical conduction path requires deposition of an electrode on top of the polymer molecules. This process is difficult, and often results in damage or destruction of the SAM due to the energy carried by the deposited species [,]. We discuss here a method of producing molecules lying in the plane of the surface to avoid these problems. The molecules are still highly oriented, enabling good functionality. Defects in the orientation can provide sites susceptible to electron scattering and potential electron-induced atom motion problems [, , ,], especially at high bias or high current density conditions. Thus, defects will impact reliability and lifetime. The degree of orientation also impacts device parameters [, ,], i.e. performance. The technique described here uses nano-poling during deposition to orient the molecules in the surface plane, with a novel split-tip probe. The locally generated orienting fields produce very highly oriented films. We note that when the molecules are asymmetric, a potential barrier will be formed at an interface between region of oppositely oriented molecules. The very high degree of local orientation and the nanoscale resolution of the technique offer the possibility of new devices based solely on the orientation of one asymmetric species of molecules. We present here the electric and optical field modeling of the split-tip probe, and large areas of oriented molecular deposition as a first demonstration of the technique.

The key aspect of the oriented molecular deposition system is a split-tip probe, which is mounted onto a standard scanning proximal probe microscope. The split-tip probe consists of two electrically isolated and independently contacted metal electrodes deposited on opposite sides of a tapered optical fiber, similar to those used for near-field scanning optical microscopy (NSOM). An electron microscope image of one of these split-tip probes is shown in Fig. 1. We use Al or Au coating for these silica tips. The probe is mounted onto an existing NSOM system. The NSOM system has the required optical hardware for coupling laser light into the region between the split-tip electrodes, which is exactly where it is needed for initiating the bonding to the surface.

The split-tip probe offers several advantages for molecular deposition. Nanoscale separation of the electrodes permits a much larger electric field than is possible with larger electrode spacing, due to two fundamental properties: a voltage below an excitation threshold of the material between cannot cause a breakdown, and the likelihood of breakdown is reduced due to less material, hence less fluctuations, in the small volume near the probe.

The field depends (roughly) upon the voltage divided by the spacing, so huge fields are possible below breakdown voltages for small separation, enabling better alignment of the molecules. Further, the small size of the probe permits high-resolution deposition. In this paper we concentrate on the scanning probe approach to attach molecules to a surface with fixed orientation, and in particular modeling the probe for this purpose []. The probe not only guides the deposition, but can characterize the quality of the resulting material by (1) measurement of topography by the near-field scanning optical microscope (NSOM)-like scanning probe, or (2) measuring orientation with polarization-dependent NSOM imaging with the probe that is also used for deposition.

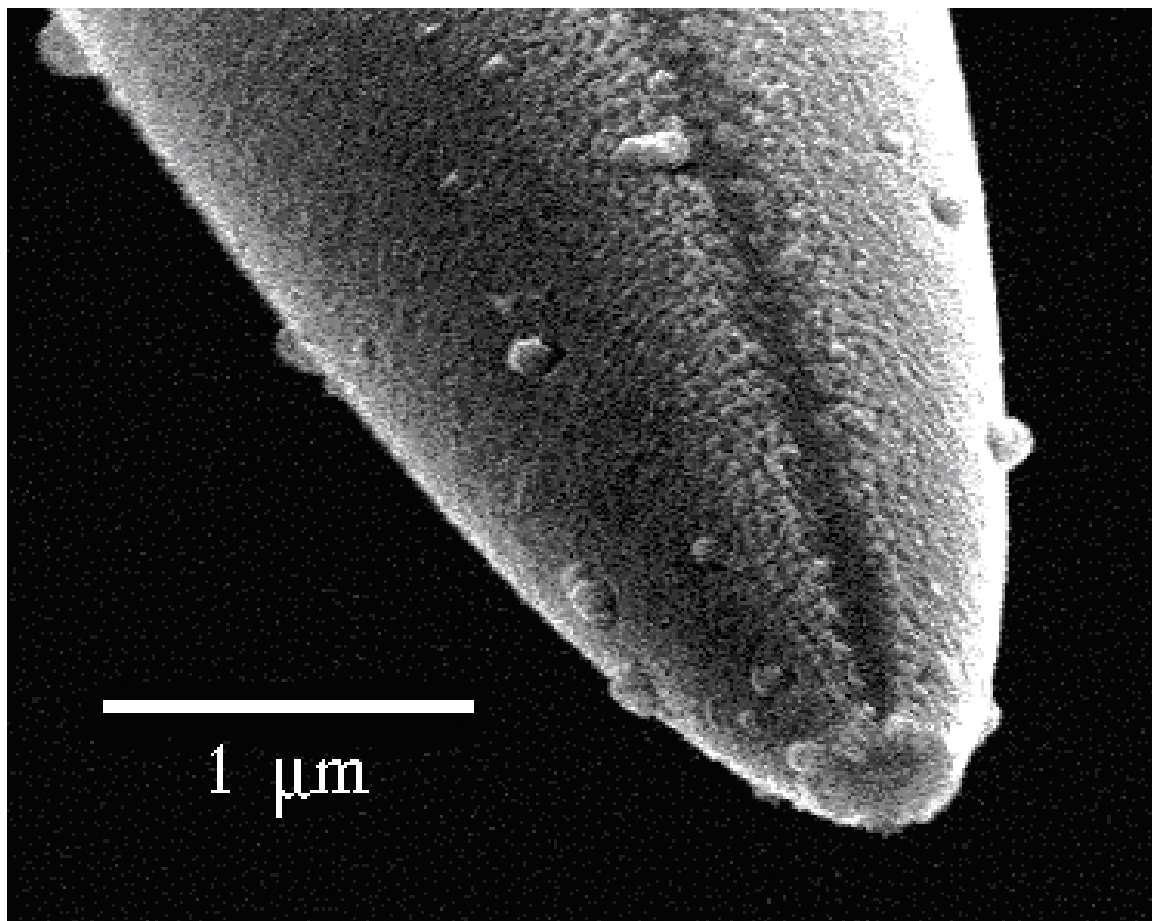


Figure B.1: The split-tip probe. The electrodes are on the left and right sides, and the aperture is visible at the bottom.

The split-tip probe, which is mounted onto a standard scanning proximal probe mi-

roscope, consists of two electrically isolated and independently contacted metal electrodes deposited on opposite sides of a tapered optical fiber, similar to those used for near-field scanning optical microscopy (NSOM). An electron microscope image of one of these split-tip probes is shown in Fig. B.1. We use Al or Au for these tips. The NSOM system has the required optical hardware for coupling laser light into the region between the split-tip electrodes, which is exactly where it is needed for initiating the deposition to the surface. The probe not only guides the deposition, but can characterize the quality of the resulting material by (1) measurement of topography by the NSOM-like scanning probe, or (2) measuring orientation with polarization-dependent NSOM imaging with the probe that is also used for deposition.

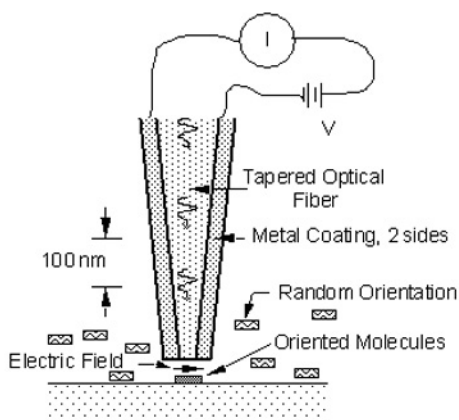


Figure B.2: A schematic of the probe illustrates the major features.

Deposition Scheme

A schematic of the probe tip near the sample as molecules are being deposited with a fixed orientation to the sample surface is shown in Fig. B.2. In this cut-away view, the electrodes are on the left and right sides of the tip. The electric field is localized in the region of the split, and is highest where the split is narrow - near the tip apex. Molecules spin-cast onto a surface, but remain mobile until the solvent evaporates. In this time window, molecules will be oriented where the field is high, but not elsewhere. The tip moves to a location, aligns the molecules, then initiates the deposition to the sample with a UV light

pulse in the region where the molecules are aligned. The tip then moves to a new location, orients the molecules following the same procedure in the new location, and deposits them to the surface. The deposition step could be the UV-initiated leaving group separation from a molecule, rendering the molecule insoluble [,] as demonstrated in this work; a UV-driven catalyst []; or a local excitation induced bonding to the surface []. It is important that molecules not under the probe tip do not attach to the surface, since they are not oriented. We dissolve the molecules that were not exposed to UV light in a 'development' step. The molecules need not be spun cast onto the surface. Another alternative is to load the tip with molecules as in the 'dip-pen' lithography scheme [], oriented and attached as in liquid, then another molecule chosen for a different position. The point to note here is that the design of the probe and its ability to orient molecules is not significantly impacted by the various sources of molecules or the deposition technique used.

The requirements for the tip are that two electrodes must be electrically isolated from each other, that ultraviolet light must be able to propagate through the probe to the region between the electrodes, that deposition must not occur on the probe itself, that the probe must be compatible with a microscope system, that the probe must not be 'shorted' by the solution or the molecules that are in the solution, that the probe be usable in a probe-surface distance regulation scheme and that the probe have a reasonable lifetime.

Comparison to Other proximal Probe Lithography Techniques

The following comparison will concentrate primarily on scanning probe efforts for nanoscale fabrication. Proximal probe lithography has been used for several years. Early work included using an scanning tunneling microscope (STM) as an electron source with e-beam resists [] or for electron-assisted chemical vapor deposition [], single atom manipulation at low temperature [] or room temperature [,], the creation of gold bumps on a surface with an STM current pulse [], and the growth of single layer high gold terraces on the bottom surface of a gold film with hot electrons injected from an STM tip, and their observation with ballistic electron emission microscopy (BEEM) [, , ,]. More recent examples of high lateral resolution patterning with proximal probes includes optical modification of materials with a near-field scanning optical microscope (NSOM) [,], and 'dip-pen' nanolithography with an atomic force microscope (AFM) [16]. Although the resolution of many of these probe methods is very high, the interactions with the samples are symmetric, so lateral (in the plane of the sample) orientation cannot be controlled. The proposed project

addresses this issue by using a nonsymmetric 'split-probe' to control orientation through a proximal probe interaction while maintaining nanometer-scale resolution. This added dimension of control represents a significant advance.

A problem with proximal probes for large-scale patterning is that they are usually slow. Several approaches were proposed including rapid motion of the substrate – a spinning disk [,], utilizing many probe microscopes in parallel [,], and using the microscope only for small, specific regions on the sample as has been done for metrological purposes on an IBM process line []. Although these ideas can be made to work, one must still be very concerned about the complexity of the systems and the long-term reliability. Tip wear will always be a problem with scanning probe systems. We therefore believe that the proximal probe should be used where it gives the most advantage - in the developmental and model-building stages. Later, industrial-scale manufacturing stages should be performed with more naturally parallel and robust systems. Our method of oriented deposition should be extendable to a 'smart-mask' system.

Applications

The split-tip probe enables the fabrication of highly oriented, nano-scale-patterned materials. The greatest impact will probably be for electronic materials, where the orientation will increase the conductivity, reliability and lifetime, and may help to reduce the voltages required for operation of polymeric electronics. Also enabled are nanoscale textured anisotropic optical materials, or tailored biomedical interfaces. The latter application requires molecular orientation for cellular recognition. These are discussed in more detail below, and serve to define the materials systems that we will investigate.

bfseries High Performance Conducting Polymer Films. The conductivity of conducting polymer films is improved by a process called poling, in which a large electric field is applied to the material to partially align the molecules and dramatically increase the conductivity. The higher local fields provided by our probe and poling during growth should result in almost all of the molecules oriented in the same direction while they are defined into wires on the nanometer scale. These are two major impacts in the conducting polymeric materials arena. Figure B.3 shows example structures that could be fabricated. The material is deposited in the gap between the contacts. The size of the structure that can be made without manual coarse adjustment is limited by the instrument scan range of ~ 25 microns.

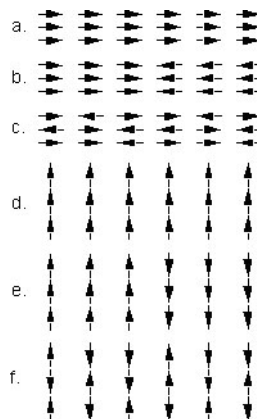


Figure B.3: The arrows indicate which way the molecules are oriented in several configurations, which will be studied, as described more fully in the text. The current flows from left to right. These are schematic: there will be many more molecules in each direction than shown.

Conducting polymers are typically semiconductors with similar bandgaps due to the common π -conjugated bonding found in these polymers. [1] The materials display a broad range of conductivities. The conductivity is strongly dependent on the morphology, [22, 23] which consists of ordered domains separated by disordered regions [1-3] in material prepared by standard practices. Our deposition method should yield wires with nearly perfect orientation, due to the strong poling field we can use during growth. These should show much higher conductivity, which we will measure, and the ability to carry large current densities with a long lifetime.

New Device Opportunities. The ability to orient a conducting polymer molecules virtually 100% in the same direction, which can vary on a nanometer-scale length, allows new possible device configurations that depend upon the orientation of an asymmetric molecule rather than different doping of regions of less-ordered molecules. The field provided by the probe should be sufficient to prevent the depolarization field from previously deposited molecules from affecting the orientation of later molecules. Some example structures are shown in Figure B.3, where the arrows represent the direction of the permanent dipole moment of the molecules (much enlarged). We can investigate conduction along the molecules, expected to be good, with all molecules aligned, Figure B.3(a), with an interface, that should act as a potential barrier from an analysis of the electrostatics, Figure 2(b),

and with both orientations in a film produced by alternating the field direction during the deposition process, Figure B.3(c). Studies of the properties when molecules are oriented perpendicular to the current flow direction will also be possible, with a similar array of orientation possibilities, Figure B.3(d-f).

Reduced Driving Voltage. Most conducting polymeric devices such as polymer LED's require a very large driving voltage. This reduces efficiency and inconvenient power supplies. Our technique can impact this area by providing a means to reduce drive voltage, improve the quantum efficiency by reducing defect quenching [24] and increase the capability for high current densities so that electrically pumped polymer laser diodes can be fabricated. [25] The addition of secondary molecules near an electrode [26] to improve efficiency and lifetime [27] is also possible. This could be done by combining the 'dip-pen' lithography with our orienting capabilities. Optimization of the electrode/polymer interface, especially the band offsets, [27, 28] will reduce the drive voltage. The NSOM technique (with the deposition probe) can be used to create light emission maps of the device, to test that the structures are behaving as expected.

Electrical Connection to Tissue. When cells are adjacent in a tissue, they recognize each other by the proteins displayed. A cell constructs a protein tunnel that connects its ion channels to those of its neighbor so that when it signals (changes the ion current pattern), the next cell receives the message. There are many types of ion channels in cells, but only like-types are connected. Thus, one way to optimize specificity in communications between man-made electronics and tissue is to mimic the protein distribution of a particular ion channel of interest, using the orienting capabilities of split-tip probe fabrication, and let the cell build the connectors.

Probe Fabrication

Our 'split-tip' probe resembles an NSOM probe, and it is fabricated using a process similar to that used for our NSOM tips, but with a few significant differences that make the process work. We use either a Sutter Instruments puller, modified to work better with fibers, [5, 6, 7, 8] or chemical etching [9] to taper the end of an optical fiber. We need to pull the fibers when we want a large separation of the electrodes, since the fiber gets a flat face as it cleaves in the fiber pulling apparatus. This shape contrasts with the sharp

point at the tip of properly-etched fibers. Thus, if the electrodes are to be brought in close proximity to the surface, they need to be close together with etched fibers, but may be further apart when pulled fibers are used. Etched fibers are more reproducible to fabricate in large quantities, and have a higher optical throughput. We initially used only pulled fiber probes for the fabrication of split-tip probes, since we were concerned that the electrodes might short near the tip, but we now use both types without shorting problems.

Once the fibers are shaped, metal is coated on one side, then the fiber is rotated 180° , and the other electrode is deposited. This forms a split metal structure with the two metal sides electrically isolated. The metal coating must be thin so that the two sides do not short together. Our probe-holding fixture in the deposition chamber allows an accurate flipping of the probes in vacuum, and three different source materials can be used during one pump-down. We use Al or Au. Following the initial deposition, a thicker coating of gold is applied to the contact regions on the shank of the tip. A close-up view of the split-tip probe can be seen in Fig. B.1. A significant challenge in the fabrication process is insuring a well-defined split and a continuous coating of metal down to the aperture of the probe.

Various tests are needed to insure that the electrodes are not shorted and that the probe is in proper working order. A voltage is applied to one side of the split tip while the other side of the probe is brought to a virtual ground through a high gain current preamplifier. We have two leads on each side of the tip shank to insure that contacts are made. The tip is mounted in an NSOM system with a known orientation of the probe split, and the sample approached. Lateral force feedback [] is used to regulate probe-sample distance. This is the same as that used in NSOM, with a sub-nanometer lateral tip oscillation, sub-nanometer to 10's of nanometer probe-sample distance during regulation, and 10 nm lateral resolution (typically better than 1 nm vertical resolution). A particular region for deposition is located in topographic mode, then the deposition begun.

Molecular Deposition

We have described how molecules can be oriented under the probe in a liquid or a spun-on layer and how the probe can be positioned. Another requirement is attaching the molecules to the sample surface to complete the deposition process. Existing procedures have demonstrated (non-oriented) molecular deposition with several schemes that involve using light from the probe to react the molecules beneath it to render them insoluble, so they remain on the surface. Examples utilize (1) large precursor molecules for PPV

deposition, and (2) a UV curable resin, i.e, a photoinitiator with monomers for photopolymerization such as 1,6-hexanedioldiacrylate (HDDA) monomer with 2% benzoin ethyl ether (BEE) as the initiator. Both have also been grown with near-field probes [12, 14], although not with controlled orientation. The modification to these schemes for oriented deposition is to use a split-tip probe during deposition. In the latter case, the monomers are not large molecules, so orientation would commence as the polymer grows. The remaining precursor or monomers and BEE is removed in a development step after exposure, leaving the oriented nanoscale material. We use films created of the well-known, conducting, light emitting polymer PPV as a great test case, since it will provide a strong optical asymmetry when aligned.

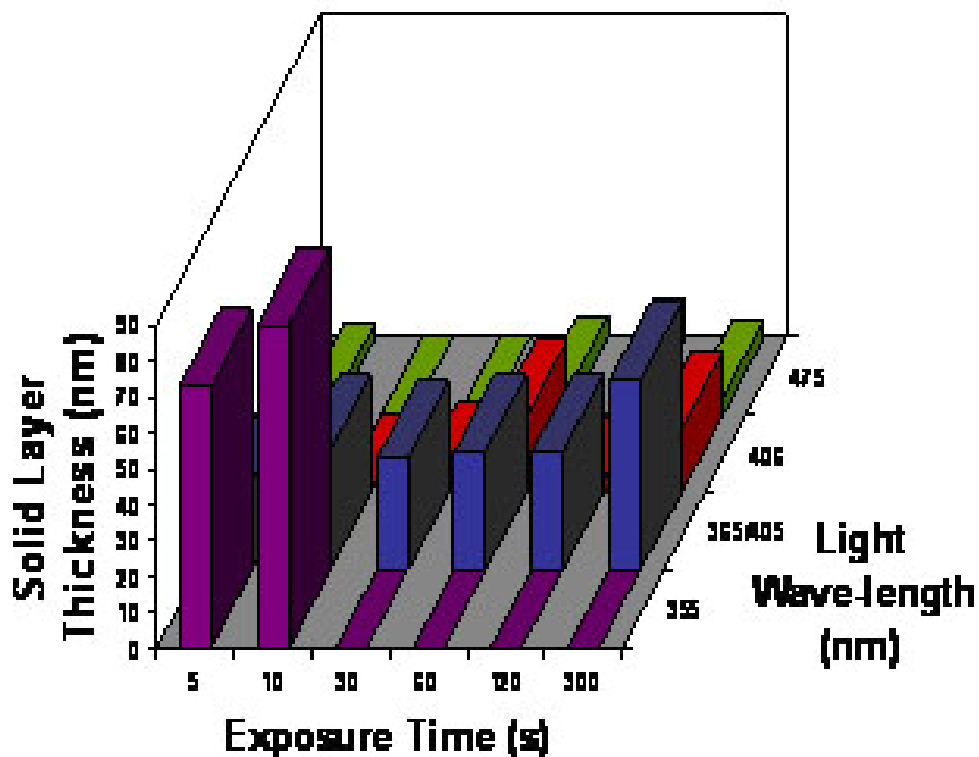


Figure B.4: Layer Solidification Using Various Light Sources

The solid layer thickness left after spin-coating, exposure to the indicated wavelength at the indicated time, and development in methanol.

We have performed an exposure test on a water soluble PPV precursor Poly (p-xylylene tetrahydrothiophenium chloride), 2.5% in water diluted 1:4 methanol, Figure B.4.

Sapphire substrates were spin-coated at 500 RPM for 15 s, then at 2000 RPM for 60 s, then at 3500 RPM for 40 s. This left a layer thickness of the order of 30 nm, as measured by ellipsometry. The samples were then exposed to various light sources to determine the degree to which the polymers became insoluble. Illumination with 355 nm light from a frequency-tripled, pulsed Nd-YAG laser had the highest exposure rate for short exposure times, as measured by the thickness of the solid layer after development for 30 s in methanol, which dissolves the unexposed polymer, and thickness measurement with ellipsometry. The use of sapphire substrates rather than glass was required since the index of the polymer is very close to that of glass, so ellipsometry was not possible for polymer deposition on glass or quartz. At longer exposure times, the pulsed laser ablated the film entirely, and the resulting thickness dropped to zero. Exposure to a filtered mercury arc lamp (365, 405 nm) also gave significant exposure of the PPV precursor, but exposure only at 406 nm with a diode laser was much less effective, and at blue wavelengths, hardly effective at all. The most consistent results are obtained with wavelengths below 400 nm.

Electric Field Near the Tip

The flat end of the probe defines the deposition region between the electrodes. Its size can be from several hundred nanometers down to ~ 10 nm. We can estimate the field strength if we assume a flat capacitor model. For example, a 50 nm tip with 0.5V applied would have a field of order 10^7 V/m. This is a very large electric field, and it is therefore not surprising that we have, on occasion, found that the probe tip is damaged by the high fields. We observe this as an irreversible change in our ability to control the polarization of the light emanating from the probe. It results from damage to the silica. The result illustrates two points: (1) Damage, or breakdown, is possible only when an energy threshold, or voltage threshold if the electrons are emitted from a conductor. A clean system has a very large breakdown system, since lower energy electronic states are not available. Thus, huge electric fields are possible with the nano-split-tip. Even if the minimal voltages are exceeded, breakdown usually doesn't occur until a fluctuation aids the process. A likelihood of a large fluctuation in a nanoscale volume is small, so even larger fields may be possible. (2) We can apply very large fields to the molecules that are being oriented. This is a common occurrence in nanoscale science, when distances get small, and results in new physics as energetic electrons can be injected into materials - potentially causing damage [24, 25, ,]. These fields can allow access to nonlinearities in the electric

field interaction. We will probably not need to use fields this large for orienting molecules, but it is important not to exceed the probe damage thresholds in order not to cause artifacts in the following optical characterization. The high fields may be useful for inducing bonding to the surface, although we do not expect to require them.

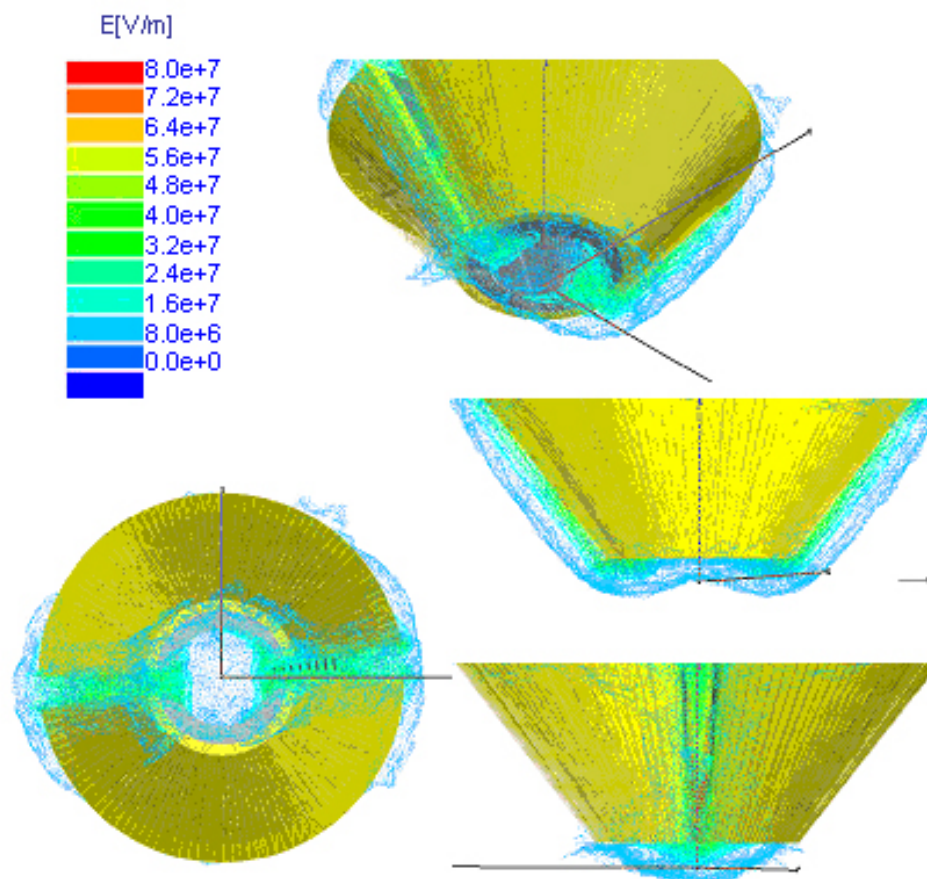


Figure B.5: The Electric Field of a Split-Tip Probe

A better estimate of the electric field follows a finite element calculation. We used a truncated-cone model for the probe and coating. One side of the probe was set to ground, and the other to a 1 volt potential. The resulting field is shown in Fig. B.5. The simple estimate noted above for the field magnitude is quite good. As expected, the field is largest close to the surface near the minimum separation of the two electrodes. The field pattern drops more slowly at larger distances. Several orientations of the probe are shown in the

figure so that the symmetry of the field pattern can be ascertained. An electric field of magnitude $> 10^7$ V/m is available over much of the aperture at operating distances (few 10's of nm) above the surface. There is a minimum in the field magnitude near the center of the aperture, but this is not important since the field is still sufficient there.

Molecular Orientation

A molecule that is polarizable or that has a permanent dipole moment can be oriented in an electric field. This is especially important for the conjugated polymers often used in nonlinear optics or as conductors, since they have a very large polarizability tensor α of order 1 nm^3 or $10^{-13} \text{ C}^2\text{m}^2/\text{J}$. A dipole moment \mathbf{d} is generated by placing the molecule in an electric field \mathbf{E} :

$$\mathbf{d} = \alpha\mathbf{E} \quad (\text{B.1})$$

This dipole moment is along the molecule, which may not be parallel to the field due to the other constraints and the tensor nature of the polarizability. If it is not along the field, then the dipole will experience a torque

$$\boldsymbol{\tau} = \mathbf{d} \times \mathbf{E} \quad (\text{B.2})$$

The torque induces a rotation of the molecule. This will either be balanced by a torque due to its neighbors, or as in our case for which the molecules are free in solution, work against viscous forces to align the molecule with the field. Without viscous forces, the molecule would oscillate about the aligned orientation, but dissipation dominates the motion in solution at these short length scales. For Stokes flow, applicable in the dissipative regime, the evolution of the angle of the dipole θ is given in terms of the angle of the field ϕ and electric field amplitude E_0 as:

$$I \frac{d^2}{dt^2} = -\alpha \left(\frac{E_0^2}{4} \right) \sin[2(\theta - \phi)] - \gamma \frac{d}{dt} \quad (\text{B.3})$$

with γ the damping constant. [] Since dissipation dominates, we can ignore the left hand side of equation B.3 and solve for $\xi = 2(\theta - \phi)$ in

$$I \frac{d\xi}{dt} = -\alpha \left(\frac{E_0^2}{2\gamma} \right) \sin \xi. \quad (\text{B.4})$$

The $\sin\xi$ term on the right hand side can be replaced by its argument for small ξ (or order of magnitude calculations) to obtain

$$\xi = \xi_0 \exp \left[-\alpha \left(\frac{E_0^2}{2\gamma} \right) t \right] \quad (\text{B.5})$$

for the decay of the relative angle ξ . The time constant can be evaluated from the above, E_0 from the last section, and γ from the relation for a rod of length L and radius a :

$$\gamma = \frac{(\pi\eta L^3)}{3[\ln(L/2a) - 0.66]} \quad (\text{B.6})$$

with η the viscosity of water, 1 centiPoise. The use of a continuum equation for near-atomic sized structures is justified by work on modeling scanning probe tip interactions by Landman's group, and carbon nanotubes by Yakobson. [] For a length L of 10 nm and $a = 1$ nm, the orientation is immeasurably fast, indicating that the time to orient a small molecule with a large polarizability in a very strong local electric field is inconsequential.

Optical Characterization

The split-tip probe permits optical characterization of the deposited material. As has been mentioned, the probe must be asymmetric for use in lateral orientation. Our 'split-tip' probe resembles an NSOM probe, except that the metal coating on the outside is split into two parts that are electrically isolated. As such, it can be used as an NSOM tip for optical imaging as a characterization technique. The NSOM topography will also be used as the indicator of material deposition: both where it should and should not be. Polarized light will be used to detect sample anisotropy and hence the quality of orientation. NSOM probes have been used in polarized light studies in the past. The key question is whether the asymmetry of the split-tip precludes such measurements. We have been able to control the state of polarization of light emanating from a split-tip probe from linearly polarized ($> 100 : 1$) in any direction, or circularly polarized. This means that polarized NSOM measurements with a split-tip will be possible. A simple anisotropy analysis system comprised of polarized illumination through the probe with an analyzer in the far-field collection system is envisioned.

Demonstration of Oriented Molecular Deposition

As a first step in the demonstration of the abilities envisioned in this paper, which will take years to fully develop, we show the proof of principle that molecules with a preferred orientation can be deposited with the split-tip. A large area is scanned with the tip during deposition to allow analysis of the material with a standard optical microscope.

A thin film of a water soluble PPV precursor Poly (*p*-xylene tetrahydrothiophenium chloride), 2.5% in water was diluted 1:4 methanol. Small chips of glass coverslip used

as substrates were spin-coated at 500 RPM for 15 s, then at 2000 RPM for 60 s, then at 3500 RPM for 40 s. This differs from the sapphire used in the thickness studies, since the sapphire is also optically anisotropic, confusing the analysis of the film layer. The glass substrates are optically isotropic.

The samples were loaded into a custom NSOM with a split-tip installed, and the system brought into feedback. A large area of the surface was covered in several 4-micron-square scans, with exposures from a Photon Systems HeAg laser at 224.3 nm wavelength. Exposures varied from an average of 5.8 to 50 pulses per point, where the points were spaced by 40 nm, approximately the optical resolution of the probe. Each pulse was 80 microseconds long and of 3 microJoules of energy. The pulse rate of the laser was 20 Hz. The size of the exposed region is consistent with deposition at all exposure times.

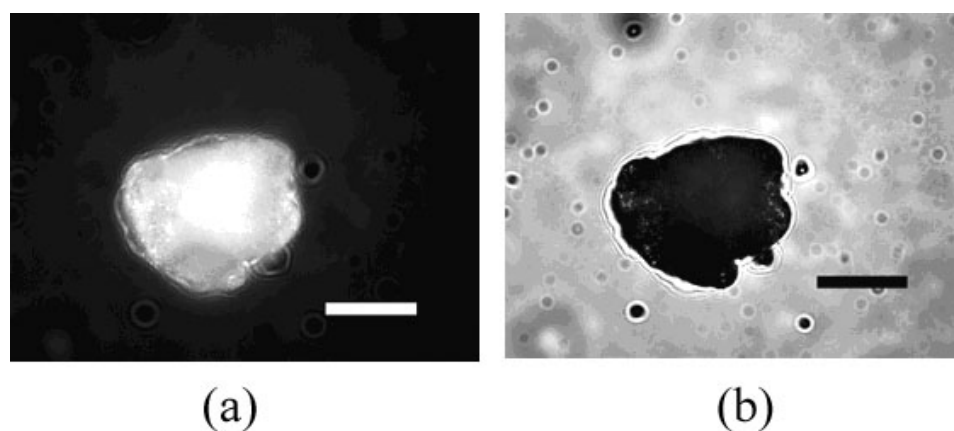


Figure B.6: The region of molecular deposition is imaged with polarized microscopy. (a) Crossed polarizer configuration. (b) with the analyzer removed. The bars are 20 microns long.

After exposure, the sample was removed from the NSOM and developed in pure methanol for 30 s, rinsed in DI water, and blow-dried with dry nitrogen. Optical analysis was performed in a Nikon TE2000-U inverted optical microscope using a 40X, 0.75 NA objective lens. Figure B.6 shows optical micrographs of the region of deposited molecules. In the figure, the orientation of the split-tip should result in molecules aligned a few degrees left of vertical in the image, perpendicular to the edge. The analyzer was set to pass light polarized vertically with respect to the image. When the incident polarization was set perpendicular to this, Fig. B.6 (a), the region without molecules appears dark, as expected

for crossed polarizers, but the region with molecules appears bright. This indicates that the molecules have rotated the polarization of the light, which implies that the deposition is at least partially ordered; the molecules have a preferred orientation. When the analyzer is removed, the background is bright. The region of molecules now appears dark. This is due to absorption of light by the molecules. Since undoped PPV is a semiconductor with a bandgap just over 1 eV, it should absorb light in the visible wavelength range. The exposure time in Fig B.6 (a) is 8 times that of Fig. B.6 (b).

Further information can be gleaned by comparing to data acquired after rotating the sample by 45 degrees, so that the analyzer collects light far from the orientation of the molecular axis. Two effects will be noted since the complex dielectric function will likely be different for light polarized along or perpendicular to the molecular axes. The first is a change in absorption. The second is a change in the polarization state of the transmitted light. The latter can be modeled as absorbing uniaxial optical layer with the optical axis in the plane of the surface, close to the input polarization for the unrotated sample data. For the unrotated case, the polarization remains essentially constant, but the amplitude is decreased, assuming perfect alignment (in practice it is off by a few degrees). For the 45 degree rotated case, the film behaves like a waveplate, so the resultant transmitted polarization is slightly elliptical in addition to an amplitude decrease (primarily for the component along the optic axis).

Table B.1: Normalized transmission data extracted from images similar to B.6

Sample Rotation	Analyzer Position	Transmission in region		Ratio of rotated/unrotated data
		w/ molecules	w/o molecules	
None (few deg)	None	10129 ± 2319	45137 ± 4126	1.54
45°	None	15556 ± 3247	46353 ± 4767	
None (few deg)	90° (\parallel to input)	5057 ± 1586	44032 ± 3631	1.42
45°	90°	7173 ± 1802	42030 ± 3089	
None (few deg)	0° (\perp to input)	6983 ± 283	779 ± 223	1.17
45°	0°	8154 ± 208	782 ± 138	
None (few deg)	25°	6090 ± 1137	6379 ± 1651	1.42
45°	26°	8669 ± 1008	7080 ± 1023	
None (few deg)	-24°	6334 ± 1122	5668 ± 1725	1.37
45°	-24°	8705 ± 989	5887 ± 846	

Table B.1 shows data for several measurements. Averages within and outside of the region with deposited molecules were taken for several polarization conditions. The

data in the tables are arbitrary units after scaling to correct for different image exposure times. The light away from the molecular deposition follows the cosine-squared form expected as the analyzer polarizer is rotated. It does not depend upon the sample rotation. The area with molecules does not follow that functional form, but depends only weakly on the analyzer position. Generally, the transmission is lower when the input polarization aligns with the molecules. This suggests that the molecules absorb more energy along their axis than perpendicular to them. The ratio when no analyzer is in place, 1.54, can be used to calculate the fraction transmitted along the molecule axis, A , compared to the perpendicular polarization, B , to be about $A/B = 0.69$, using $(A^2/2 + B^2/2)/A^2 = 1.54$. Table ?? shows that this ratio drops to 1.42 when an analyzer parallel to the input polarization is inserted. The difference relates to the conversion to elliptic polarization for the 45 degree rotated case, and is consistent with the molecular film acting as a waveplate - as would be expected when the molecules are aligned. Also of note is the reduction of this ratio in the crossed polarization configuration. On one hand, this could be expected since this component of light would not experience significant absorption. On the other hand, the 45 degree rotated configuration would be expected to more efficiently convert the polarization state compared to the few-degree off (what we have been calling aligned) configuration. Perhaps the increase in index due to the proximity to an absorption axis can explain this observation. The final note from Table ?? in the consistency as the analyzer is rotated in the positive and negative directions, in both the ratios and the signal levels.

Summary

We have described a novel split-tip probe, which can be used to explore the possibility of depositing molecules with specific in-plane orientation that can be controllably varies over 10's of nanometers. It is expected that the development of this method will open new venues for the fabrication of complex materials and, in particular, novel polymer electronic materials and devices or biological interfaces.

Acknowledgements

This material is based upon work supported by the National Science Foundation under grant numbers DMR-9975543 and DMII-0210058. This research was also sustained by fellowship support from the U.S. Department of Education Graduate Assistance in Areas of National Need (GAANN) Fellowship Program (P200A000854).

References

- [1] M. P. Taylor and H.D. Hallen, "Fabrication of Nanoscale Polymer Structures with In-Plane Molecular Orientation". Manuscript.
- [2] Z. Zhu, D.L.Allara, N. Winograd, "Chemistry of metal atoms reacting with alkanethiol self-assembled monolayers," *Applied Surface Science*, v 252, n 19, Jul 30, 2006, p 6686-6688.
- [3] Emiel A. Speets, Paul Te Riele, Marc A. F. Van Den Boogaart, Lianne M Doeswijk, Bart Jan Ravoo, Guus Rijnders, Jurgen Brugger, David N.Reinhoudt, Dave H. A. Blank, "Formation of metal nano- And micropatterns on self-assembled monolayers by pulsed laser deposition through nanostencils and electroless deposition," *Advanced Functional Materials*, v 16, n 10, Jul 4, 2006, p 1337-1342.
- [4] R.D. Piner, J. Zhu, F. Xu, S. Hong and C.A. Mirkin, ""Dip-Pen" Nanolithography," *Science* 283, 661 (1999).
- [5] B.I. Yakobson, P.J. Moyer and M.A. Paesler, "Kinetic limits for sensing tip morphology in near-field scanning optical microscopes," *J. Appl. Phys.* 73, 7984 (1993).
- [6] R.L. Williamson and M.J. Miles, "Melt-drawn scanning near-field optical microscopy probe profiles," *J. Appl. Phys* 80, 4804 (1996).
- [7] Mufei Xiao and et al, "Fabrication of Probe Tips for Reflection SNOM: Chemical Etch and Heating Pulling Methods," *J. Vac. Sci. Tech.* B15, 1516 (1997).
- [8] G.A. Valaskovic, M. Holton and G.H. Morrison, "Parameter control, characterization, and optimization in the fabrication of optical fiber near-field probes," *Appl. Opt.* 34, 1215 (1995).
- [9] P. Hoffmann, B. Dutoit and R.-P. Salath, "Comparison of mechanically drawn and protection layer chemically etched optical fiber tips," *Ultramicroscopy* 61, 165 (1995).
- [10] Miller, R. E., W. H. Mallison, A. W. Kleinsasser, K. A. Delin and E. M. Macedo. 1993. Niobium trilayer Josephson tunnel junctions with ultrahigh critical current densities. *Appl. Phys. Lett.* 63, 1423-1425.

- [11] C.L. Jahncke, S. H. Huerth, Beverly Clark and H.D. Hallen, "Dynamics of the tip-sample interaction in near-field scanning optical microscopy and the implications for shear-force as an accurate distance measure," *Applied Physics Letters* 81 (21) 4055-7 (2002).

Appendix C

Electromigration in $\text{YBa}_2\text{Cu}_3\text{O}_{7-\delta}$ using a Metal Clad Near-Field Scanning Optical Microscope Probe

S. H. Huerth*, M. P. Taylor*, H. D. Hallen*, and B. H. Moeckly†

*North Carolina State University, Raleigh, NC 27695

†Conductus, Inc. Sunnyvale, CA 94086

Electromigration or electron-induced-migration (EIM) of oxygen in the high-temperature superconductor $\text{YBa}_2\text{Cu}_3\text{O}_{7-\delta}$ (YBCO) alters the superconducting properties through variations in the oxygen concentration. We study this process with unprecedented spatial resolution and find that the transport of oxygen through a grain boundary into a neighboring grain is unlikely, and that hot electron effects dominate the mechanism for EIM in this system. The extent of the EIM effects implies that grain boundary scattering is strong for these electrons. EIM is induced with the tunnel current from the metal cladding on a near-field optical microscope (NSOM). Variations in the oxygen concentration due to fabrication, aging, and electromigration are imaged optically and corroborated to the grain structure.

Electromigration (EM) of oxygen in $\text{YBa}_2\text{Cu}_3\text{O}_{7-\delta}$ (YBCO) has been reported in several papers [1, 2]. Device quality and lifetime can be limited by it, so understanding and controlling this process is important. The change of the superconducting current-voltage curves after various EM doses was used to show improvement of microbridge critical current at low dose, degradation at high dose, and reversibility of electromigration. It was experimentally determined that a current density of $3 - 5 \text{ MA/cm}^2$ at room temperature improved the critical current while higher current densities caused degradation. EM has

also been used to change the properties of superconducting Josephson junctions, although the behavior is somewhat more complex. Heating the samples in an oxygen atmosphere was found to partially reverse the EM effects [1]. EM of oxygen in YBCO arises in fault protection for electrical power systems. Excess current in a superconducting bar causes it to become normal and heat. EM ensues, resulting in the equivalent of a low insertion loss, high current fuse. EM characterization in commercial superconducting material is needed for reliability and lifetime estimates.

In this paper, we localize the electron-induced-migration (EIM) of oxygen, in samples deposited at Conductus, by using a near-field scanning optical microscope (NSOM). This improved resolution, combined with NSOM topographic images, open a new venue into EIM physics in this system. We find that we can induce EIM with tunnel electrons from the NSOM tip, that hot electrons are important in the EIM mechanism, and that grain boundary scattering is strong for these electrons. The transport of oxygen from one grain to another is found to be small. We select the local area to electromigrate – within a grain or at a grain boundary, for example, from NSOM images. The results of the EIM are imaged with NSOM as changes in the reflectance induced by differences in the oxygen concentration. This adds another capability to NSOM, which has already been used extensively for materials analysis [3], spectroscopy [4,5], and electron-hole recombination time imaging [6].

Several groups have studied the optical properties of YBCO [7,8,9,10]. Kircher *et al* [10] found that the reflectance decreases with increasing oxygen content for the electric field parallel to the a -axis, but the opposite and a stronger dependence for the electric field parallel to the c -axis. Far field measurements of c -axis normal films show an anti-correlation between reflectivity and oxygen content, as has been observed [2]. The situation is not as straightforward in NSOM. Calculations [11,12] of the electric field near an NSOM probe show that the component of electric field perpendicular to the sample is similar in magnitude to that parallel to the sample. The boundary conditions imposed in NSOM for coupling light from the aperture to the detector in the reflection geometry with a conducting sample favor the detection of light polarized perpendicular to the sample. Thus, we expect the stronger dependence of the electric field parallel to the c -axis [10] to dominate. There will be a positive correlation between the reflectivity and oxygen content in NSOM measurements. Our images of aged and electromigrated samples are consistent with these expectations.

The physics of EIM is very complex and has been modeled in various ways [14,15,16,17,18].

EM is usually modeled as a momentum transfer from the moving electrons in the "electron wind" to the atoms in the lattice. It can also be caused by the electrostatic force present in the material (the "direct force"). Measurements of EM of the basal-plane oxygen toward the anode, not the cathode, in YBCO [2] support the latter mechanism in lithographically-defined structures of this material, since the O(1) atoms exist as negatively charged ions. EIM induced by tunnel electrons can also be caused by hot (few eV) electron scattering, elastically or inelastically, from the oxygen atoms. YBCO is an orthorhombic lattice, with the O(1) oxygen moving in the Cu(1) planes.

The sample was imaged using an NSOM in reflection mode, similar to that used previously [20], but the shear force is detected using the tuning fork method [21]. The sample is carbon-taped to the extender tube mounted on the piezoelectric scanner. Ar^+ laser light, 514 nm or 488 nm , is coupled into the fiber and the light reflected from the sample focused by a 0.45 NA lens onto a photodiode. The preamplified signal is filtered to 3 Hz and averaged 5 times. The optical image from the photodiode is collected simultaneously with the topographic image. The probe apertures, resulting from an angled ~ 500 nm Al coating, were characterized with SEM and were less than 100 nm in diameter. An image was obtained for each wavelength before and after each EIM.

EIM was induced with a negative voltage applied to the sample and using the probe as a tunneling electrode. To allow tunneling, the shear force regulation level was reduced, causing the sample to approach the tip. Once the tunnel current reached the desired level, the probe was stopped and, except for feedback dithering, held in this position from 36 minutes to 8 hours to achieve the desired dosage. The voltage applied to the sample in this study was varied from -1 to -3 volts. The laser was shut off during EIM.

The YBCO films were deposited by laser ablation onto $LaAlO_3$ substrates. A 20 nm buffer layer of CeO_2 was first grown in order to suppress a-axis growth. The YBCO films were grown to a thickness of 200 nm , at a substrate temperature of 785 $^{\circ}C$, in a background oxygen pressure of 400 $mTorr$. The laser fluence was $\sim 1J/cm^2$. We have grown many hundreds of YBCO films using this procedure, and the process produces routinely excellent films, as discussed in previous publications. These films typically possess a room-temperature resistivity of $\sim 200-250 \Omega \cdot cm$ which decreases linearly with decreasing temperature and extrapolates to zero at 0 K . Superconducting transition temperatures are typically above 89-91 K with transition widths less than 1 K . Standard 2θ X-ray diffraction analysis of the films in this study indicated the presence of only (001) peaks. Scans of

the (104) χ -angle confirmed that the films were entirely c -axis oriented with no detectable amount of a -axis-oriented grains. In addition, ϕ -scan analysis indicated that the films were completely oriented in the a - b plane; i.e., high-angle grain boundaries were absent.

We characterize the initial surface with the simultaneously acquired topographic and optical images from the NSOM. Figure C.1(a) shows a 5 micron square topographic scan on one of the samples used. Figure C.1(b) is the corresponding optical data taken with 514 nm light, displaying magnitude variations due to reflectivity changes. Since the films are uniform, the optical variations are likely due to changes in oxygen content. The optical image shows some correlation with the topographic grains. This is not a topographic induced artifact in the optical image, since the effect remains well away from the grain edges in this slow (due to high signal averaging) scanned data. It appears that the oxygen content varies from one grain to another. An overlay of the optical contours over the topographic gray scale illustrates this. Many of the topographic features appear outlined. This correlation is not, and isn't expected to be, one-to-one. Rather, the oxygen content varies primarily between grains when it does vary. Most grains sticking out of the surface have a significantly lower near-surface oxygen concentration than the rest of the sample (NSOM is surface-dominated). This suggests that oxygen can move within the ab -plane at room temperature much more readily than it can in the c -direction. It also suggests that oxygen can escape from the sample by diffusing laterally to the exposed edges of the ab -planes in these regions extending 6-70 nm above the surface plane. The uniformity within the grains and differences between some grains imply that the motion of oxygen through at least some grain boundaries is inhibited. Nothing can be said about the motion along grain boundaries from these measurements, although other data suggest mobility in that direction.

We next demonstrate EIM with the tunnel current. For the sample shown in Figure C.1, EIM was induced by applying $-1 V$ to the sample, and decreasing the tip-sample distance until a current of $2 nA$ was achieved. The system was left in this state for 36 minutes. The changes during EIM can be related to the grain structure by comparison of Figure C.1(c) and C.1(d). Since the topography remains unchanged, it is likely that oxygen motion is responsible for the changes. Oxygen was forced into the grain that sticks out of the surface. One might have expected a region of reduced oxygen content to encircle the grain, indicating the oxygen source. The fact that none is observed indicates either a diffuse source for the oxygen, or that the oxygen moves from the bulk of the film towards

the surface. The position of the arrows on the figure indicates the direction of contour line motion during the EIM process. Comparisons of the images in this manner yields good insights into the granular dependence of the EIM, but does not provide an ideal method for measuring the size of the effect. The variation in the native oxygen concentration of the samples with position also hinders this measurement. The size of the effect can be measured readily in 'after' minus 'before' optical difference images. We therefore performed cross-correlation between the before and after *topographic* images to quantify the lateral drift over the several hours between the two images, during which several other images and the EIM occurred. The shift given by this correlation agrees with that from the correlation of the two optical images to within one pixel. The measured drift rate was 260 nm per hour. Intensity variations between the optical images were corrected by scaling before subtraction. A similar shift and subtraction was performed with the topographic images before and after electron-induced-migration. The result showed only noise. We have not observed any evidence of topographic changes during the EIM of the oxygen. Figure C.2 shows these results for the same region as shown in Figure C.1, but as imaged with 488 nm light. The radius of the effected area is 250 nm. The results from a different sample, electromigrated for 8 hours at -3 V and 3nA, are shown in Figure C.3. It is interesting to note that the radius of the effected region is still approximately 250 nm despite the much stronger EIM driving force.

The size of the effect should depend upon the region for which the force is sufficient to move oxygen atoms. First, we note that there should be no effect due to local heating of the sample since the local temperature rise is extremely small. The energy input by the tunnel electrons is a few tens of nanowatts (similar to that of the light), and the heat diffuses into three dimensions, due to the small source size. Diffusion calculations [23] show that the temperature rises by many orders of magnitude less than it does with a larger spot. The force due to the current density falls as the current spreads out, eventually dropping as $1/\text{distance}$ for a thin film. A prediction of the size of the EIM-affected region, using current density requirements from the literature, yields a radius much smaller than we observe. Our configuration differs from prior work in that we inject few-volt electrons directly into the EIM region rather than locally increasing the current density of near-thermal-energy electrons through lithographic constriction of the conductor [1,2]. This means that we inject the electrons with a higher momentum, due to the increased local potential drop. It is likely that this voltage effect plays a major role in this process, as it has in other few-eV-electron-

induced processes [24,25,26]. In those previous studies of metallic films, the size was found to be limited by growth dynamics, and eventually the grain size, since the grain boundary strongly back- or inelastically-scattered the hot electrons. The figures support a similar conclusion here, although for motion of different components in a very different materials system. The size of the affected region after small doses should be dose-dependent, but at higher doses limits to a size given by either the grain size or the inelastic scattering length of the injected electrons. The grain size limitation, as suggested in Figure C.1, would imply that elastic or inelastic scattering confines the hot electrons to a single grain in this material also. The grain size limit would also tend to disfavor a pure electrostatic origin of the electron-induced-migration, as the electric field should persist across a grain boundary.

We have shown that electrons injected from a near-field metal clad probe can induce oxygen movement over significant distances in YBCO. Our images show changes in the reflectivity corresponding to a change in the oxygen concentration where the EIM occurred. The results suggest that hot electrons injected into YBCO remain confined to a single grain, at least until they lose sufficient energy such that they are unable to induce oxygen motion. No topographic changes are observed during the electron-induced-migration. The local variations in the oxygen concentration of the as-grown surfaces show that diffusion of oxygen at room temperature occurs primarily in the *ab*-plane and within a grain.

The authors thank Eric Ayars, Steve Winder and Sean Boylan for the help in stages of the instrument design. Funding for this work was provided by the Department of Education and the Department of the Navy, Office of Naval Research, through grant N00014-98-1-0228.

References

- [1] B. H. Moeckly, D. K. Lathrop, and R. A. Buhrman; Phys. Rev. B, **47** (1), 400-417 (1993).
- [2] B. H. Moeckly, R. A. Burhman, P. E. Sulewski, Appl. Phys. Lett. **64**, 1427 (1994).
- [3] H. D. Hallen, A. La Rosa, and C.L. Jahncke; Physica Status Solidi A **152**, 257-268 (1995).
- [4] C.L. Jahncke, M. A. Paesler, and H.D. Hallen; Appl. Phys. Lett. **67**, 2483-2485 (1995).
- [5] C.L. Jahncke and H. D. Hallen, 9th annual meeting of IEEE Lasers and Electro-Optics Society (LEOS) 96 conf. Proc. Vol. 1, pp. 176-177.
- [6] A.H. La Rosa, B. I. Yakobson, H.D. Hallen; Appl. Phys. Lett. **70** (13), 1656-1658 (1997).
- [7] P.E. Sulewski, T. W. Noh, J. T. McWhirter, A. J. Sievers, S. E. Russek, R. A. Buhrman, C. S. Jee, J. E. Crow, R. E. Salomon, and G. Myer, Phys. Rev. B **36** (4), 2357-2360 (1987).
- [8] G. Zhao, Y. Xu, W.Y. Ching, K. W. Wong; Phys. Rev. B, **36**, 7203 (1987).
- [9] K. Kamaras, C. D. Porter, M. G. Doss, S. L. Herr, D. B. Tanner, D. A. Bonn, J. E. Greedan, A. H. O'Reilly, C. V. Stager, and T. Timusk, Phys. Rev. Lett. **59** (8), 919-922 (1987).
- [10] J. Kircher, M. K. Kelly, S. Rashkeev, M. Alouani, D. Fuchs, and M. Cardona, Phys. Rev. B, **44**, 217-224 (1991).
- [11] H.A. Bethe, Phys. Rev. **66**, 163 (1944).
- [12] C.J. Bouwkamp, Phillips Research Report **5**, 401 (1950).
- [13] M.A. Paesler and P.J. Moyer, *Near-Field Optics: Theory, Instrumentation and Applications* (John Wiley and Sons, Inc., New York, 1996).

- [14] K. P. Rodbell, M.V. Rodriguez, and P. J. Ficalora; *J. Appl. Phys.* **61** (8), 2844-2848 (1986).
- [15] M.L. Dreyer, K.Y. Fu, and C.J. Varkar; *J. Appl. Phys.* **73** (10), 4894-4902 (1993).
- [16] K. Hinode, T. Furusawa, and Y. Homma; *J. Appl. Phys.* **74** (1), 201-206 (1993).
- [17] H. Boularot and R. M. Bradley; *J. Appl. Phys.* **80** (2), 756-761 (1996).
- [18] J. R. Lloyd; *Semicond. Sci. Technol.* **12**, 117-1185 (1997).
- [19] J. B. Goodenough and A. Manthiram; *Proceedings of the IX Winter meeting on Low Temperature Physics: High Temperature Superconductors* (World Scientific, Singapore, 1988) Vol. 295, pp. 18-27.
- [20] C.L. Jahncke and H.D. Hallen, *Rev. of Sci. Instr.* **68** (4), 1759 (1997).
- [21] Khaled Karrai and Robert D. Grober, *Appl. Phys. Lett.* **66**, 1842 (1995).
- [22] B. Moeckly and K. Char, *Physica C* **265**, 283 (1996).
- [23] A.H. LaRosa, C.L. Jahncke and H.D. Hallen; *SPIE Proc.* **2384**, 101 (1995).
- [24] H.D. Hallen, A. Fernandez, T. Huang, R.A. Buhrman, and J. Silcox, *Phys. Rev. Lett.* **69**, 2931 (1992).
- [25] H.D. Hallen and R.A. Buhrman in *Atomic and Nanometer-Scale Modification of Materials: Fundamentals and Applications*, edited by Ph. Avouris (Kluwer, Dordrecht, 1993).
- [26] H.D. Hallen, in *The Technology of Proximal Probe Lithography*, edited by Christie Marrian, Vol. IS10 (SPIE, Bellingham, 1993).

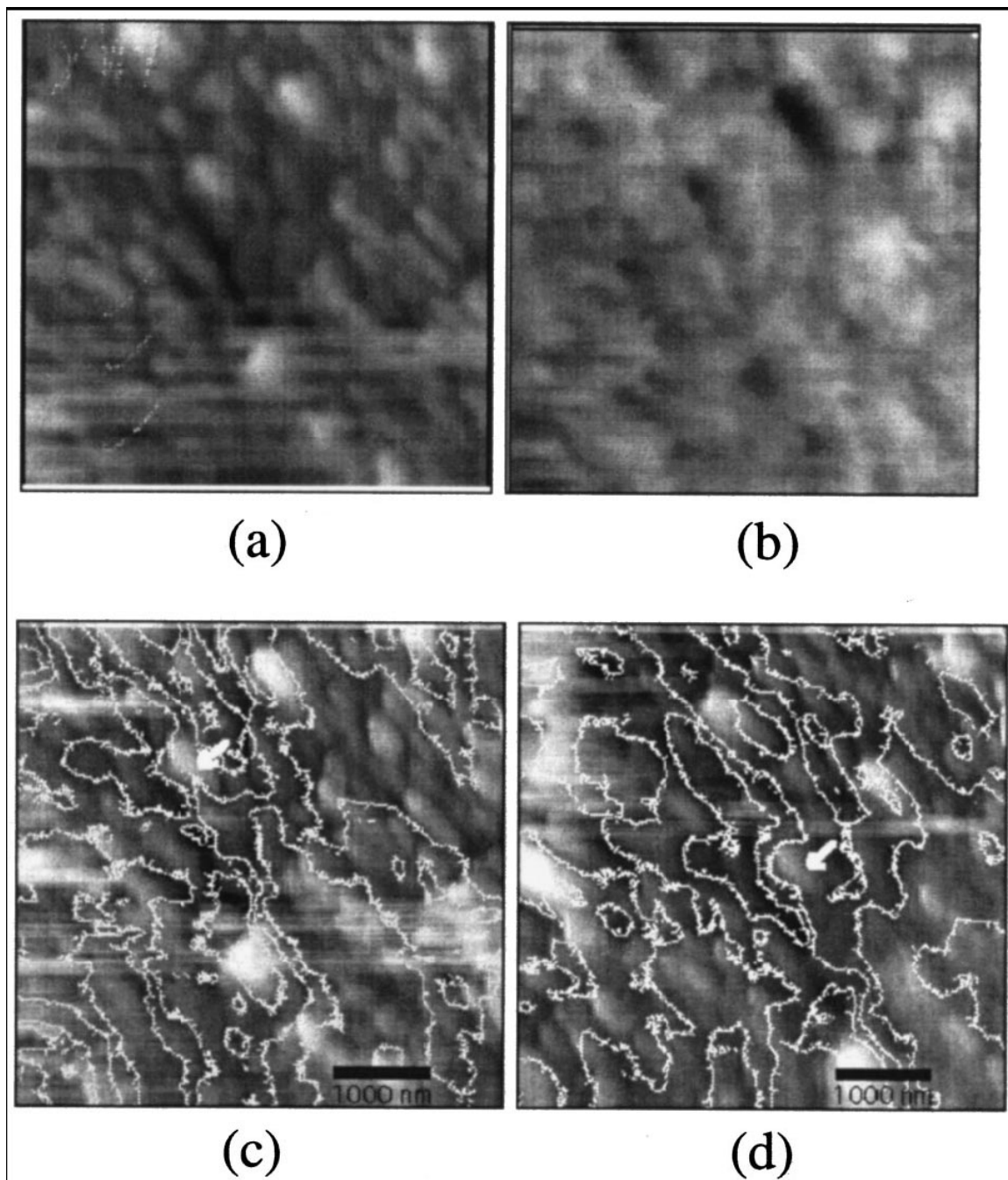


Figure C.1: Representative images of YBCO in a $5 \mu\text{m}$ square region. (a) The topography is shown with a 150 nm range of the gray scale (white higher). (b) The corresponding optical (green) image with a 6 nW range ($\sim 43 \text{ nW}$ average value, white lower reflectivity, higher oxygen content)). (c) An overlay of (a) in gray scale and (b) as a contour plot to illustrate the correlation between the grains and oxygen content before EIM. The tick marks on the contours point towards lower oxygen content. (d) As (c) but using the after EIM and optical images. The images are shifted due to microscope drift. The white arrow shows a major path of oxygen flow during the EIM as the contour has shifted across the grain indicated.

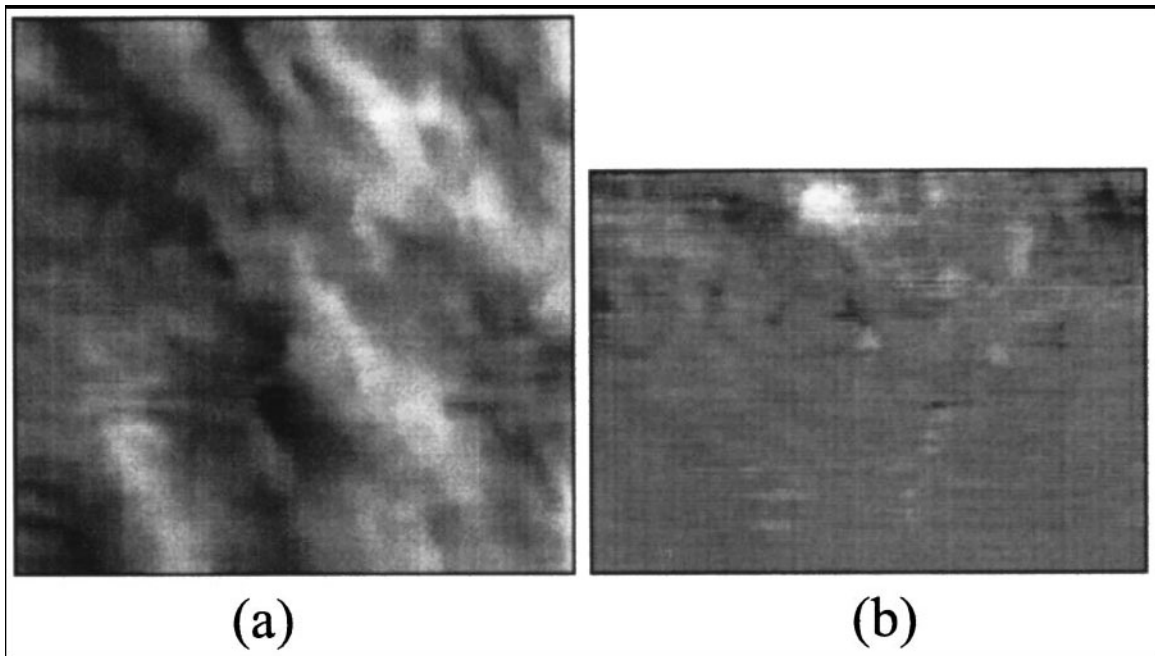


Figure C.2: (a) Optical image of the region shown in Figure C.1 but taken with blue (488 nm) light, 10 nW range, before EIM. (b) The difference image obtained after that shown in (a) was shifted and subtracted from the blue optical image taken after EIM with 12 nW range. Note that the region shown is smaller, $3.9 \times 2.9 \mu m$, since only the overlapping regions of the scans are meaningful.

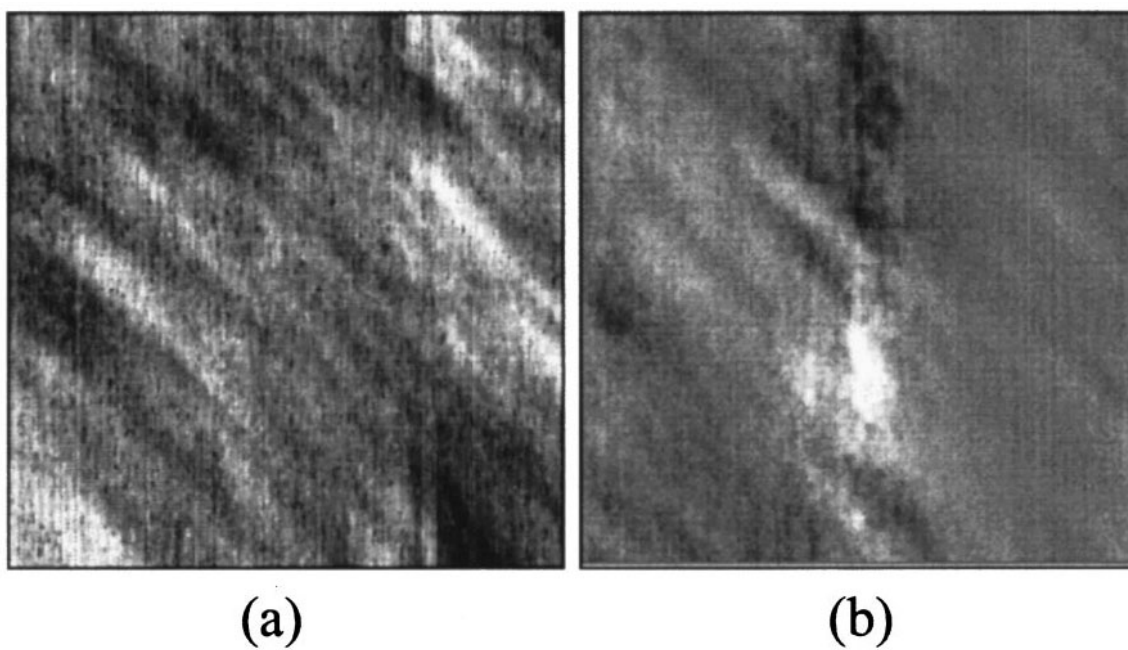


Figure C.3: (a) Optical image of a $10\ \mu\text{m}$ square region of a sample taken with green ($514\ \text{nm}$) light, before EIM, with $1\ \text{nW}$ range. (b) The difference image obtained after that shown in (a) was shifted and subtracted from the green optical image taken after EIM. The $9\ \mu\text{m}$ square overlapping region is shown.